Three-Dimensional Structure Determination of Surface Sites with Dynamic Nuclear Polarization Surface Enhanced NMR Spectroscopy

Pierrick Berruyer

To cite this version:

Pierrick Berruyer. Three-Dimensional Structure Determination of Surface Sites with Dynamic Nuclear Polarization Surface Enhanced NMR Spectroscopy. Analytical chemistry. Université de Lyon, 2017. English. NNT : 2017LYSEN042 . tel-01782401

HAL Id: tel-01782401
https://theses.hal.science/tel-01782401

Submitted on 2 May 2018

HAL is a multi-disciplinary open access archive for the deposit and dissemination of scientific research documents, whether they are published or not. The documents may come from teaching and research institutions in France or abroad, or from public or private research centers.

L'archive ouverte pluridisciplinaire **HAL**, est destinée au dépôt et à la diffusion de documents scientifiques de niveau recherche, publiés ou non, émanant des établissements d'enseignement et de recherche français ou étrangers, des laboratoires publics ou privés.

Numéro National de Thèse : 2017LYSEN042

THÈSE de DOCTORAT de L'UNIVERSITÉ DE LYON
opérée par
l'École Normale Supérieure de Lyon

École Doctorale 206
École Doctorale de Chimie de Lyon

Spécialité : Résonance Magnétique Nucléaire
Discipline : Chimie

Soutenance publique prévu le 8/09/2017, par :
Pierrick BERRUYER

Three-dimensional Structure Determination of Surface Sites with Dynamic Nuclear Polarization Surface Enhanced NMR Spectroscopy

Détermination structurale de sites de surface en spectroscopie RMN
exaltée par la polarisation dynamique nucléaire

Devant le jury composé de :

Jeffrey A. Reimer	Professeur Université de Californie, Berkeley	Rapporteur
Dominique Massiot	Directeur de Recherche Centre National de la Recherche Scientifique, Orléans	Rapporteur
Martin Blackledge	Directeur de Recherche Commissariat à l'Énergie Atomique, Grenoble	Examinateur
Chantal Andraud	Directrice de Recherche Centre National de la Recherche Scientifique, Lyon	Examinatrice
Leonard J. Mueller	Professeur Université de Californie, Riverside	Membre invité
Anne Lesage	Ingénieure de Recherche HDR Centre National de la Recherche Scientifique, Lyon	Co-encadrante de thèse
Lyndon Emsley	Professeur École Polytechnique Fédérale de Lausanne	Directeur de thèse

…

Remerciements

Avant de rentrer dans le cœur de cette thèse, je tiens ici à remercier l'ensemble des personnes qui rendu ce travail possible, directement ou indirectement.

Plus précisément, je remercie tout d'abord l'ensemble des membres de mon jury de soutenance : le Pr Reimer et le Dr Massiot qui ont accepté d'évaluer mon manuscrit en plein été ; le Dr Blackledge, la Dr Andraud, le Pr Mueller qui ont accepté de participer à mon jury de soutenance.

Je remercie ma co-encadrante de thèse, la Dr Anne Lesage et mon directeur de thèse, le Pr Lyndon Emsley. Je les remercie pour leur confiance, pour la liberté qu'ils m'ont laissé dans mes travaux, pour le niveau d'équipement exceptionnel du CRMN à lequel ils m'ont permis d'avoir accès, et pour m'avoir proposé et guidé dans les projets intéressants qui sont présentés dans ce manuscript. Je vous remercie en particulier pour m'avoir appris pendant ces trois années, l'importance de la collaboration scientifique qui rend le travail humainement très intéressant et scientifique plus solide. Plus précisément je retiendrais qu'en Science, personne ne peut, ni ne sait tout faire mais qu'il est primordial de pouvoir identifier ce que l'on peux faire. Anne, je te remercie pour m'avoir accompagner quasi-quotidiennement au cours de cette thèse, pour la qualité de ton encadrement, et pour ta patience infinie à m'expliquer et me réexpliquer des expériences de RMN.

Les travaux de cette thèse sont toujours faits dans le cadre de collaboration passionnante. Je remercie donc chaleureusement le Pr Christophe Copéret et son groupe à l'ETH Zurich, en particulier Dr. Matthew Conley et Dr. Daniel Silverio, qui ont synthétisé un grand nombre de matériaux étudiés dans au cours de cette thèse. Je remercie également le Dr Chloé Thieuleux à CPE Lyon et le Dr. Marc Renom Carrasco avec qui j'ai eu l'occasion de travailler. Je remercie le Dr. Olivier Ouari et le Pr. Paul Tordo à l'Université de Aix-Marseille qui nous fournissent les agents polarisants indispensables à la réalisation des expériences de DNP. Merci au Dr Jasmine Viger-Gravel de l'EFPL avec qui je travaillais sur DNP Jelly. Bien que nos sessions étaient parfois frustrantes car l'on butait (trop !) souvent sur la reproducibilité de nombreux résultats, les semaines à Lausanne était toujours agréable et je suis maintenant fluent sur le franglais de Gattineau ! Merci aussi au Dr Sachin Chaudhari qui m'a beaucoup appris sur la société indienne lors de nos interminables attentes que la température de la sonde 1.3 mm se stabilise. Je remercie tout particulièrement le Dr. David Gajan qui m'a appris beaucoup sur la chimie des matériaux que j'ai étudié dans ma thèse, mais aussi sur l'instrumentation RMN, DNP et du laboratoire. Je remercie Ribal Jabbour, étudiant de M2, qui continue l'étude du catalyseur d'iridium abordé en fin de thèse.

Je remercie toute les personnes du laboratoire que j'ai pu côtoyer au cours de ces dernières années au CRMN et qui participent à la vie du laboratoire. Merci donc à Audrey, Bénédicte, Gilles, Torsten, Cécile G., Cécile C., Andrea, Kévin, Tobias, Marta, Jan, Kristaps, Elodie, Dorothéa, Daniella, Guido, Diane, Olivier, Ladislav, Sylvie, Houda, Manhal, ... Un petit clin d'œil particulier à notre groupe d'exclu de la cantine CNRS tous les midis ;-) Bien sur un grand merci tout particulier à Tanguy sans qui ces trois années n'auraient pas été les mêmes !

Je remercie tous mes amis que j'ai rencontré au cours de ces sept années passées à l'ENS Lyon, après les années ENS, l'agrégation puis la thèse, c'est l'heure du départ ! Merci à Maëlle, Eloïse, Romain, Mathilde, Arthur, Benjamin, Laure-Lise, Nils, Antoine, Apo.

Finalement je remercie toute ma famille : mon papa et ma maman, mes frères, Joris et Florent, ma sœur, Nelly, mes neveux, Enzo et Théo et mes nièces, Chloé et Calie mais aussi mes grands-parents, mes cousins...

Bonne lecture.

Abstract

The ability to understand the properties of chemical systems relies on their detailed description at the molecular level. Over the last century, several methods based on X-ray diffraction have allowed a structure-based understanding of many materials. However, several key questions often remain unanswered. In particular when the system under investigation is located on a surface. Although an extensive range of surface-sensitive methods are available for surface science and give valuable information, they only lead to a partial understanding of surfaces at the molecular level. Moreover, these methods are not compatible with all kinds of materials and usually require the use of a model and pristine surface.

Solid-State NMR would be a method of choice to characterize surfaces. However, the approach suffers from its intrinsically low sensitivity and this is strongly emphasize in the case of surfaces where the atoms of interest are diluted in the matrix. Dynamic Nuclear Polarization (DNP) applied to surfaces (SENS) recently emerged as a very promising method to characterize surface sites. It offers a dramatic enhancement of NMR sensitivity and DNP applied to materials has led to many examples in the last ten years.

In the present thesis, I have shown that DNP SENS, in combination with EXAFS, allowed the detailed 3D structure determination of the silica-supported organometallic complex determined with a precision of 0.7 Å.

In parallel, some experimental aspect of DNP SENS have been explored. A spin diffusion has been developed to understand diffusion of hyperpolarization in porous media. A new aqueous DNP matrix, coined DNP Jelly, has been developed to characterize nanoparticles and thus expanding experimental range of DNP SENS. Finally, the first experiment of DNP NMR at fast magic angle spinning (up to 40 kHz) and high field are reported.

Résumé de la thèse

La capacité à déterminer les structures moléculaires en trois dimensions à partir de monocristaux par des méthodes de diffraction a transformé la chimie des matériaux. Le problème de la détermination de structure est en grande partie non résolu, en particulier si le système étudié est situé à une surface et n'a pas de périodicité, comme dans la plupart des matériaux fonctionnels actuels.

La Résonance Magnétique Nucléaire (RMN) à l'état solide serait une méthode de choix pour caractériser les surfaces mais la limite de détection de la RMN est beaucoup trop faible pour permettre à la RMN de caractériser les surfaces. L'introduction récente d'une nouvelle approche utilisant la Polarisation Dynamique Nucléaire (DNP) pour améliorer la sensibilité de la RMN des surfaces (DNP SENS) permet à présent de réaliser des expériences qui étaient totalement impossible il y a quelques années encore.

Plus particulièrement, grâce à la méthode DNP SENS, les présents travaux de thèse aboutissent à la première structure tridimensionnelle d'un complexe organométallique supporté sur silice, avec une précision de 0,7 Å.

De nombreux aspects de l'expérience DNP SENS ont été exploré. Le transport de de l'hyperpolarisation par diffusion de spin est primordial et un modèle numérique dans les matériaux mésoporeux a été développé. De plus, une nouvelle matrice aqueuse se basant sur des gels polyacrylamides a été mise au point et utilisée pour la caractérisation par RMN de nanoparticules permettant ainsi d'étendre les domaines d'application de DNP SENS. Enfin les premières expériences RMN DNP combinant hauts champs magnétiques et haute fréquence de rotation d'échantillon sont présentées.

Contents

1 Introduction 1

2 Surface structure investigations in solid-state NMR 9

2.1 Introduction . . . 10

2.2 Well Defined Immobilized Heterogenous Catalysts . . . 10

2.2.1 Generalities . . . 10

2.2.2 Silica-based materials . . . 12

2.3 Solid-State NMR Spectroscopy for single well-defined supported sites heterogeneous catalysts . . . 15

2.4 Hyperpolarizing surfaces in NMR using Dynamic Nuclear Polarization . . 21

2.4.1 Introduction . . . 21

2.4.2 Basics of Magic Angle Spinning Dynamic Nuclear Polarization in NMR . . . 23

2.4.3 MAS DNP applied to Surfaces . . . 39

2.5 Conclusions . . . 48

I Expanding the experimental range of Dynamic Nuclear Polarization for surfaces 51

3 Experimental aspects of impregnation in DNP SENS of porous silica materials 53

3.1 Introduction 54
3.2 Diffusion of the polarizing agent into mesoporous materials 56
3.2.1 Signal quenching induced on surface nuclei when introducing nitroxides into porous silica 56
3.2.2 Spin diffusion simulations 58
3.3 Partial Impregnation Dynamic Nuclear Polarization 66
3.3.1 Effect of partial pore filling on DNP SENS experiments 67
3.3.2 Pore filling mechanisms 69
3.4 Conclusions 72

4 40 kHz Magic Angle Spinning Dynamic Nuclear Polarization 75

5 Frozen acrylamide gels as DNP matrix 77

II Three-dimensional surface structure determination 79

6 Direct observation of three-dimensional surface molecular structure 81

7 Perspectives: exploring low coordinated Ir-NHC surface sites 83

8 Conclusions 87

Chapter 1

Introduction

En chimie, la capacité à comprendre les propriétés des systèmes chimiques reposent sur leurs descriptions détaillées au niveau moléculaire. Au cours du dernier siècle, plusieurs méthodes comme la spectroscopie infrarouge (IR), la diffraction des rayons X (XRD)... ont été développées, permettant une compréhension de la structure de nombreux matériaux. Cependant, lorsque l'on a l'intention de décrire les espèces de surface au niveau atomique, le problème devient plus délicat et plusieurs questions clés restent souvent sans réponse. Les processus chimiques qui se produisent à une surface jouent un rôle crucial dans la chimie moderne. De nombreuses questions se posent lors de l'exploration de surfaces de matériaux modernes, liées à la description des processus d'adsorption-désorption, de la fonctionnalisation (structurale et dynamique des fonctionnalités de surface), des réactions à la surface ou de la diffusion de produits chimiques. En catalyse hétérogène, le catalyseur - souvent en phase solide - est impliqué par sa surface dans le processus chimique.

Actuellement, bien qu'un vaste choix de méthodes sensibles à la surface soient disponibles, elles ne conduisent qu'à une compréhension partielle des surfaces au niveau moléculaire. En outre, ces méthodes ne sont pas compatibles avec toutes sortes de matériaux et exigent généralement l'utilisation d'un modèle et d'une surface vierge. Parmi les développements les plus récents pour fournir une description atomique des surfaces, en 2015, de Oteyza *et al.* ont utilisé la microscopie de force atomiqe sans contact (nc-AFM) pour observer l'image d'une liaison covalente d'adsorbats sur une surface de Ag(100). [1]

L'ajout de résonance magnétique nucléaire à l'état solide (SSNMR) à la boîte à outils du chimiste pour étudier les surfaces améliorerait le développement futur des sciences de la surface car la SSNMR est, en principe, une méthode de choix pour évaluer ces questions. [2] En effet, la SSNMR a montré sa capacité à caractériser de nombreux systèmes solides allant des fibriles protéiques aux polymères en passant par des produits pharmaceutiques et est couramment utilisé pour l'étude de matériaux. En outre, la SSNMR peut être utilisé pour révéler des informations dynamiques, ce qui rend l'approche non seulement adaptée à l'étude de la structure, mais aussi pour l'étude de processus chimiques complexes. Alors que la SSNMR serait une méthode de choix pour la caractérisation des surfaces, l'approche souffre d'une sensibilité intrinsèquement faible. De plus, l'étude des espèces de surface où les atomes d'intérêt sont dilués dans la matrice accentue fortement cette question de sensibilité. En conséquence, la SSNMR est souvent inefficace pour caractériser les surfaces de nombreux matériaux modernes. La polarisation dynamique nucléaire (DNP) appliquée aux surfaces a récemment émergé comme une méthode très prometteuse pour caractériser les sites de surface. Il offre une amélioration spectaculaire de la sensibilité au RMN en transférant la polarisation des électrons non appariés dans des conditions cryogéniques. La DNP a suscité une attention considérable pendant les deux dernières décennies. L'application de DNP aux matériaux a conduit à de nombreux exemples au cours des dix dernières années.

Dans la présente thèse, l'objectif est de caractériser les surfaces par SSNMR exaltée par DNP. En particulier, mon objectif est de démontrer que la structure tridimensionnelle des sites de surface peut être entièrement résolue.

Dans le premier chapitre de la présente thèse, j'ai examiné l'état de l'art quant à la caractérisation de sites individuels bien définis sur des surfaces à l'aide de la SSNMR. Tout d'abord, certains aspects importants de la chimie organométallique de surface sont énoncés, car il s'agit d'une voie importante en chimie pour obtenir des sites de surface bien définis. J'ai ensuite décrit les méthodes utilisées dans la SSNMR conventionnel pour la caractérisation de ces matériaux. Enfin, comme le problème de sensibilité est fortement exacerbé dans l'étude de la surface, j'analyse l'approche d'hyperpolarisation par la polarisation dynamique nucléaire. Les concepts fondamentaux, les développements récents et les dernières applications sont examinés. En particulier l'expérience dite DNP SENS est présenté, il s'agit d'une méthode très robuste pour la caractérisation des surfaces en RMN.

Après cette introduction, les résultats obtenus au cours des trois années de mes études doctorales sont présentés en deux parties séparées. La première partie est axée sur les aspects pratiques et instrumentaux de l'approche DNP SENS. L'objectif est de mieux comprendre le processus DNP lorsqu'il est exploité pour les surfaces et pour améliorer les conditions expérimentales et la formulation de l'échantillon, dans laquelle cette approche peut être appliquée. Cette première partie comprend trois chapitres.

Tout d'abord, deux aspects fondamentaux de l'imprégnation de DNP SENS ont été étudiés: (*i*) la diffusion de l'agent polarisant dans le milieu poreux et (*ii*) le rapport entre le volume de solution utilisé pour l'imprégnation et la masse d'agent polarisant. Cela a permis une meilleure compréhension de l'approche DNP SENS, en particulier, il semblerait que le processus de diffusion de spin joue un rôle clé dans DNP SENS. Un modèle de diffusion de spin de l'hyperpolarisation DNP adapté à une matrice poreuse est présenté.

Dans le deuxième chapitre, les premières expériences combinant la rotation à l'angle magique jusqu'à 40 kHz et les hauts champs magnétiques (800 MHz) en conditions DNP sont réalisées. L'effet de la rotation à l'angle magique sur le gain DNP est étudié. On observe que le gain DNP est maintenue jusqu'à 40 kHz. Cependant, une importante perte de signal a été observée à une fréquence de rotation élevée.

Enfin, dans le troisième chapitre, une nouvelle matrice DNP aqueuse, *DNP Jelly*, est proposée. Cette formulation est basée sur un gel de polyacrylamide. L'utilisation de *DNP Jelly* se révèle appropriée pour la caractérisation des nanoparticules CdTe présenté dans ce même chapitre.

Dans la deuxième partie, je montre que la détermination de la structure tridimensionnelle d'un complexe organométallique sur une surface de silice amorphe utilisant des mesures RMN à l'état solide est possible. La détermination de la structure est rendu accesible grâce à une approche combinant la spectroscopie RMN exaltée par polarisation nucléaire dynamique avec l'EXAFS. Le résultat est une structure détaillée du complexe de surface déterminée avec une précision de 0.7 Å.

In chemistry, the ability to understand the properties of chemical systems relies on their detailed description at the molecular level. Over the last century, several methods like infrared (IR) spectroscopy, mass balance analysis, X-ray diffraction (XRD)... were developed, allowing a structure-based understanding of many materials. However, when one intends to describe the surface species at the atomic level the problem becomes trickier, and several key questions often remain unanswered. Chemical processes that occur at a surface play a crucial role in modern chemistry. Many questions arise when exploring surfaces of modern materials, related to the description of adsorption-desorption processes, functionalization (structure and dynamics of surface functionalities), reactions at the surface, or diffusion of chemicals. In heterogeneous catalysis, the catalyst - often in the solid phase - is involved through its surface in the chemical process.

Currently, although an extensive range of surface-sensitive methods are available for surface science and give valuable information, they only lead to a partial understanding of surfaces at the molecular level. Moreover, these methods are not compatible with all kinds of materials and usually require the use of a model and pristine surface. Among the most recent development to provide an atomic-level description of surfaces, in 2015, de Oteyza *et al.* have used state-of-the-art non-contact Atomic Force Microscopy (nc-AFM) method to directly image covalent bond of adsorbates onto a Ag(100) surface, thus providing insights in the description of Bergman reaction of formation of cycle.[1]

Adding solid-state nuclear magnetic resonance (SSNMR) to the chemist's toolbox for studying surfaces would improve future development in surface science as SSNMR is, in principle, a method of choice to assess such questions.[2] Indeed, SSNMR has shown its capability to characterize many solid systems ranging from protein fibrils to polymers or pharmaceuticals and is commonly used for the study of materials. Moreover, SSNMR can be used to reveal critical dynamical information, making the approach not only suitable for the structure but also relevant for the study of complex chemical processes. While SSNMR would be a method of choice for the characterization of surfaces, the approach suffers from its intrinsically low sensitivity. Moreover, the study of surface species where the atoms of interest are diluted in the matrix strongly emphasize this sensitivity issue. As a consequence SSNMR is often inefficient to characterize surfaces of many modern materials. Dynamic Nuclear Polarization (DNP) applied to surfaces recently emerged as a very promising method to characterize surface sites. It offers a dramatic enhancement of NMR sensitivity by transferring polarization from unpaired electrons under cryogenic conditions. DNP has raised considerable attention for the last two decades. Application of DNP to materials has led to many examples in the last ten years.

In the present thesis, my interest is in characterizing surfaces from SSNMR enhanced with the DNP method. In particular, my aim is to demonstrate that the three-dimensional structure of surface sites can be fully resolved.

In the first chapter of the present thesis, I have reviewed the characterization of single well-defined sites supported on surfaces using SSNMR. First, some important aspects of surface organometallic chemistry are reported, since this is an important route in chemistry to obtain single well-defined surface sites. I have then described the methods used in conventional SSNMR for the characterization of such materials. Finally, as the sensitivity issue is strongly exacerbated in the study of surface, the hyperpolarization approach by Dynamic Nuclear Polarization is analyzed. Basics concepts, recent developments, and the latest applications are reviewed, in particular the approach, coined DNP Surface Enhanced NMR Spectroscopy (DNP SENS), is presented, which is a very robust method for the characterization of surfaces.

After this introduction, the results obtained during the three years of my doctoral studies are presented in two separated parts. The first part is focused on practical and instrumental aspects of the DNP SENS approach, to better understand the DNP process itself when exploited for surfaces and to improve the experimental conditions/the formulation, in which this approach can be applied. This first part includes three chapters.

First, two fundamental aspects of impregnation in DNP SENS have been investigated: (*i*) the diffusion of the polarizing agent in the porous medium and (*ii*) the ratio between the volume of solution used for impregnation and the weight of the material. This has allowed for a better understanding of the DNP SENS approach, in particular, it appeared that spin diffusion process plays a key role in DNP SENS resulting in the development of a spin diffusion model of DNP hyperpolarization adapted to porous matrix.

In a second chapter, the first experiments combining fast magic angle spinning (up to 40 kHz) and DNP at high field (800 MHz) are reported. The effect of fast spinning on the DNP enhancement is investigated. DNP enhancement is maintained up to 40 kHz magic angle spinning (MAS) rate. However, an important loss of signal due an increase quenching has been observed at a high spinning rate.

Finally, in the third chapter, a new aqueous DNP matrix, coined DNP Jelly, is proposed. It is based on a polyacrylamide gel. The use of DNP Jelly is demonstrated to be suitable for the characterization of CdTe nanoparticles.

In the second part, I have shown that the determination of the three-dimensional structure of an organometallic complex on an amorphous silica surface using solid-state NMR measurements is possible. Structure determination is enabled through a dynamic nuclear polarization surface enhanced NMR spectroscopy approach. The result, in combination with EXAFS, is a detailed structure of the surface complex determined with a precision of 0.7 Å. A single well-defined conformation that is folded toward the surface in such a way as to include an interaction between the metal center and the surface atoms was observed.

Chapter 2

Surface structure investigations in solid-state NMR

2.1 Introduction

In the present chapter, I review the recent SSNMR development for the study of surfaces. This chapter focuses on the ability of SSNMR to reveal an atomic level description of active sites on chemically functionalized surfaces with catalytic relevance.

The first part of this chapter is dedicated to Surface Organometallic Chemistry (SOMC) and Supported Homogeneous Catalysis (SHC). The idea of this first section is not to give an exhaustive description of the field but rather an overview of this important part of modern chemistry which has raised a critical attention in the chemists' community. In the second part, I report examples of the atomic description of surfaces using conventional SSNMR experiments. Note that Marchetti *et al.* very recently published an excellent review of studies conducted with SSNMR on surfaces and interfaces.[3] As one of the pitfalls of characterizing surfaces from SSNMR is its intrinsically low sensitivity, in the third part, I concentrate on the description of state-of-the-art developments in hyperpolarization from Dynamic Nuclear Polarization (DNP) for SSNMR under Magic Angle Spinning (MAS). The review is stressed on the description of surfaces where DNP hyperpolarization is used to reveal surface structural and dynamical characteristics.

2.2 Well Defined Immobilized Heterogenous Catalysts

2.2.1 Generalities

In an industrial context, the use of heterogeneous catalysis is very relevant, as this class of catalysts usually simplifies purification steps. For instance, in 2015, Tsubogo *et al.* published [4] the synthesis of (R)-Rolipram, an anti-inflammatory pharmaceutical, using a continuous flow system with multiple chemical reaction steps. The synthesis was achieved without the separation of any excess reactants, by-products, or catalysts. This was enabled by the use of a series of continuous flow reactors packed with different heterogeneous catalysts to ensure both chemo- and enantio-selectivities of the reaction, and a decent overall yield. This kind of process is economically relevant for the pharmaceutical industry, as it simplifies purifications steps, but also ecologically relevant as it should reduce the use of big amounts of organic solvents in purification steps. Here, the use of efficient and optimized heterogeneous catalysts is crucial in the success of such an approach as (*i*) they simplify the catalyst elimination step; (*ii*) avoid complex purification of the final products.

Thus there is an important interest in obtaining and optimizing heterogeneous catalysts. However, active sites characterization of heterogeneous catalysts is still challenging and never easy. SOMC and SHC are popular strategies to obtain supported single site catalysts on a surface where active sites are covalently immobilized onto a surface. These methods aim to “bridge the gap”[5] between surface science and molecular organometallic chemistry. Indeed, organometallic chemistry provides powerful tools to allow rational design of homogeneous organometallic catalysts from molecular description.[6] Having well-defined organometallic sites on a surface permits taking advantage of both tools of molecular organometallic chemistry and robustness of heterogeneous catalysts. In SOMC, well-defined surface catalytic sites are obtained by the reaction between an organometallic fragment and a surface. In SHC, a homogenous catalytic center is anchored to a surface via a pre-existing linker.[7]

For the last decades, various surface types have been used as supports for well-defined surface sites such as silica,[8] alumina, [9] aluminosilicates,[10] etc. Silica is among the most popular support for single well-defined surface sites in heterogeneous catalysis.[5] Due to both the flexibility of the Si-O-Si angle and rigidity of O-Si-O angle, silica exists in a large number of different phases as represented in FIGURE 2.1. It can be non-porous, with at least fourteen known polymorphs,[11, 12], or also gives dense non-periodic glass phase. It can also form porous materials, that can be periodic or non-periodic. However, in the context of catalysis, amorphous silica is usually the most widely used support in its porous or non porous forms.[12] There is a considerable number of examples of well-defined catalytic centers supported on silica for various types of catalyzed reactions, such as metathesis, hydrogenation, Ziegler-Natta polymerization, hydrogenolysis, isomerization, epoxidation, to cite few examples; extensively reviewed in 2016 in [8].

While at the premises of SOMC, surfaces was intuited to act as *classical ligand*, it is now well established that surfaces adds some particularities. In particular, the surface is a rigid ligand and significantly reduces the mobility of organometallic species. For example, silica surface allows for the stabilization of electron-deficient Ta(III) or Zr(IV) complexes, at oxidation number that has not be observed before in homogeneous organometallic chemistry.[13, 14, 15]

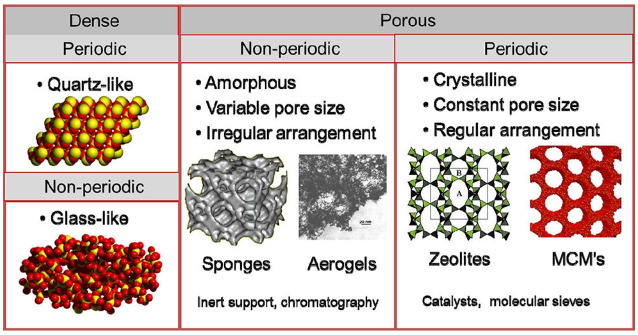
Dense
Porous
Periodic
Non-periodic
Periodic
• Quartz-like
• Amorphous
• Variable pore size
• Irregular arrangement
• Crystalline
• Constant pore size
• Regular arrangement
Non-periodic
• Glass-like
Sponges
Aerogels
Zeolites
MCM's
Inert support, chromatography
Catalysts, molecular sieves

FIGURE 2.1: Different solid phases involving $\{SiO_4\}$ units. Reprinted with permission from [12]. Copyright 2013 American Chemical Society.

2.2.2 Silica-based materials

As silica-based materials will be the focus of an important part of this thesis, some general features of this class of materials are therefore reported hereinafter. SOMC mainly uses amorphous silica in the form of non-porous particles or porous materials. The most common way to synthesize silica is to start from a silica precursors such as tetraethylorthosilicate (TEOS) or tetramethylorthosilicate (TMOS), which condensate to afford silica materials via the so-called sol-gel approach. In the 90s, very efficient methods have been described to obtain mesoporous silicas, which exhibit a dense network of pores and therefore a large surface area. MCM-41,[16, 17] SBA-15,[18] and SBA-16 are,[19] for instance, popular mesoporous silica matrices. Mesoporous silica is obtained using the sol-gel approach in the presence of a structure directing agent (SDA). The SDA first self-assembles in solution to form a liquid-crystal phase that works as a template for the formation of the porous network during the condensation of silica. FIGURE 2.2, reproduced from [20], schematically lays out this synthetic process. After the condensation of silica, SDAs can be removed via calcination or extraction, yielding empty and accessible pores.[20]

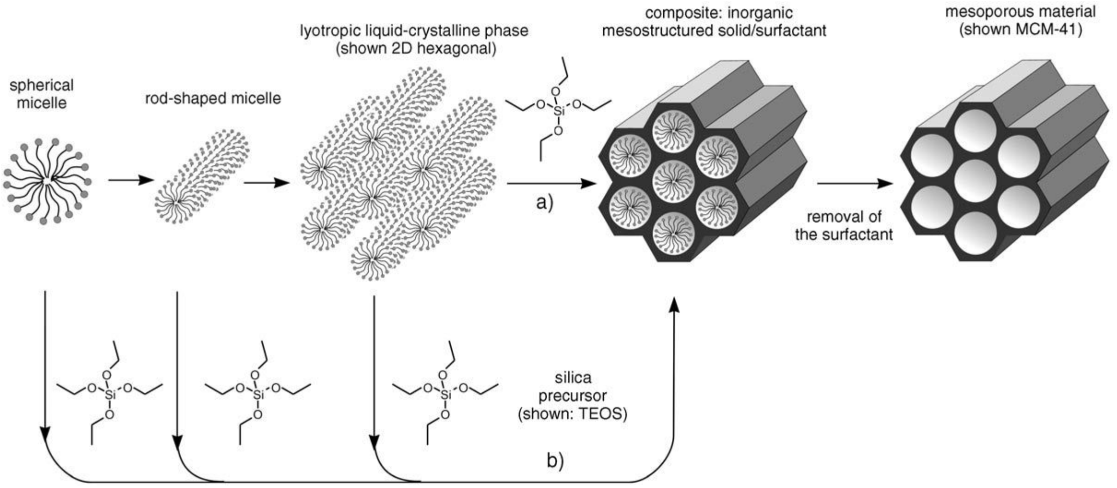
spherical micelle
rod-shaped micelle
lyotropic liquid-crystalline phase (shown 2D hexagonal)
composite: inorganic mesostructured solid/surfactant
mesoporous material (shown MCM-41)
a)
removal of the surfactant
silica precursor (shown: TEOS)
b)

FIGURE 2.2: Sol-gel approach for the synthesis of MCM-41 silica. Two routes are possible: a) true liquid-crystal template mechanism, and b) cooperative liquid-crystal template mechanism. Reprinted with permission from [20]. Copyright 2006 John Wiley and Sons.

Control of silanol density

Under typical laboratory condition, silica surfaces exhibit two major functional groups: silanols (Si-OH), and siloxane bridges (Si-O-Si). Both can also be present in the bulk, but they are not accessible. On silica surface, silanols are found isolated or as geminal or vicinal silanols (see FIGURE 2.3). Si atoms bound to one OH are denoted as Q_3 (isolated and vicinal), Si atoms bound to two OH groups are named Q_2 (germinal). Q_4 denotes a silicon without OH group and involved in four Si-O-Si bridges.[12] As such structure-templated sol-gel processes are performed under aqueous conditions, the existence of surface silanols cannot be avoided, however, their density can be controlled using de-hydroxylation by heating the silica under reduced pressure.[21]

Strategies to functionalize silica surfaces

The first common strategy to functionalize silica surfaces is the post-synthetic functionalization route. The presence of silanols allows introducing a catalytic center, by a post-modification of the silica surface. This can be achieved for example by a reaction between surface silanols and organometallic precursors to afford the formation of a surface organometallic fragment.[22, 23] FIGURE 2.4 lays out an example of a rhenium catalyst supported on silica $SiO_{2-(700)}$ (silica partially at dehydroxylated at 700°C) obtained through the reaction between surface silanols and an organometallic complex. An alternative post-modification approach is to graft functionalities on the silica surface via a reaction with organosilanes $(R^1O)_3SiR^2$, chlorosilanes $ClSiR_3$, or silazanes $HN(SiR_3)_3$.[20]

A second common strategy to incorporate functionalities to the silica surface is the use of co-condensation. In this approach, the silica is synthesized via condensation of tetraalkoxysilanes (e.g. TEOS or TMOS) and trialkoxyorganosilanes (e.g. $(EtO)_3SiR$), thus the organic moiety R is directly incorporated on the surface. This strategy has the advantage of allowing a more homogenous distribution of the functionalities on the surface.[24]

Tuning hydrophobicity of silica surfaces

Surface silanols give silica a hydrophilic character because it enables the possibility of formation of hydrogen bonds between the surface and water molecules. Thus, it is possible to make the surface hydrophobic by capping silanols with hydrophobic organic moieties. That is usually achieved by reaction of surface silanols with chlorosilane, *e.g.* tetramethylsilyl chloride. Surface passivation also allows avoiding side-reactions with the surface silanols during the formation of the active center on the surface. For instance, Conley *et al.* explain that the passivation of surface silanols was required to use the reagents necessary to obtain an Ir metal carbene supported on the surface without side-reaction with surface silanols.[24]

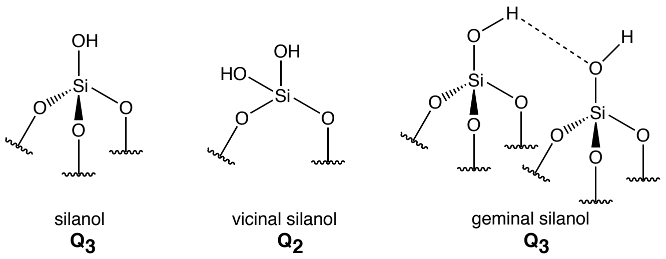

FIGURE 2.3: Isolated, vicinal, and geminal surface silanols

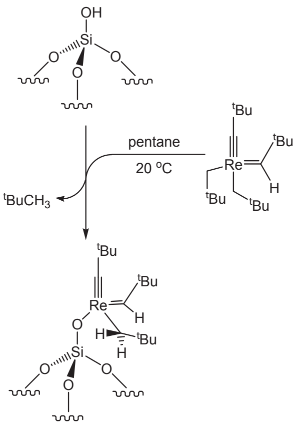

FIGURE 2.4: Synthetic route to Rhenium complexes supported on silica. Reprinted with permission from [25]. Copyright 2009 John Wiley and Sons.

This approach has led to the synthesis of a large number of new heterogeneous catalysts where the catalytic properties have been efficiently tuned from their homogeneous analogues. Supported nanoparticles also provide an efficient route to obtain well-defined sites in heterogeneous catalysis and also take advantage from a rational design based on homogenous catalysts. However, supported nanoparticles cannot be considered as part of SOMC as this class of material do not systematically include an organic moiety to tether the NPs to a surface. In 2010, Fu *et al.* demonstrated the possibility to obtain a heterogeneous catalyst based on coordinately unsaturated ferrous (CUF) sites from Pt-Fe nanoparticles supported on silica particles. CUFs are attractive sites as they can stabilize the unusual Fe(IV) oxidation state. They demonstrated their catalyst to be efficient for carbon monoxide oxidation. Apart from that, CUF sites are particularly well-known catalytic sites in enzymes, and immobilizing such active sites provides attractive catalysts for oxidation processes in industry.[26]

2.3 Solid-State NMR Spectroscopy for single well-defined supported sites heterogeneous catalysts

Over the years, SSNMR has proven to be very efficient to characterize active catalytic species located on a surface, providing valuable information for understanding the catalytic activity. In this section, I review examples where SSNMR has been successfully used to characterize functionalized surfaces, focusing on catalysts immobilized on surfaces.

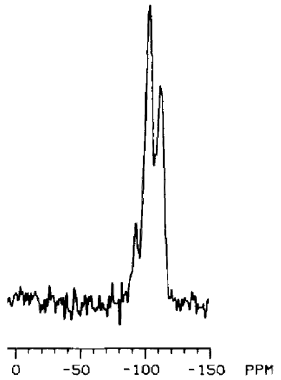

FIGURE 2.5: ^{29}Si CPMAS spectrum of silica gel obtained at 11.88 MHz (1014 scans). Reprinted with permission from [27]. Copyright 1980 American Chemical Society.

Structural type	δ_{Si} (ppm)
$(HO)_2\mathbf{Si}(OSi)_2$	- 90.6
$(HO)\mathbf{Si}(OSi)_3$	- 99.8
$\mathbf{Si}(OSi)_4$	- 109.3

TABLE 2.1: Chemical shift assignement. The reference for chemical shift is tetramethylsilane. Data from [27]

Cross-polarization (CP), was introduced by Hartmann and Hahn[28] in 1962 and was significantly improved by Lurie and Slichter two years later[29] and then first successfully demonstrated for natural abundance ^{13}C NMR in 1972.[30, 31] The approach relies on the magnetization transfer from sensitive high gyromagnetic ratio nuclei to less sensitive low gyromagnetic nuclei. The method uses the dipolar coupling to perform the transfer. As the dipolar coupling scales by r^{-3}, where r is the distance between the two nuclei, it provides a very efficient way to selectively polarize surfaces in organic-inorganic materials (such as functionalized silica) where the bulk does not contain any protons. In 1980, Maciel and coworkers used CPMAS (Cross Polarization Magic Angle Spinning) experiments to study silica gel surfaces. They were able to polarize surface ^{29}Si nuclei from protons of silanol surface groups.[27] Their ^{29}Si CPMAS spectrum of silica gel is depicted in FIGURE 2.5 and the chemical shifts assignments in TABLE 2.1. In 1981, Maciel *et al.* reported surface studies of functionalized silica gel where CPMAS experiments were used to obtain surface selective ^{29}Si and ^{13}C spectra. Simple surface functionalities such as chlorotrimethylsilane, 3-(trimethoxysilyl)propanethiol, and 2-(3,5-dinitrobenzamido)-2-phenylacetic acid were observed. The method proved to have a decent resolution as the authors succeeded in observing and assigning the different signals obtained from the various grafted molecules used.[32] Later, they were able to observe the modification of the grafted molecules on the silica surface after exposure to air, proving that SSNMR should be a powerful tool to study and monitor surface species.[33]

These experiments performed by Maciel and co-workers in the early 80s were the very first observation of surface supported species by SSNMR. Since then, steadily methodological and instrumental developments has allowed to provide a more and more detailed picture of single well-defined sites supported on surfaces. The combination of 2D HETCOR spectroscopy and ^{13}C isotopic enrichment allowed Petroff-Saint-Arroman *et al.* to report the detailed characterization of Mo carbyne species supported on $SiO_{2-(700)}$ obtained from SOMC.[34] Later, the introduction of efficient homonuclear decoupling schemes in SSNMR allowed the implementation of J-resolved experiments for surface species. Thus, it was used to evidence the presence of H agostic bonds on a Re-alkylidene supported metathesis catalyst.[35] Important features of well-defined supported catalysts were obtained using combination of isotopic labeling with CPMAS and HETCOR.[36, 37, 38] For example, Soignier *et al.* studied the deactivation process of Ta hydride supported on MCM-41 or $SiO_{2-(700)}$.[39]

In the previous examples, isotopic enrichment is used to circumvent the lack of sensitivity of SSNMR of surfaces. ^{1}H NMR spectroscopy has been investigated as ^{1}H is significantly more sensitive than heteronuclei. In 2004, ^{1}H single quantum (SQ) - double quantum (DQ) correlation NMR spectroscopy was exploited to differentiate ZrX and ZrX_2 species (where X stands for -H, -OH, or -C(=O)H) on a zirconium hydride supported on $SiO_{2-(700)}$.[40] In particular, the authors demonstrated the formation of mono- and bis-hydride surface species from the reaction of H_2 with silica supported $[(^t SiO)Zr(CH_2Bu)_3]$. They also studied the reactivity of these two active sites with three different reagents: NO_2, CO_2, and H_2O. Similar SSNMR approaches have been used to reveal the dissociation mechanism of the strong nitrogen-nitrogen triple bond in N_2 by H_2 on a silica-supported Ta active center. Specifically, DQ NMR allowed unambiguous assignment of imido and amido resonances formed upon the reaction of labeled $^{15}N_2$ with the surface Ta complex.[41, 42]

In 2005, Trébosc *et al.* applied fast magic angle spinning (MAS) (up to 45 kHz spinning frequency) to study allyl functional groups grafted on MCM-41 silica. They recorded ^{1}H spectra at different spinning rates and observed ^{1}H signals narrowing as expected by partial averaging of strong ^{1}H homonuclear coupling. Their ^{1}H NMR MAS spectra are reported in FIGURE 2.6. The assignment is not straightforward as ^{1}H are coming from the different surface silanol types but also from adsorbed water onto the silica surface. The authors carefully assigned ^{1}H signals using different partially dehydroxylated MCM-41 samples. When combining fast MAS with the Frequency-Switched Lee-Goldburg (FSLG) decoupling scheme, they did not observe any resolution improvements and attributed the remaining signal broadening to inhomogeneous contributions and chemical exchange.[43] Fast MAS also allowed them to implement a Carr-Purcell-Meiboom-Gill (CPMG) detection scheme to improve the sensitivity during the acquisition of ^{1}H-^{29}Si HETCOR spectrum at natural abundance.[44] In 2007, the same research group examined ^{1}H-detected schemes, based on the development of Ishii and Tycko,[45] for the acquisition of ^{1}H-^{13}C HETCOR spectra on organically functionalized mesoporous species. Their pulse program is represented on FIGURE 2.7, based on CP correlation with **(a)** ^{13}C detection and **(b)** ^{1}H detection. The detection of the ^{1}H has the advantage to be more sensitive because of the higher gyromagnetic ratio of the ^{1}H compared to ^{13}C nuclei. The authors reported a sensitivity gain of about 3.8, which is near to the theoretical value of 4.[46] The approach was also successfully applied on mesoporous silica nanoparticles functionalized with a rhodium phosphine complex.[47] In contrast to these two examples using through-space correlation, a through-bond correlation experiment with ^{1}H detection has been reported on organically functionalized mesoporous silica nanoparticles.[48] This has been enabled by a sequence based on refocused INEPT HETCOR with ^{1}H detection, as represented on FIGURE 2.8.

In 2010, Mao *et al.* studied the conformation of a fluorocarbon moiety (PFP) grafted onto mesoporous silica nanoparticles (MSN). This material is interesting for its highly hydrophobic surface and hence its capacity to catalyze esterification and dehydration processes. Using ^{13}C-^{19}F HETCOR, and ^{19}F-^{29}Si HETCOR (through-bonds and through-space versions of the experiments) in combination with computational chemistry, they were able to demonstrate the existence of two non-exchanging conformations. The organic moiety can fold to the surface (PFP-p) or stand upright (PFP-u) (see FIGURE 2.9**(a)** for the structure). FIGURE 2.9**(b)** and **(c)** respectively show the ^{13}C-^{19}F INEPT HETCOR and ^{13}C-^{19}F INEPT HETCOR spectra of MSN-PFP. They clearly demonstrate the existence of two different surface sites (PFP-p (red) and PFP-u (blue) in

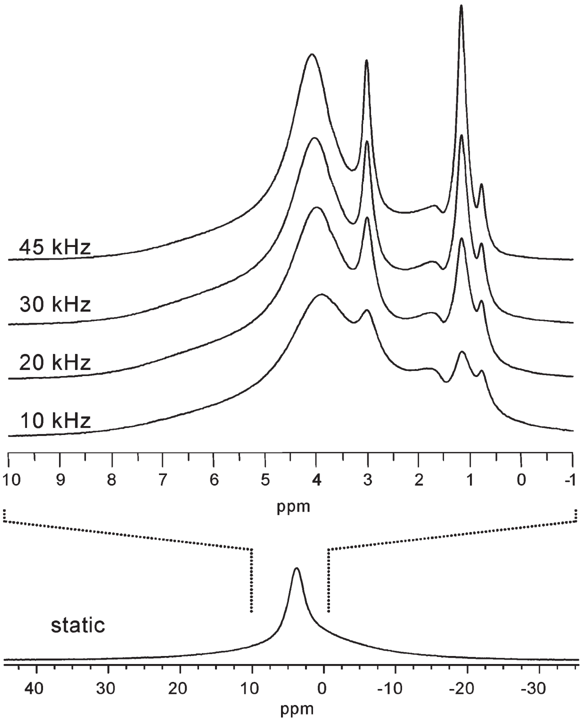

FIGURE 2.6: ^{1}H MAS NMR on MCM-41 as function of MAS rate. Reprinted with permission from [43]. Copyright 2005 American Chemical Society.

FIGURE 2.9**(b-c)**).[49] Later, the same group demonstrated that when PFP functionalized mesoporous silica nanoparticles were impregnated with heptane, only the PFP-p conformation was found. Thus, contact between hydrophilic surface silanols and heptane was avoided.[50]

SSNMR was shown to be suited for studying the dynamics of grafted surface molecules. In 2008, Blanc *et al.* studied the dynamics of a series of organometallic complexes supported on silica and found that the motions of the grafted molecules were not isotropic, likely due to the tethering of the molecules to the surface. They also discovered that the dynamics of the supported metal complex was dependent on the metal center.[51] In 2009, Gath and coworkers used ^{2}H NMR to study the motions on SBA-15 and aerosils silica.[52]

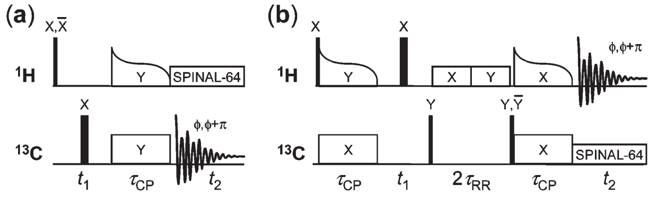
(a)
X,X̄
1H
Y
SPINAL-64
X
ϕ,ϕ+π
13C
Y
t1
τCP
t2
(b)
X
X
1H
Y
X
Y
X
ϕ,ϕ+π
Y
Y,Ȳ
13C
X
X
SPINAL-64
τCP
t1
2τRR
τCP
t2

FIGURE 2.7: CP-based HETCOR with **(a)** ^{13}C detection and **(b)** ^{1}H detection. Reprinted with permission from [46]. Copyright 2007 American Chemical Society.

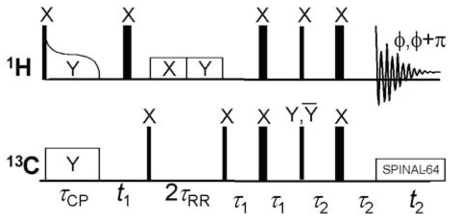
X
X
X
X
X
1H
Y
X
Y
ϕ,ϕ+π
X
X
X
Y,Ȳ
X
13C
Y
SPINAL-64
τCP
t1
2τRR
τ1
τ1
τ2
τ2
t2

FIGURE 2.8: ^{1}H detected INEPT-based HETCOR. Reprinted with permission from [48]. Copyright 2009 American Chemical Society.

In all these studies, SSNMR has proven to be a very powerful method to access both structural and dynamical properties of surface sites. However, isotopic enrichment and/or long accumulation times are necessary, mainly due to the poor sensitivity of SSNMR exacerbated by the dilution of the investigated molecules in the sample. Various approaches have been developed to address this sensitivity issue: higher magnetic fields, CPMG acquisition, or ^{1}H detection. In parallel, the use of a molecular surface models to mimic the surface, such as polyhedral oligomeric silsesquioxanes (POSS) (as surface silanol models) have been developed [53] and used for example in [54, 55]. In two decades, computational modeling of surfaces has become an increasingly important tool to complement the experimental data. Despite these efforts, sensitivity remains a critical bottleneck.

In the following section, I explain how hyperpolarization by Dynamic Nuclear Polarization in NMR can address the sensitivity issue for surface NMR spectroscopy.

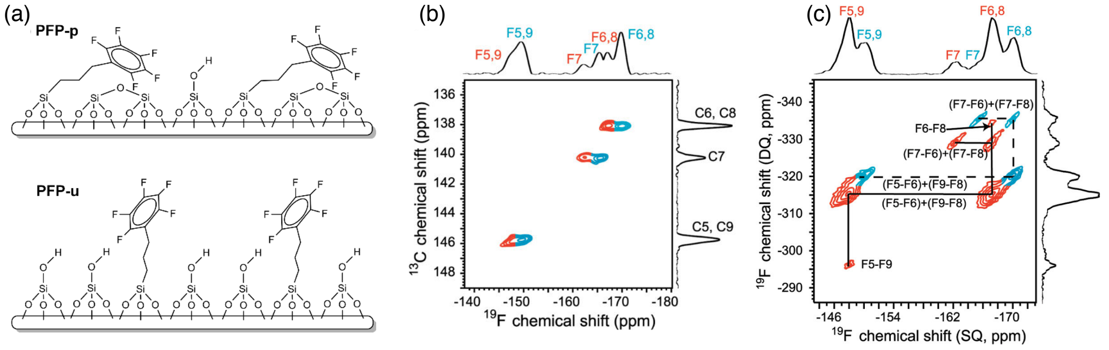

FIGURE 2.9: **(a)** Representation of the two surface conformations PFP-u and PFP-p on MSN-PFP. **(b)** ^{13}C-^{19}F INEPT HETCOR of MSN-PFP showing the two surface conformations PFP-p (red) and PFP-u (blue). **(c)** 2D ^{19}F-^{19}F DQMAS spectrum of PFP-MSN where DQ excitation and reconversion were achieved using the back-to-back (BABA) sequence, showing the two independent systems PFP-p (red) and PFP-u (blue). Reprinted (adapted) with permission from [49]. Copyright 2010 American Chemical Society.

2.4 Hyperpolarizing surfaces in NMR using Dynamic Nuclear Polarization

2.4.1 Introduction

Dynamic Nuclear Polarization (DNP) takes advantage of the gyromagnetic ratio of the electron which is 658 times higher in magnitude than the gyromagnetic ratio of ^{1}H nuclei. The thermal polarization of electrons in a magnetic field is thus considerably greater than nuclear polarization. DNP allows transferring this high polarization to nuclei and thus to observe nuclear spin polarization at a much higher level than that achieved by the Boltzmann equilibrium (so-called hyperpolarization). DNP is not a new discovery in the field of NMR; in 1953, Overhauser proposed a theoretical model showing that hyperpolarized metal nuclei can be obtained based on a cross-relaxation process between nuclei and saturated unpaired electrons.[56] This was experimentally demonstrated by Carver and Slichter a few months later.[57] Conducting electrons of metallic lithium were saturated resulting in a ^{7}Li NMR signal enhancement of about 100. FIGURE 2.10 depicts the ^{7}Li NMR spectrum obtained with and without microwaves.

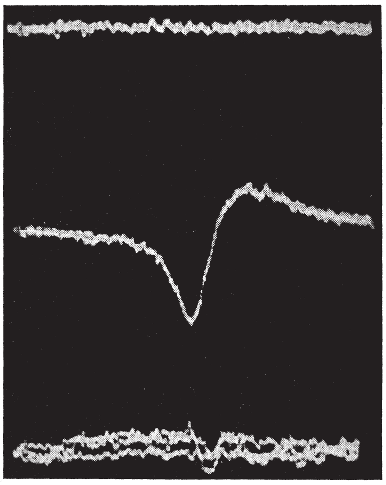

FIGURE 2.10: Oscilloscope pictures nuclear resonance absorption vs static magnetic field. Top: ^{7}Li resonance, with microwaves; middle: ^{7}Li resonance enhanced by electron saturation; and bottom: ^{1}H resonance in glycerin sample. Reprinted with permission from [57]. Copyright 1953 American Physical Society.

Although the first experiment was promising, efficient Overhauser Effect (OE) DNP demands short correlation times of the electrons spins and is thus mainly limited to mobile electrons in conductors or liquids. Solid Effect (SE) [58] and Cross Effect (CE) [59] were discovered a few years later, but they unfavorably scaled with the magnetic field. As high-power and high-frequency microwaves sources were not available at that time, DNP NMR has not been considered as a relevant field of NMR development for several decades.[60] The field reborn during the 90s with the pioneering work of Robert G. Griffin at the Massachusetts Institute of Technology (MIT) by combining newly available gyrotrons able to produce high-frequency and high-power microwaves to the design of DNP low temperature (LT) magic angle spinning (MAS) probes.[61, 62, 63] DNP NMR in the solid state is now a field in constant effervescence, and has been applied to a large number of systems ranging from small molecules in frozen solvents,[62] proteins,[64, 65, 66, 67] crystals and organic powders,[68, 69, 70] functionalized surfaces,[71, 72] nanoparticles,[73] microporous organic polymers,[74] etc. In particular, in the course of the thesis, MAS DNP NMR in the solid-state has been found to be particularly powerful to characterize surfaces.[71, 75] Thus, historical and more recent concepts in MAS DNP are reported in the current section.

2.4.2 Basics of Magic Angle Spinning Dynamic Nuclear Polarization in NMR

Continuous waves (CW) MAS DNP instrumentation

Before reviewing in more detail the recent developments in the field of MAS DNP, we will briefly describe current commercial MAS DNP instrumentation. As represented in Figure 2.11, the instrument is divided into two parts. The first one is a usual NMR magnet equipped with a LT-MAS probe, which can operate at temperatures around 100 K. The second magnet is equipped with a gyrotron tube that generates a continuous microwave irradiation. Commercial Bruker systems use 263 GHz, 395 GHz, and 527 GHz microwave frequencies for 400 MHz, 600 MHz, and 800 MHz NMR systems (^{1}H Larmor frequencies) respectively. The microwave beam is conducted to the NMR probe via a waveguide and used to irradiate the sample continuously.[76, 77]

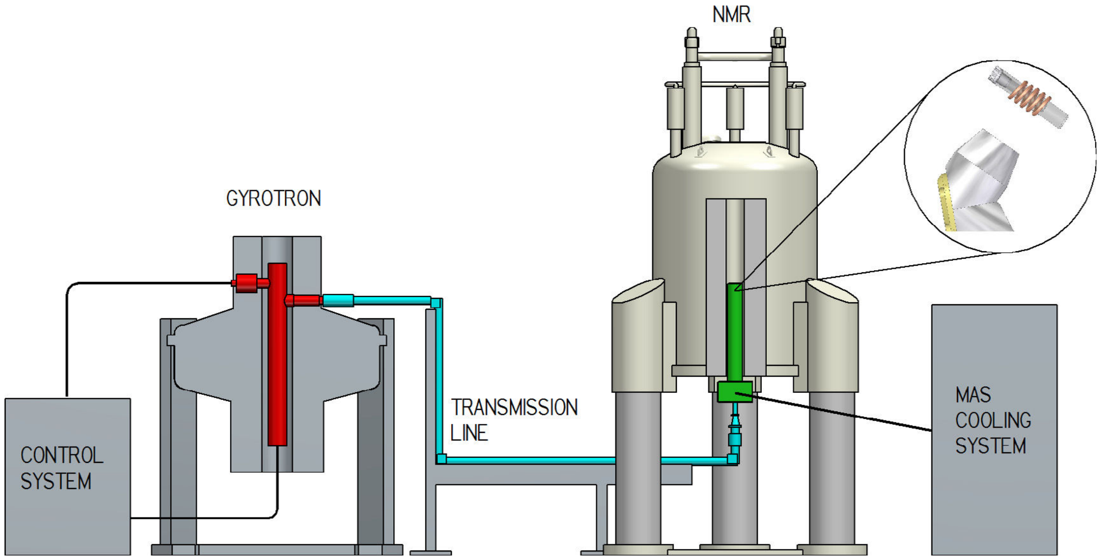

Figure 2.11: Commercial MAS DNP NMR system composed of a gyrotron, an NMR magnet, a wave guide, and a cryocabinet. Reprinted with permission from [77]. Copyright 2016 Elsevier Inc.

Irradiation of the sample with microwaves allows, under certain conditions, to transfer polarization from unpaired electrons to nuclei. The DNP enhancement is usually evaluated using the ratio of the NMR signal intensity of the sample with microwaves irradiation (I_{ON}) and without microwave irradiation (I_{OFF}):

$$\varepsilon = \frac{I_{ON}}{I_{OFF}} \tag{2.1}$$

To understand under which conditions electron to nuclei polarization transfer can occur, the principle mechanisms responsible for polarization transfer in MAS DNP are described in the following section.

DNP mechanisms

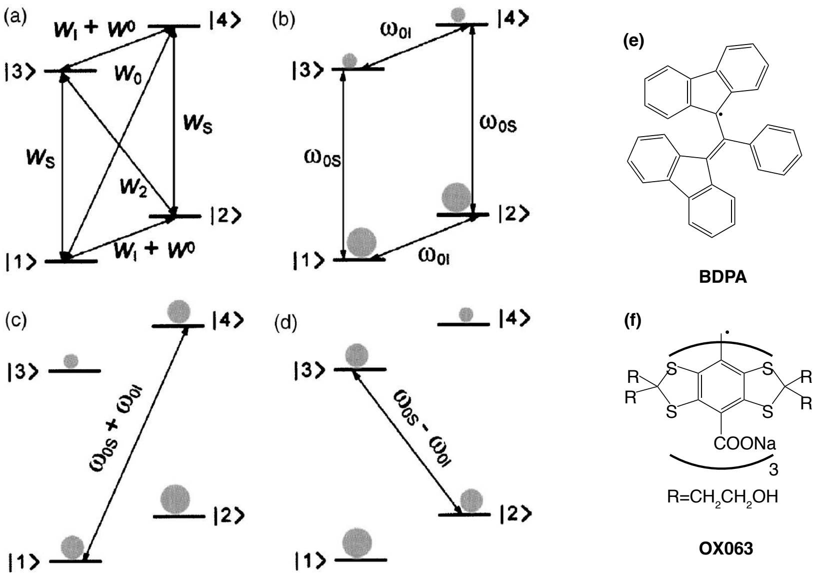

FIGURE 2.12: **(a-d)** Energy level diagrams relevant for the description of OE and SE. **(a)** Transition rates important for the OE. W_I and W_S are the SQ transition rates for respectively I and S spins. W_0 and W_2 are respectively the ZQ and DQ transition rates. W_I the interconversion rate. **(b)** Thermal equilibrium population for a two-level spin system. The spin population is depicted schematically in gray. **(c)** and **(d)** Saturation of the forbidden ZQ and DQ transitions leads to negative or positive enhancement through the SE. **(e)** BDPA structure. **(e)**OX063 (trityl radical) structure. Reprinted (adapted) with permission from [78]. Copyright 2008 American Institute of Physics (AIP)

The Overhauser Effect. As was already stated in the introduction, the very first evidenced DNP mechanism is the Overhauser Effect (OE). Let us consider a two-spin system of one electron and one nucleus represented in by the transition frequencies FIGURE 2.12**(b)** and transition rates 2.12**(b)(a)**. The OE is a cross-relaxation process between the two spins involving the zero-quantum (ZQ) and double-quantum (DQ) relaxation rates. In FIGURE 2.12**(a)** the ZQ transition occurs at a rate W_0 and the DQ transition at W_2. If these two relaxation rates are different, then saturation of the electron at its Larmor frequency results in an enhancement of the nuclear polarization. One can note that DQ and ZQ transitions are dominated by the fluctuation of the electron-nuclear coupling (hyperfine and dipolar couplings). The sign of the enhancement is determined by the ratio of the two relaxation rates: $W_2 < W_0$ results in a positive nuclear enhancement and $W_2 > W_0$ in a negative enhancement.[78, 79]

To be efficient, the OE requires the fluctuations of the hyperfine coupling at a frequency close to the Larmor frequency of the electron which was found possible in metals with free conducting electrons and in liquids.[57, 80] In insulating solids, OE was not expected to be very efficient. Surprisingly, in 2014, Can *et al.* were however able to observe sizeable OE DNP with the BDPA radical (see FIGURE 2.12**(e)**) dispersed in polystyrene and with its derivative water-soluble version SA-BDPA (sulfonated BDPA) in a glycerol/water mixture. Moreover, they have observed that, with BDPA, OE DNP scales favorably with the magnetic field as one can see in FIGURE 2.13. In this figure the central transition corresponds to OE DNP and increases when going from 9.4 T to 18.8 T.[81] OE DNP with BDPA has been recently rationalized, with the help of *ab initio* molecular dynamics simulations, and attributed to fluctuating hyperfine couplings at about 650 GHz in BDPA. Thus, moving from 263 GHz for 9.4 T (400 MHz ^{1}H frequency), 395 GHz for 14.1 T (600 MHz ^{1}H frequency), and 527 GHz for 18.8 T (800 MHz ^{1}H frequency), the fluctuation frequency of the hyperfine coupling gets closer to the electron Larmor frequency and hence the DNP enhancement increases.[82]

The Solid Effect. The Solid-Effect is a second DNP mechanism discovered in 1958.[58] Similarly to the OE, it can be described by the same two-spin system involving a nucleus and an electron represented in FIGURE 2.12. However, instead of saturating the electron, continuous microwaves irradiation occurs at the *forbidden* DQ or ZQ transitions.

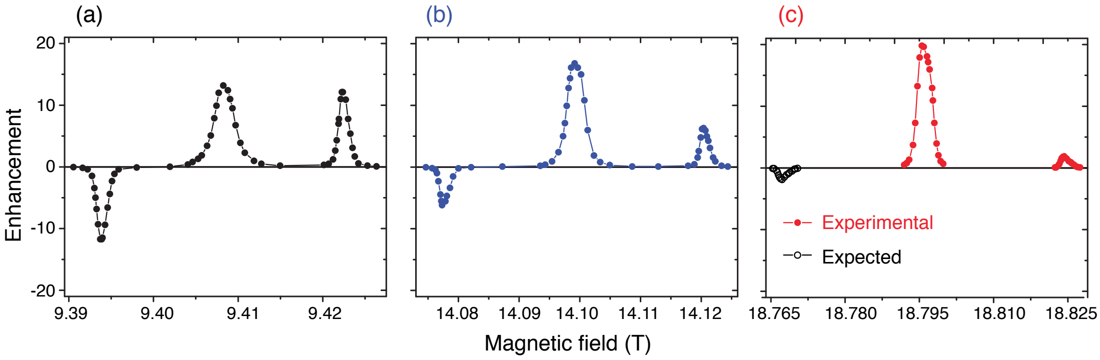

FIGURE 2.13: **(a)** ^{1}H enhancement magnetic field dependance with CW microwaves irradiation at 263 GHz on BDPA in polystyrene at 100 K and MAS rate of 8 kHz. The central transition corresponds to OE DNP and the two satellites to SE DNP. **(b)** and **(c)** represent the ^{1}H enhancement magnetic field dependance with CW microwaves irradiation at 395 GHz and 527 GHz respectively of the same sample under similar conditions. The OE DNP scales favorably whereas SE strongly decreases with magnetic field. Reprinted with permission from [81]. Copyright 2014 American Institute of Physics (AIP).

Similarly to the previous effect, saturation of ZQ or DQ will lead to a positive or negative enhancement. The principle of SE is that non-secular nuclear-electron coupling is responsible for a partial mixing of the two-spin (unperturbed) system thus resulting in *partially* allowing the DQ/ZQ transitions and driving the polarization transfer from the electron to the nucleus. As shown in FIGURE 2.12**(c)**, saturation of the ZQ transition results in negative enhancement whereas, as depicted in 2.12**(d)**, the saturation of the DQ transition results in positive nuclear enhancement.

SE is observed with BDPA. Indeed the ^{1}H enhancement magnetic field dependance curves reported in FIGURE 2.13 shows positive and negative enhancements due to the SE.[81] SE corresponds to the positive and negative satellites peak when microwaves irradiation saturate the ZQ and DQ transitions. SE is also observed on the organic radical trityl OX063 (see FIGURE 2.12**(f)** for the structure). To be efficient, the EPR linewidth should not exceed the nuclear Larmor frequency, otherwise positive and negative SE can occur at the same time and hence, cancel each other. SE has not attracted considerable attention in high-field DNP NMR as the efficiency of the transfer drops dramatically with the magnetic field (ω_0): it scales with the permanent field as ω_0^{-2}.[83, 78]

The Cross Effect. The Cross-Effect is a DNP mechanism first evidenced in 1963.[59] In non-rotating sample and under high fields, the CE mechanism can be understood as followed: let us consider a three-spin system constituted of two electrons and one nucleus. In Figure 2.14, the system is represented by eight energy levels. When the CE condition $\omega_{0,I} = |\omega_{0,e1} - \omega_{0,e2}|$ (where $\omega_{0,I}$ is the nuclear Larmor frequency, $\omega_{0,e1}$ the Larmor frequency of electron e1 and, $\omega_{0,e2}$ the Larmor frequency of electron e2) is matched, $|\alpha\beta\alpha\rangle$ and $|\beta\alpha\beta\rangle$ are degenerate as represented on Figure 2.14(**A**). When one electron EPR transition is saturated with continuous microwave irradiation (e1 in Figure 2.14(**B**)), the CE transition leads to nuclear polarization enhancement (negative enhancement in Figure 2.14(**C**)). Saturation of electron e2 will lead to positive enhancement.

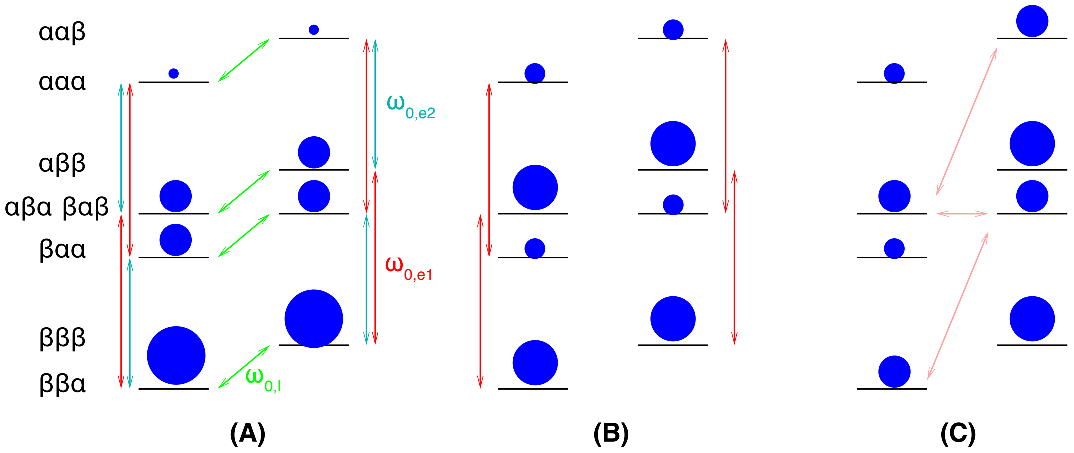

Figure 2.14: Representation of the energy levels of the three spin system: electron e1, electron e2 and nucleus I. Each level is labelled with its corresponding eigenvector given as $|m_{e_1} m_{e_2} m_I\rangle$. The CE condition is matched when there is degeneracy of levels $|\alpha\beta\alpha\rangle$ and $|\beta\alpha\beta\rangle$. Red, blue and green arrows represent respectively the single quantum transitions for e1, e2, and I. (**A**) gives the populations distribution at thermal equilibrium. (**B**) shows the effect of saturation of the EPR transition of e1 at $\omega_{0,e1}$ and (**C**) gives the distribution after CE transitions occured. Adapted from [78].

CE is usually performed with radicals exhibiting an inhomogeneously broadened EPR line, where the width of the EPR line is larger than the Larmor frequency of the nucleus.

Thus the CE can occur when two radicals close in space with the correct g-tensor orientations give EPR resonances that match the CE condition $\omega_{0,I} = |\omega_{0,e1} - \omega_{0,e2}|$.[78, 84] FIGURE 2.17 shows the EPR line TEMPO radical compared to the DNP enhancement measured on the system as a function of the magnetic field. The DNP transfer is dominated by the CE mechanism, and the two maxima correspond to optimized negative and positive CE conditions. In this model, the CE mechanism scales with the inverse of the magnetic field as the width of the inhomogeneously broadened EPR line scales (in Hz) with the magnetic field leading to a decreasing spectral density and lower microwave saturation efficiency.[84]

The CE mechanism under MAS has been intensively discussed recently. In particular, Thurber *et al.* and Mentik-Vigier *et al.* have shown the important role of level anti-crossings (LACs) occurring during the rotation of the sample at the magic angle.[85, 86] Corzilius recently schematically illustrated the CE MAS mechanism.[87] FIGURE 2.15**(a-b)** gives the central energy levels (color code in FIGURE 2.15**(d)**) and electron frequencies as a function of the MAS rotor position and FIGURE 2.15**(e)** is a spectral representation. In FIGURE 2.15**(e)-A**, one starts with two separate electron spin resonances. Then due to the rotation of the sample, electron frequencies evolve and one electron matches with the continuous microwaves irradiation, which causes (partial) saturation of this electron, this corresponds to event (1) in FIGURE 2.15**(a)** and is spectrally represented in FIGURE 2.15**(e)-B**. Then, in FIGURE 2.15**(e)-C**, the CE condition is matched, leading to polarization transfer from the electrons to the nuclei during the LAC. It corresponds to event (2) in FIGURE 2.15**(b)**, and one can observe the increased nuclear polarization during this event in the population representation FIGURE 2.15**(c)**. Then, moving to FIGURE 2.15**(e)-D**, the frequencies of the two electrons cross and thus exchange their polarization in a second LAC event. This is denoted as event (3) in energy-level representation FIGURE 2.15**(a-b)** and the exchange can be clearly seen on the population in FIGURE 2.15**(c)**. As rotation continues, a second CE LAC event occurs transferring more polarization to the nucleus. This second transfer is efficient because the two electrons just exchanged their polarization (as one can observe in panel FIGURE 2.15**(b-c)** when two CE events (2) happened successively, only the first one actually results in hyperpolarizing the nucleus). Then the second electron is saturated when crossing the continuous microwaves irradiation and the process continues. Note that in this model, LACs are supposed to be in adiabatic conditions thus driving the transfers. The transfer efficiency can be estimated using the Landau-Zener model.[85, 86, 87, 88]

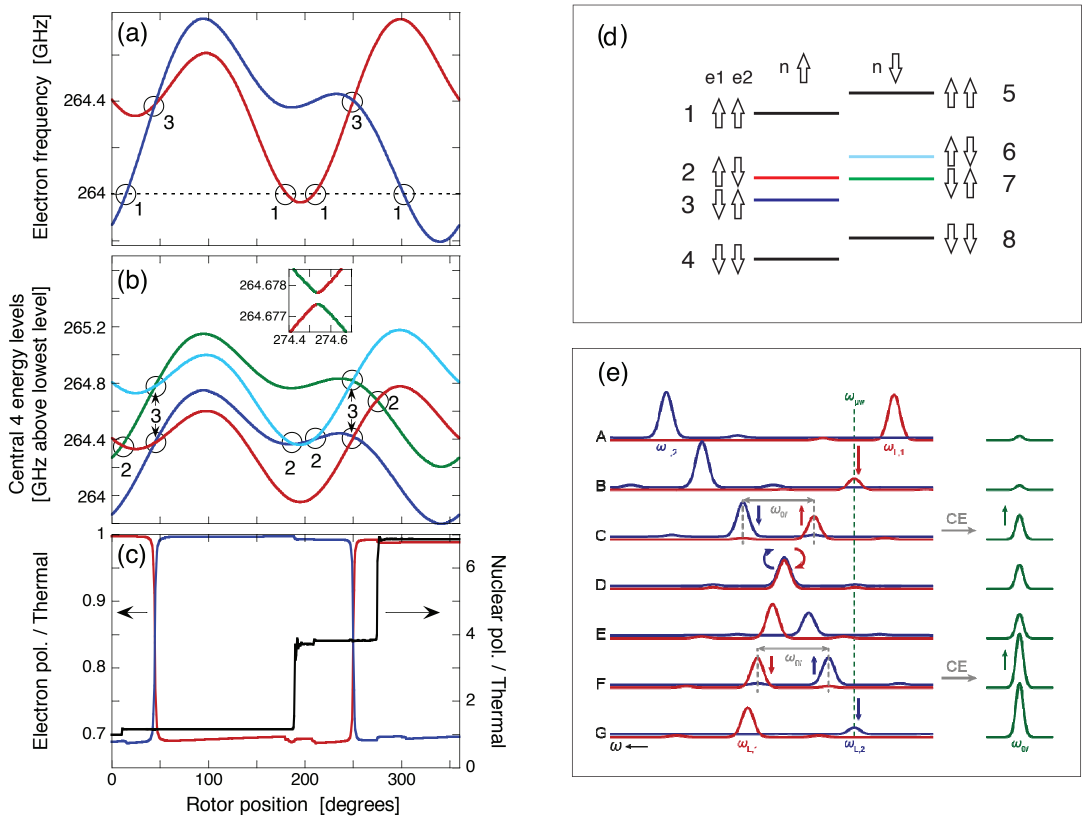

FIGURE 2.15: Simulated data for one orientation of a nitroxide biradical, as a function of the MAS rotor position angle: **(a)** EPR frequencies (blue and red lines) with microwave frequency indicated by dashed line; **(b)** central energy levels, color code according to **(d)**; **(c)** electron and nuclear polarization during the first rotor period. The energy LACs are circled: (1) EPR frequency crosses microwave irradiation; (2) EPR frequency difference matches the NMR frequency; (3) EPR frequencies cross. **(e)** Spectral representation of rotor events during MAS for CE. Details are given in the main text. Credits: **(a-d)** Reprinted with permission from [85]. Copyright 2012 American Institute of Physics (AIP); **(e)** Creative Commons Attribution 3.0 Unported Licence [87] - Published by the PCCP Owner Societies.

There is a fourth DNP mechanism coined Thermal Mixing. However, this mechanism is out of the scope of the present thesis as it is not significantly active in the conditions used for MAS DNP at low temperature (≈ 100 K).

Solvents in MAS DNP

As the materials studied by MAS DNP do not usually contain unpaired electrons, the sample needs to be doped with stable free radicals. These are typically stable organic radicals in aqueous media (e.g. water/glycerol) or organic solvents (e.g. 1,1,2,2-tetrachloroethane). MAS DNP experiments are usually performed at low temperature (LT) around 100 K and solvents are thus frozen. LT experiments are used because they lead to longer electron relaxation times and thus facilitate the saturation of the electrons with continuous microwaves leading to higher enhancements.[62]

An important property of the solvent is to avoid the aggregation of radicals upon cooling the sample to approx. 100 K. Radical aggregation would result in the formation of electron-concentrated regions leading to shortening of the electron relaxation times and thus to reduced DNP enhancement.[89] Hence, glassy solvents are usually used in MAS DNP experiments such as water/DMSO,[90] water/glycerol.[91] In 2012, Zagdoun *et al.* compared different organic solvents for MAS DNP applications. They found that the best non-aqueous systems rely on halocarbon solvents such as 1,1,2,2-tetracholoroethane or 1,2-dichloroethane.[92]

Interestingly, the protonated frozen solvent provides a solid matrix, so-called DNP matrix, where ^{1}H-^{1}H spin diffusion, driven by ^{1}H homonuclear couplings, can efficiently distribute the hyperpolarization through the entire sample. Spin diffusion is particularly relevant as in most MAS DNP experiments direct DNP transfer occurs between the electron and ^{1}H and then ^{1}H hyperpolarization is transferred via CP to heteronuclei. ^{1}H-^{1}H spin diffusion numerical models of Van Der Wel *et al.*[68] and later Rossini *et al.*[69] have demonstrated the importance of this process in MAS DNP experiments.

Some experimentations have been performed without the use of a solvent. For example, De Paëpe, Hediger, and co-workers have developed a matrix-free approach for MAS DNP where the polarizing agents are anchored to the sample of interest using a *gluing* agent. They demonstrated the applicability of the method for microcrystalline cellulose, lysozyme, and liposomes.[93, 94, 95]

Recently, the suppression of the solvent resonances in DNP MAS experiments has been proposed. As described in reference [96], coherence lifetimes of frozen solvent (TCE or water/glycerol) are usually significantly shorter than those of the materials of interest (surfaces and microcrystalline powders in their studies), and thus solvent signals can be filtered out using spin echoes or spin-lock. In [97], the authors propose to use deuterated solvent and reintroduce ^{2}H-^{13}C dipolar couplings of the deuterated solvent to quickly dephase ^{13}C solvent signals.

Rational development of DNP polarizing agents

Development of optimized radicals has attracted wide attention from the NMR community in the last decade. The general objective here is to approach the maximum theoretical DNP enhancement of 658 for ^{1}H nuclei. The development of polarizing agents has mainly focused on CE DNP as the scaling of SE with the magnetic field is strongly unfavorable. For ^{1}H OE DNP in insulating solids, so far no other efficient radicals, except BDPA and its derivative SA-BDPA are known. The structure of the polarizing agent discuss in the current section are depicted in FIGURE 2.16.

In the 90s, TEMPO was the first radical investigated in DNP MAS. TEMPO is a stable nitroxide exhibiting a broad EPR spectrum in frozen solution and that can perform CE DNP. In 2004, Hu *et al.* proposed to use biradical to control the electron-electron dipolar coupling and reported polarizing agents constituted of two tethered TEMPO units (bis-TEMPO-n-ethyleneglycol: bTnE represented on FIGURE 2.16). They observed an increase of the DNP enhancement by a factor of about 4.[90] The water-soluble biradical TOTAPOL introduced in 2006 followed the same principle and the authors reported a DNP enhancement of 290 on ^{1}H. One year later, the concept of using rigid tether was introduced.[98] As stated before, only the association of molecules with an orientation of the g-tensor that allows matching with the CE condition gives rise to effective CE. Thus, using rigid tethers allows imposing the appropriate relative orientation of the g-tensor of the TEMPO units of the biradical. While authors reported a ^{1}H enhancement of 260 for bT2E, they obtained 325 under the same experimental conditions ($\approx$ 80 K, 211 MHz NMR magnet under 160 GHz microwaves continuous irradiation), with the rigid biradical bTbK (see structure on FIGURE 2.16). Later, Zagdoun *et al.* introduced bulkier radicals in order to increase the electron relaxation times (T_{1e} and T_{2e}) improving EPR saturation upon continuous microwaves irradiation. This lead to the design of TEKPOL, depicted in FIGURE 2.16, that can provide ^{1}H enhancements of 200, outperforming bTbK that gives ^{1}H enhancement of 50 under the same conditions (≈ 105K, 400 MHz NMR magnet, 263 GHz gyrotron).[99, 100] The same concept has been used for the design of AMUPOL (FIGURE 2.16), which is – to date – the best polarizing agent in aqueous solvents (water/glycerol).[91] In 2016, Kubicki *et al.* published a comparison of 37 CE biradicals in which they carefully compared the respective DNP performances and correlated them to the radical substituents. TEKPOL2 was introduced and with a DNP enhancement factor of 215 (≈ 105 K, 400 MHz NMR magnet, 263 GHz gyrotron) is slightly better than TEKPOL.[101] The careful analysis of this exhaustive series of biradicals lead to the conclusion that at a moderate magnetic field (400 MHz), the polarizing agent – by itself – does not prevent from reaching the maximum theoretical DNP enhancement and that other parameters should be identified to reach this maximum. For example, in reference [102], the same authors observed that the DNP enhancement can be doubled by incorporating dielectrics particles (*e.g.* KBr) in the rotor, thus achieving a better distribution of the microwave field in the sample.

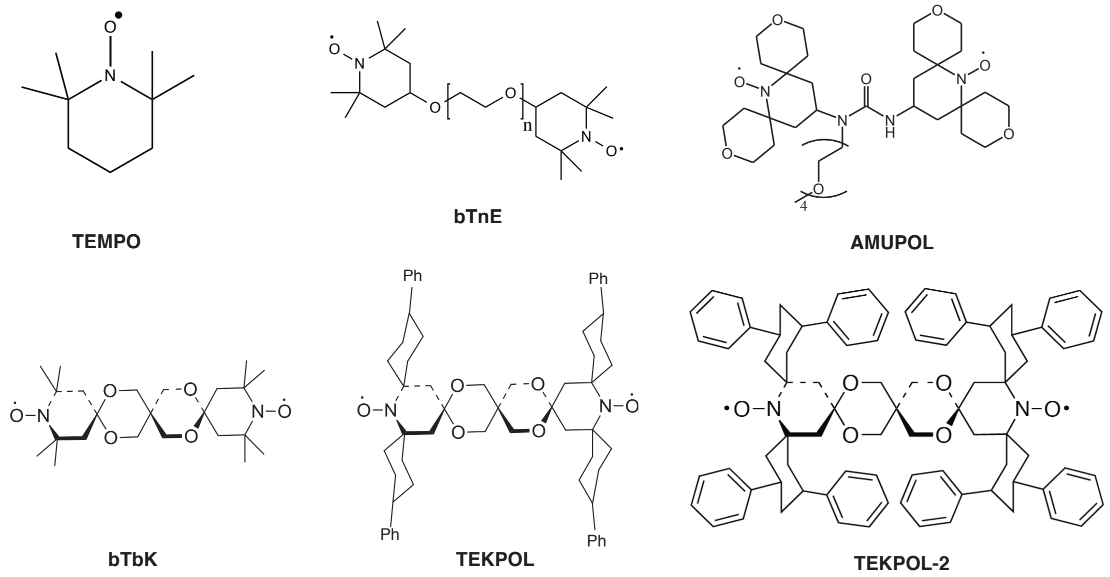

FIGURE 2.16: Structures of some landmark CE nitroxide-based polarizing agents.

Currently, research is focused on obtaining polarizing agents that can provide high

DNP enhancements at a very high magnetic field (800 MHz) where the standard AMUPOL and TEKPOL under-perform. As already discussed, the BDPA radical is giving efficient OE DNP and providing a promising enhancement at 800 MHz.[81] Another approach that has been investigated to obtain optimized CE polarizing agents is to mix two different radicals. In 2007, a mixture of 20 mM TEMPO and 20 mM trityl was examined and yielded a DNP ^{1}H enhancement of about 160 (which should be compared to an enhancement of 50 obtained under similar conditions with 40 mM TEMPO). FIGURE 2.17**(a-b)** shows the field profiles of the radical trityl (SE) and TEMPO (CE). The superposition of the two EPR profiles shows that the difference between the narrow line EPR spectrum of trityl and the maximum (at the top of the field plot) of the integrated EPR line of TEMPO perfectly matched the Larmor frequency of the ^{1}H in their 5 T magnet. As the CE condition matches between the two radicals, the possibility to observe CE DNP between TEMPO and trityl in a TEMPO/trityl mixture was predicted. FIGURE 2.17**(c)** shows that this expected CE in the mixture was actually observed.[84] The same idea was used in reference [103] where a mixture of trityl and BDPA was investigated. In this paper, the difference between the two narrow line EPR frequencies matches with the ^{13}C Larmor frequency under the given working conditions. Very recently, Mathies *et al.* went further and reported the investigation of mixed radicals made of a TEMPO unit tethered to a radical trityl, coined TEMTriPol (represented on FIGURE 2.17**(d)**).[104] The influence of the tether has been considered. In particular they introduced TEMTriPol-1, represented in FIGURE 2.17**(d)**, which generated a ^{1}H enhancement of 65 at 800 MHz, and more importantly they observed that this ^{1}H enhancement scaled favourably with the magnetic field. Although the electron-electron interaction in the TEMPO/trityl mixture is a dipolar interaction, the authors' calculations showed that there was a very high electron-electron exchange interaction in TEMTriPol-1. The authors correlated the important enhancement observed for TEMTriPol-1 and its field dependance to this unusual exchange interaction. Usually, in binitroxide radicals, the electron-electron dipolar coupling drove the CE transition, and the exchange interaction is negligible. The authors noted that this strong exchange interaction was only efficient at a higher field as they attributed CE DNP enhancement at low field (211 MHz) to intermolecular dipolar interactions between nitroxide units for TEMTriPol-1.

Finally, note that metal complexes are currently under investigation in the group of

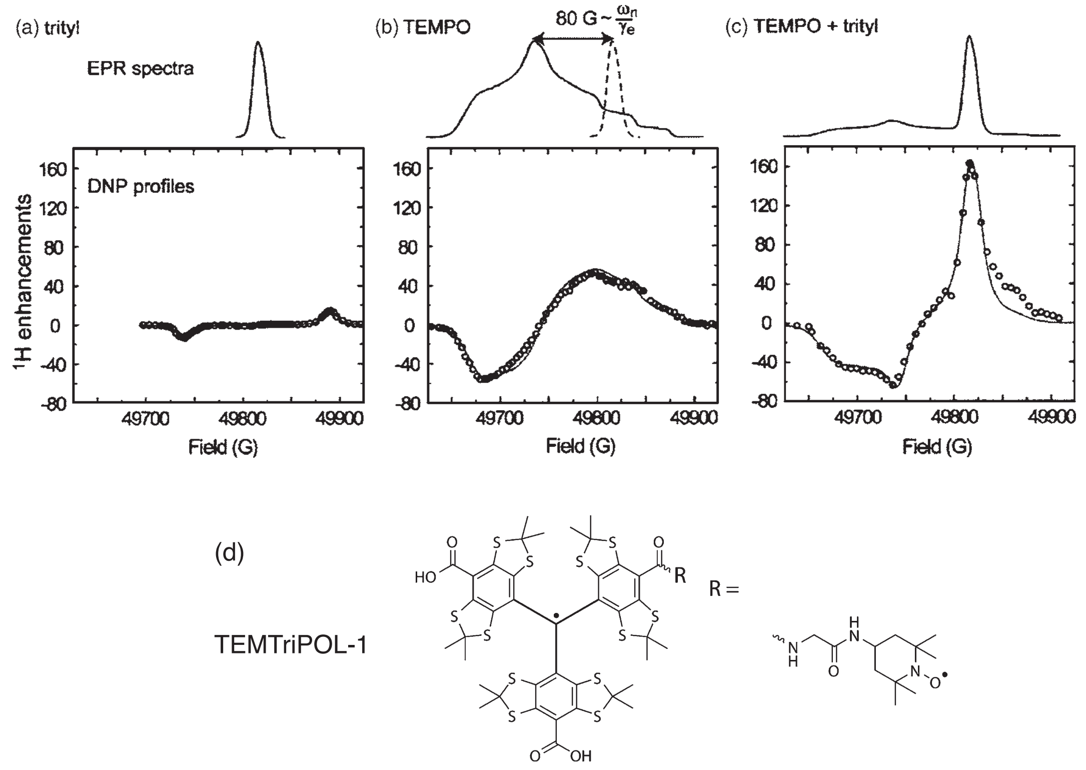

FIGURE 2.17: **(a)** Integrated EPR profile of trityl and the ^{1}H enhancement as function magnetic field with microwave irradiation at 139.66 GHz. The positive and negative enhancement peaks correspond to SE DNP, when ZQ and DQ transition are irradiated. **(b)** The same representation for TEMPO, which exhibits a broad EPR profil resulting in CE DNP. **(c)** The same representation for a mixture of trityl and TEMPO. Credits: **(a-c)** Reprinted with permission from [84]. Copyright 2007 American Institute of Physics (AIP). **(d)** Reprinted with permission from [104]. Copyright 2015 Wiley-VCH.

Corzilius. In particular, biradicals made of two Gd(III) complexes tethered have been investigated and reported for direct DNP on ^{1}H, ^{13}C, and ^{15}N [105] in parallel with the development of a new theory for CE and SE DNP for high spin metal complexes.[87]

All the mechanisms presented so far require the saturation of EPR line continuous microwaves, which usually requires working at low temperature to ensure efficient saturation. Thus most MAS DNP experiments are conducted at temperatures around 100 K.

In the next section, I will report on the temperature dependence of DNP enhancements.

Temperature

In 2013, Ong *et al.* evaluated if *ortho*-terphenyl (OTP) might be a suitable solvent for MAS DNP experiments. It is a frequently used matrix in EPR measurements where it is known to provide a rigid glassy medium.[106] As illustrated in FIGURE 2.18**(a)**, the sample should be carefully prepared to ensure the formation of a glassy OTP phase, and the authors showed that the formation of a crystalline phase results in poorer DNP performance. Moreover, they found that using deuterated OTP (95% deuteration) results in better DNP enhancement. Later Lelli *et al.* found that using the system TEKPOL/OTP gives a better DNP performance than the TEKPOL/TCE system ($\varepsilon_H = 240$ and $\varepsilon_H = 200$ respectively in a 9.4 T magnet, 105 K, MAS rate 8 kHz). They also demonstrated that BDPA and TEKPOL dispersed in OTP can provide efficient DNP up to the glass transition temperature of OTP ($T_g = 243$ K) as illustrated on FIGURE 2.18**(b-c)**. They hypothesized that above T_g, increased motions lead to a shortening of the electron relaxation times and hence to a lower DNP enhancement.[107]

Oschkinat and co-workers proposed to use high temperatures to improve the resolution of proteins studied by MAS DNP NMR, which is one of the major issues preventing a larger adoption of DNP for structural biology in solid-state NMR.[65] Using TOTAPOL in the glycerol/water matrix, they observed an important loss of DNP performance but also the concomitant improvement of NMR resolution.

NMR signal quenching in MAS DNP

For the moment, the quantification of the efficiency of MAS DNP experiments was limited to the sole evaluation of the DNP enhancements factor ε. However, it was shown that ε is not sufficient to reflect the quality of the MAS DNP experiments. This topic is discussed in the following section.

In 2012, Rossini *et al.* introduced the concept of overall sensitivity enhancement.[60] In MAS DNP, the common way to measure the DNP performance is to evaluate ε as the ratio of the signal intensity with microwaves and the signal intensity without microwaves. In principle, this is not sufficient to evaluate the sensitivity gain between

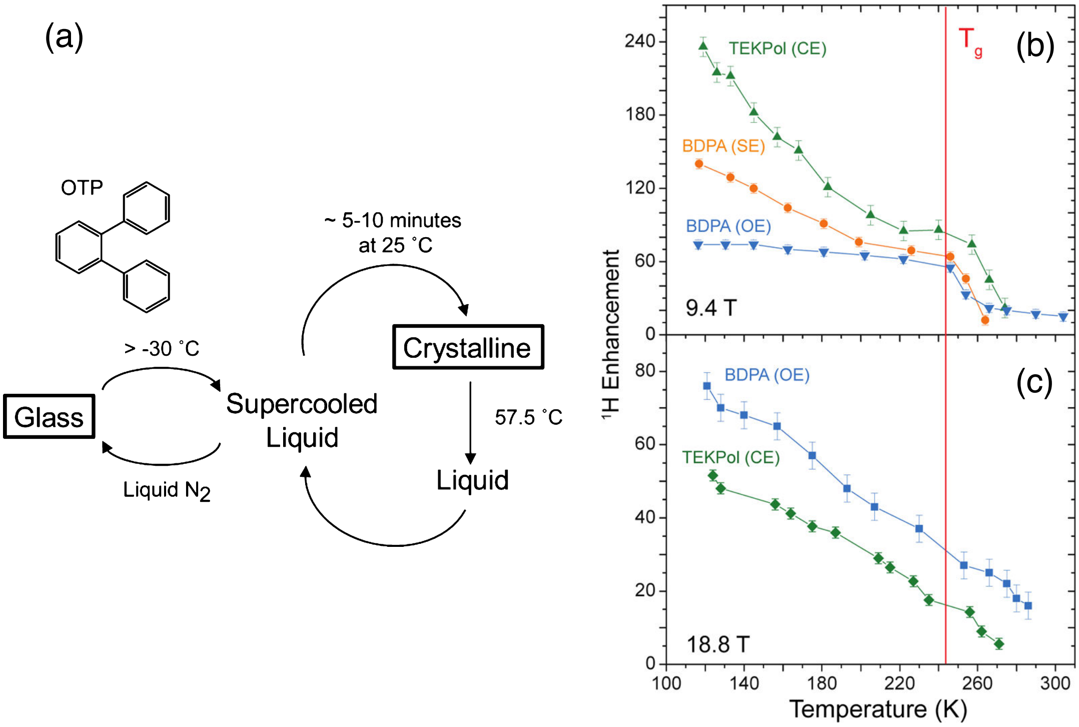

FIGURE 2.18: **(a)** Phase transition of *ortho*-terphenyl (OTP). **(b)** Temperature dependance of ^{1}H enhancement for 32 mM BPDA in OTP or 16 mM TEKPOL in OTP-d$_1$4 at 9.4 T and 18.8 T. T_g shows the glass transition temperature of OTP. Credits: **(a)** Reprinted with permission from [106]. Copyright 2013 ACS. **(b-c)** Reprinted (adapted) with permission from [107]. Copyright 2015 ACS

a MAS DNP NMR experiment performed at low temperature to a conventional MAS SSNMR experiment performed with a dry sample at room temperature. Indeed, paramagnetic species are introduced, thus inducing a partial loss of NMR signals due to paramagnetic quenching. Also, the effect of temperature and the recycling delay needs to be taken into account. In [60] the overall sensitivity enhancement was then defined as:

$$\Sigma^{\dagger} = \varepsilon \times \theta \times \sqrt{\frac{T_1}{T_{DNP}}} \frac{298 \text{ K}}{100 \text{ K}} \qquad (2.2)$$

where ε is the DNP enhancement, T_1 the spin-lattice relaxation time measured on an undoped sample at room temperature, T_{DNP} is the build-up time measured on a doped sample under MAS DNP conditions with microwaves. θ is the contribution factor, i.e.

the fraction of nuclei that still contribute to the NMR signals after the introduction of the paramagnetic polarizing agent:

$$\theta = \frac{I_{\text{doped sample},\mu wOFF}/m_{\text{doped sample}}}{I_{\text{undoped sample},\mu wOFF}/m_{\text{undoped sample}}} \tag{2.3}$$

In reference [108] a similar expression was introduced to correctly quantify the sensitivity in the MAS DNP approach.

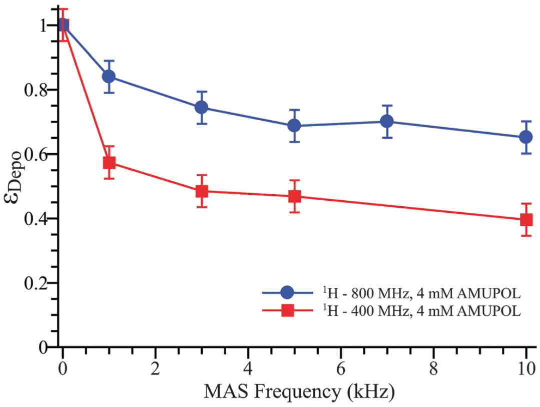

FIGURE 2.19: Depolarization factor ε_{depo} (ratio between the integrated NMR intensity of the sample under rotation at the magic angle and the static sample) for 4 mM AMUPOL in glycerol/water. Reprinted with permission from [109]. Copyright 2015 Phys. Chem. Chem. Phys. Owner Societies.

While the previous equation 2.2 can reflect the overall sensitivity gain in MAS DNP experiments, it does not provide insights into the mechanism that leads to the reduction of the NMR signal upon radical addition. In particular, in 2014, the concept of depolarization when biradicals are used in combination with magic angle spinning has emerged.[109, 110, 111] In [109], a depolarization factor ε_{depo} was defined as the ratio between the integrated NMR intensity of the sample under rotation at the magic angle and the static sample. FIGURE 2.19 depicts the evolution of ε_{depo} as function of the MAS rate for a solution of 4 mM AMUPOL in glycerol/water at 400 and 800 MHz at approx. 100 K. One can observe that under rotation at the magic angle spinning the signal intensity of a sample doped with AMUPOL dramatically decreases compared to static conditions, demonstrating that MAS is here inducing an additional quenching effect. Even stronger depolarization effects have been observed at a lower temperature

(≈ 25 K).[111] This effect has been interpreted as a loss of polarization compared to Boltzmann equilibrium due electron-electron dipolar rotor events when CE polarizing agents are present.[111, 109]

Finally, I finish this general section about MAS DNP NMR by mentioning the very most recent development in the elaboration of pulsed DNP schemes in the next section.

Pulsed Dynamic Nuclear Polarization

In the previous sections, all the results reviewed rely on continuous wave DNP where the sample is continuously irradiated with monochromatic microwave beam. The Griffin Group at the MIT is currently investigating the possibility to use pulsed microwaves and implementation of pulsed DNP schemes. The major motivation is that this approach could, in principle, circumvent the unfavorable field dependence of CW DNP used today. However, this demands instrumentation development, as no commercial systems are available today to conduct these experiments.

The NOVEL experiment (Nuclear Spin Orientation via Electron Spin Locking) introduced in 1988; is in principle similar to Hartmann-Hahn Cross Polarization where two different spins are spin-locked in a double rotating frame.[112, 113] In the original NOVEL paper in 1988, the authors were able to obtain a nuclear enhancement of about 10 using a single crystal of silicon doped with boron acceptors in a 0.28 T magnet.[112] Can *et al.* recently re-visited the NOVEL experiment and applied it to current DNP systems. At 270 K and 0.35 T, an enhancement of 323 was observed with BDPA dissolved in partially deuterated polystyrene.[114] Enhancements of 430 was obtained at 80 K and 0.28 T with the radical trityl OX063.[115] In 2017, the RA-NOVEL (Ramped-amplitude NOVEL) experiment has been introduced, where a ramp shape is used for the microwave locking pulse, leading to an improvement of NOVEL by a factor of about 1.6.[116] The recent revisit of the Integrated Solid Effect (ISE) can also be mentioned here, originally introduced in 1988,[117] modified to FS-ISE (Frequency Swept ISE).

The current section was very general and dedicated to introducing general concepts and recent developments of the MAS DNP method. In the next section, MAS DNP applied to surfaces is analyzed in more detail.

2.4.3 MAS DNP applied to Surfaces

The DNP SENS approach

In a pioneering experiment in 2010, MAS DNP was used to analyse a phenol-functionalized SBA-15 silica, using a novel approach named DNP SENS (DNP Surface Enhanced NMR Spectroscopy). The incipient wetness impregnation technique was used to infuse the porous material with a polarizing agent solution (TOTAPOL dissolved in glycerol/water in that case).[71] As represented in FIGURE 2.20, the continuous irradiation of the sample with microwaves allows the transfer of electron polarization to adjacent ^{1}H, then ^{1}H-^{1}H spin diffusion – mediated by the frozen solvent matrix – distributes the hyperpolarization through the sample. Finally ^{1}H hyperpolarization is transferred to ^{13}C via cross-polarization. The authors were able to obtain ^{13}C CPMAS spectrum within minutes, reported in FIGURE 2.20 and in 4 h the ^{1}H-^{13}C HETCOR spectrum without the help of isotopic labeling. It was also quickly possible to record a ^{29}Si CPMAS and a ^{1}H-^{29}Si HETCOR DNP SENS spectrum on similar materials at natural isotopic abundance.[72]

DNP SENS formulation

While DNP SENS were promising, it was still far from being optimized and thus providing the highest DNP sensitivity gains possible. Moreover, although the development of new polarizing agents for MAS DNP offered more and more efficient hyperpolarization, there were additional parameters that needed to be taken into account when MAS DNP was applied to materials and not only to bulk solutions (pure solution of polarizing agent) and it is reported in the next paragraphs.

Biradical concentration. The biradical concentration was the first and the most straightforward parameter to optimize. In reference [99], to ensure the highest sensitivity gain for surface signal, the authors measured the overall sensitivity gain $\Sigma^{\dagger}_{\mathrm{Si}}$ as function of the bTbK concentration. As shown in FIGURE 2.21, the increase of biradical concentration lead to an important decrease of the contribution factor θ_{Si}. Thus $\Sigma^{\dagger}_{\mathrm{Si}}$ allowed to weight the optimisation of DNP enhancement $\varepsilon_{\mathrm{Si}}$ by θ_{Si}. It was found that the optimized concentration of bTbK dissolved in TCE was 16 mM.

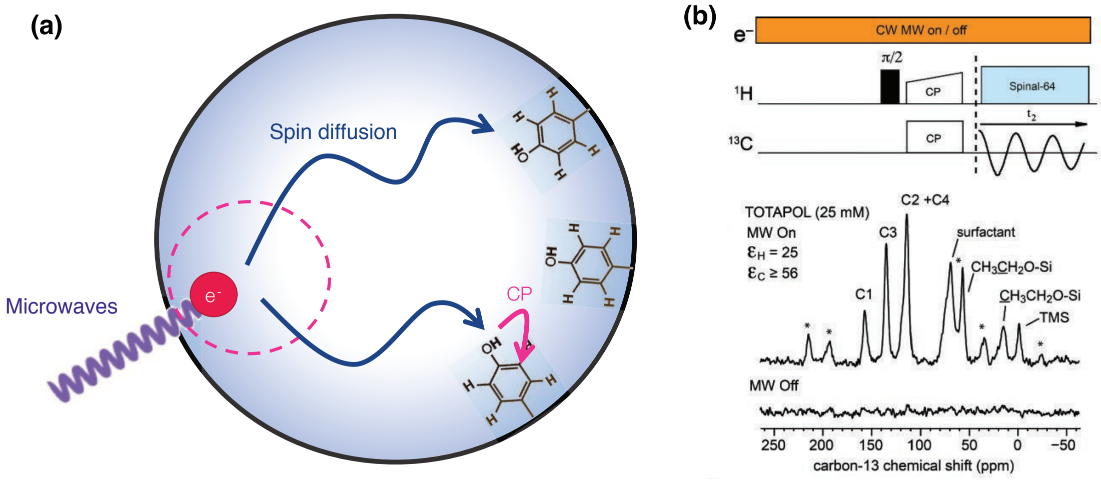
(a)
Spin diffusion
Microwaves
e-
CP
OH
H
(b)
e−
CW MW on / off
π/2
1H
CP
Spinal-64
t2
13C
CP
TOTAPOL (25 mM)
MW On
εH = 25
εC ≥ 56
C2 +C4
C3
C1
surfactant
CH3CH2O-Si
CH3CH2O-Si
TMS
*
MW Off
250
200
150
100
50
0
−50
carbon-13 chemical shift (ppm)

FIGURE 2.20: **(a)** Description of the DNP SENS experiment. **(b)** ^{13}C DNP SENS CPMAS spectrum, recorded on a phenol-functionalized SBA-15 silica impregnated with a 25 mM TOTAPOL solution in glycerol/water, at natural isotopic abundance (9.4 T, 105 K). Clear signals arise from the phenol functionality (atom labels are given in **(a)**), aliphatic signals were assigned to ethyl surface moieties remaining from the material synthesis. Reprinted with permission from [71]. Copyright 2010 ACS.

Silica surface passivation. As described in the section 2.2.2, as-synthetized silica exhibits surface silanols that can be post-modified to tune the hydrophobicity of the surface. In reference [118], the influence of different passivating groups has been investigated, they are shown in FIGURE 2.23. In particular, the presence of methyl groups has a substantial impact on the DNP performance: an enhancement $\varepsilon_{\mathrm{Si,CP}} = 9$ was measured when the surface was passivated with trimethylsilyl whereas $\varepsilon_{\mathrm{Si,CP}}$ reached 74 using deuterated trimethylsilyl passivating groups. The increase of the enhancement has been interpreted as methyl groups acting as relaxation sinks that prevent high DNP enhancements.

DNP SENS on porous materials

As functionalized porous silica is a versatile material class, described in section 2.2 of this manuscript, the beginning of DNP SENS has focused on the description of porous silica. For example, DNP have allowed following chemical reactions on surfaces using

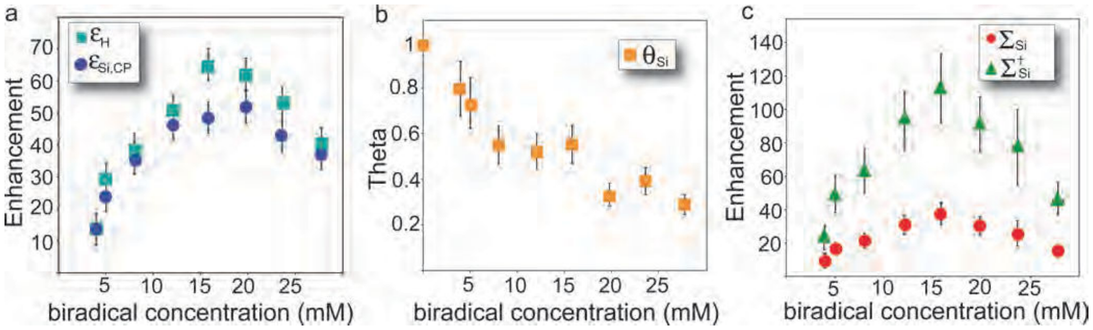

FIGURE 2.21: **(a)** ^{1}H enhancement (ε_{H}) and ^{29}Si enhancement (via CP, $\varepsilon_{\mathrm{Si,CP}}$) recorded on azide-functionalized SBA-15 silica with different concentrations of bTbK in TCE. **(b)** ^{29}Si quenching factor (θ_{Si}) as a function of the bCTbK concentration in TCE. (c) The overall sensitivity enhancement $\Sigma^{\dagger}_{\mathrm{Si}}$ takes the temperature into account, whereas Σ_{Si} does not taking it. Reprinted with permission from [99]. Copyright 2012 ACS.

^{13}C, ^{15}N CPMAS and 2D HETCOR spectra, as reported in FIGURE 2.22. In 2013, Samantaray *et al.* studied a ruthenium complex immobilized on SBA-15 silica. They were able to indirectly observe interactions between the metal and the silica surface when a flexible linker was used to anchor the organometallic complex to the surface. However, they found that a rigid linker prevents this interaction. These interactions were assumed to be able to increase the chemical lifetime of the supported Ru complex.[119] In 2015, similar interactions were qualitatively observed on an Ir(I) catalyst immobilized on SBA-15. These stabilizing interactions were believed to rationalize the exceptional capability of the supported Ir(I) catalyst to realize the hydrogenation of trans-stilbene whereas its molecular analog was far less active.[120]

DNP SENS was also applied to Metal Organic Frameworks (MOFs). The latter are an important class of materials attracting considerable attention for their possible application in gas storage, gas separation, and heterogeneous catalysis. They consist of a crystalline 3D network where organic ligands are connected via metallic centers.[121] In [122], DNP SENS enabled the use of $\{^{1}\mathrm{H}\}$-^{15}N CPMAS at natural ^{15}N isotopic abundance on N-functionalized MOFs. Interestingly, the authors noted the DNP enhancement ε evolved from 7 to 13 by simply allowing the non-functionalized MOFs - impregnated with a bCTbK solution in TCE - sample to *rest* at room temperature for 25 h. They

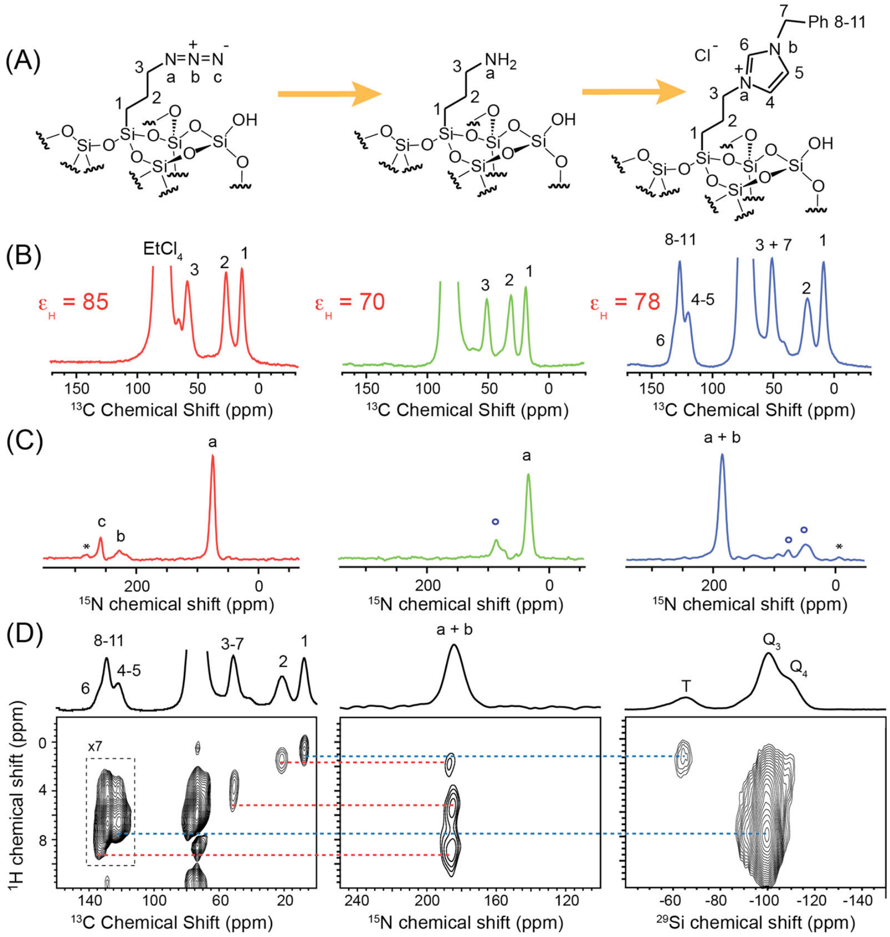

FIGURE 2.22: **(A)** Structure of functionalities immobilized on SBA-15 silica surface, Mat-PrN$_3$, Mat-PrNH$_2$, and Mat-PrIm **(B)** ^{13}C DNP SENS CPMAS spectra. **(C)** ^{15}N DNP SENS CPMAS spectra. **(D)** ^{1}H-^{13}C, ^{1}H-^{15}N, ^{1}H-^{29}Si DNP SENS HETCOR spectra of Mat-PrIm. The open circles indicate byproducts or incomplete conversion from the previous synthetic steps. Reprinted with permission from [75]. Copyright 2013 ACS.

did not observe a similar effect on the functionalized MOFs. The authors hypothesized that the polarizing agent (bCTbK) was blocked outside the pores due to its size and can slowly diffuse in the porous materials in the case of non-functionalized MOFs, however, this diffusion was hindered by organic moieties in N-functionalized MOFs. Moreover, as the radicals did not enter entirely into the material, the authors suggested that this

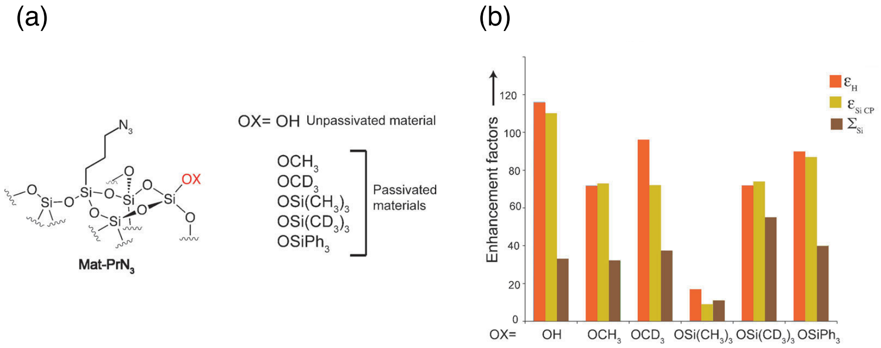

FIGURE 2.23: **(a)** azide functionalized SBA-15 silica and the passivating groups studied. **(b)** ^{1}H enhancement (ε_{H}), ^{29}Si enhancement (via CP, $\varepsilon_{\mathrm{Si,CP}}$), and sensitivity enhancements Σ_{Si} for the material with different passivating groups. Reprinted (adapted) with permission from [118]. Copyright 2013 ACS.

could explain the relatively low signal enhancement obtained on MOFs. More recently, Kobayashi *et al.* performed ^{195}Pt NMR of Pt(II) centers coordinated by the MOFs linker in UiO-66-NH$_2$. The challenge here laid in (*i*) the low concentration of Pt(II) due to its dispersion in the MOF, and (*ii*) the extreme broadening of ^{195}Pt signal due to its large CSA. BRAIN-CP/WURST-CPMG (broadband adiabatic inversion - CP / wideband, uniform rate, and smooth truncation - CPMG) combined with DNP sensitivity gain allowed them to obtain the static ^{195}Pt NMR spectrum represented in FIGURE 2.24 with an enhancement $\varepsilon_{\mathrm{Pt}}$ of 6. An enhancement of 30 was obtained by mixing the MOF with dielectric particles (NaCl).[123, 102] In 2013, Blanc *et al.* reported the analysis through MAS DNP of so-called mesoporous organic polymers (MOPs), amorphous 3D porous polymers. MAS DNP allowed ^{15}N and ^{13}C CPMAS spectra to be recorded in natural isotopic abundance. Analogously to MOFs, the authors related the quite low signal enhancement to radicals that are maintained outside the material due to the small average pore size of MOPs.[74]

Zeolites were also investigated in the DNP SENS approach. In 2014, $\{^{1}\mathrm{H}\}$-^{119}Sn DNP SENS CPMAS and CP magic angle turning (CP-MAT) DNP SENS combined with computational chemistry and Mössbauer spectroscopy revealed the presence of Sn(IV) active sites in the investigated Sn-β zeolite.[124]

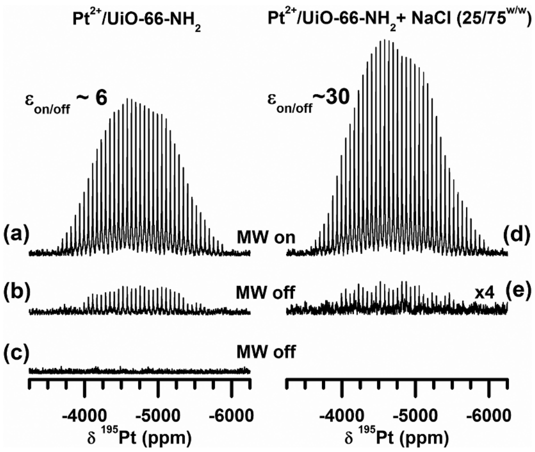

FIGURE 2.24: DNP-enhanced $^{195}Pt\{^{1}H\}$ BRAIN-CP/WURST-CPMG spectra of Pt^{2+}/UiO-66-NH_2 **(a,b)** and the Pt^{2+}/UiO-66-NH_2/NaCl (25/75 w/w) mixture **(d,e)** with **(a,d)** and without **(b,e)** microwave irradiation. Spectrum **(c)** of Pt^{2+}/UiO-66-NH_2 was acquired using direct excitation by WURST-CPMG without microwave irradiation. Reprinted with permission from [123]. Copyright 2016 ACS.

Characterization of materials with low surface area and increasingly diluted species with DNP SENS

The exploration of materials has not been limited to porous materials with relatively high surface areas. Most recent developments in MAS DNP have revealed important structural aspects of materials exhibiting lower and lower surface areas, and on very diluted surface species where the sensitivity issue is strongly emphasized.

In reference [125], DNP SENS allowed getting insights in the adsorption of sucrose on low surface area Ca_3SiO_5 particles and revealed the consequences of this adsorption on the hydration properties of the particles.

Nanoparticles (NPs) also lead to low surface area but have attracted important attention due to their vast potential. DNP enhanced NMR would be a method of choice to study these insensitive systems. In [126], it is shown that DNP SENS experiments can be carried out on NPs. The authors reported the analysis of oleate-capped 4 nm CdSe quantum dots (QDs). They observed that DNP SENS on these QDs cannot be directly performed on a solution containing the suspended QDs and the dissolved polarizing agents, as freezing the sample at 100 K results in the aggregation of the QDs. Thus, the particles were dispersed in mesoporous SiO_2 to prevent aggregation. A ^{13}C-^{111}Cd dipolar HMQC spectrum reported in FIGURE 2.25, allowed to directly observe the interactions between the oleate ligand and the QDs surface. Note that a combination of ^{13}C isotopic labeling and DNP MAS was required to obtain sufficient sensitivity for the 2D experiments. Pruski and co-workers also reported results on NPs using DNP SENS, and they were able to elucidate the degradation of methionine on Pd NPs supported on γ-Al_2O_3.[127]

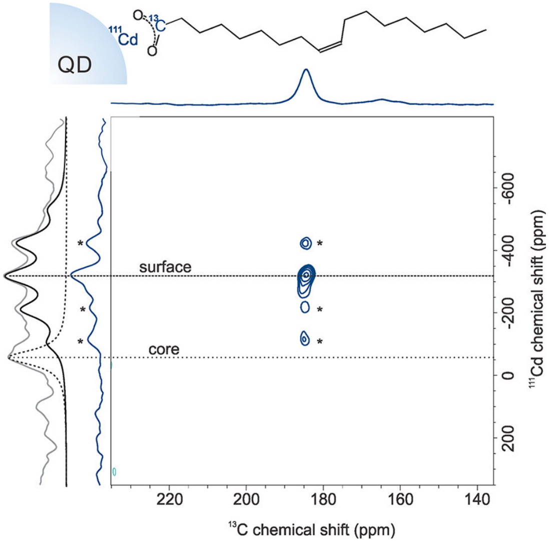

FIGURE 2.25: DNP enhanced Dipolar-HMQC spectrum correlating ^{13}C-1-oleate ligands and ^{111}Cd of CdSe. The dark blue curves are the projections of the two axes. The light grey curve is a ^{111}Cd CPMAS spectrum. The solid black line shows the isotropic signal ^{111}Cd for the surface and the dashed black line shows the ^{111}Cd signal of the core. First order rotary resonance recoupling (R3) was employed. Reprinted with permission from [126]. Copyright 2015 ACS.

Combining isotopic labelling and DNP SENS provided insights in metathesis reaction intermediates TBP (trigonal bipyramidal geometry) and SP (square pyramidal geometrie) metallacyclobutane (structures are represented in FIGURE 2.26**(a)**) on a tungsten metathesis catalyst immobilized on $SiO_{2-(700)}$ particles. Quantitative measurements of C_α-C_β were performed with 1D ^{13}C-^{13}C POSTC7 experiments and found to match with DFT calculations. Interestingly, the authors determined the formation of metallacyclopentane when an important excess of ethylene is used (see the refocused INADEQUATE spectrum reported in FIGURE 2.26**(b)**), thus gaining insights in the deactivation process of the catalyst.[128]

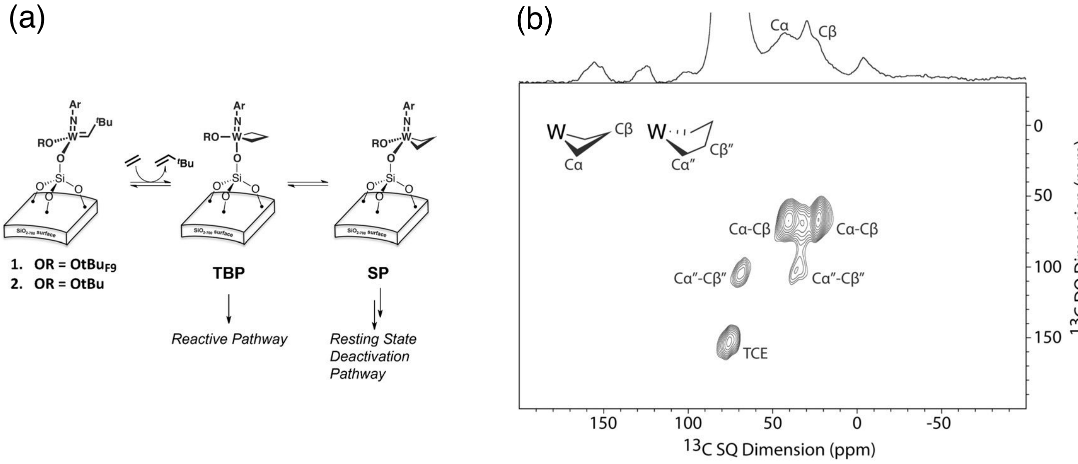
(a)
Ar
N
tBu
RO
W
O
Si
O
SiO2-700 surface
1. OR = OtBuF9
2. OR = OtBu
tBu
TBP
SP
Reactive Pathway
Resting State
Deactivation
Pathway
(b)
Cα
Cβ
W
Cα
Cβ
W
Cα″
Cβ″
Cα-Cβ
Cα-Cβ
Cα″-Cβ″
Cα″-Cβ″
TCE
150
100
50
0
-50
13C SQ Dimension (ppm)
0
50
100
150
13C DQ Dimension (ppm)

FIGURE 2.26: **(a)** Structure of tungsten metathesis catalyst immobilized on $SiO_{2-(700)}$ particles and its metathesis reaction intermediates TBP and SP metallacyclobutane. **(b)** Refocused ^{13}C-^{13}C INADEQUATE obtained by reacting **2** with large excess of ^{13}C-ethylene yielding **SP-2** and hypothesized metallacyclopentane. Reprinted with permission from [128]. Copyright 2016 Wiley-VCH.

MAS DNP for the observation of insensitive nuclei

In NMR on materials, there is a high interest to not be limited to spin-1/2 only, and relatively sensitive nuclei such as ^{1}H, ^{13}C, or ^{15}N because of the different wealth of elements in use in material science.

Oxygen, for instance, is found in many materials. ^{17}O is the only NMR active isotope of oxygen, but it has a very low natural abundance (≈ 0.04 %) and complex spectra due to quadrupolar broadenings. Its low sensitivity makes it an ideal candidate for DNP enhanced NMR. The ability to perform DNP enhanced ^{1}H-^{17}O CPMAS NMR was demonstrated on $H_2{}^{17}O$ with indirect DNP (DNP transfer from electron to ^{1}H and then hyperpolarization is CP to ^{17}O),[129] and then at natural abundance with both indirect and direct DNP (direct DNP transfer from electrons to ^{17}O).[130] The implementation of more sophisticated transfer schemes allowed Perras *et al.* to measure one bond O-H distances with natural ^{17}O isotopic abundance.[131] This was enabled with PRESTO-QCPMG (phase-shifted recoupling effects a smooth transfer of order - quadrupolar CPMG), see Figure 2.27**(a)**, and variation of τ_0 and τ_1 to get the transfer intensity curves (see Figure 2.27**(b)**) which was fitted to obtain distances. Using a similar approach, the same group also probed surface hydrogen bonding structural and dynamical features on mesoporous silica NPs and aluminosilicates.[132, 133] In [73] the first surface-sensitive ^{17}O MAS DNP NMR experiments on CeO_2 were performed. The authors observed that low efficiency for ^{1}H-^{17}O CP attributed to (*i*) the difficulty to spin-lock ^{17}O and (*ii*) the low affinity of TCE for NPs lead to a potentially long distance between ^{1}H of the solvent and ^{17}O and hence prevented efficient CP. They investigated direct DNP and found that they selectively hyperpolarized the first three layers of CeO_2 NPs isotopically enriched in ^{17}O.

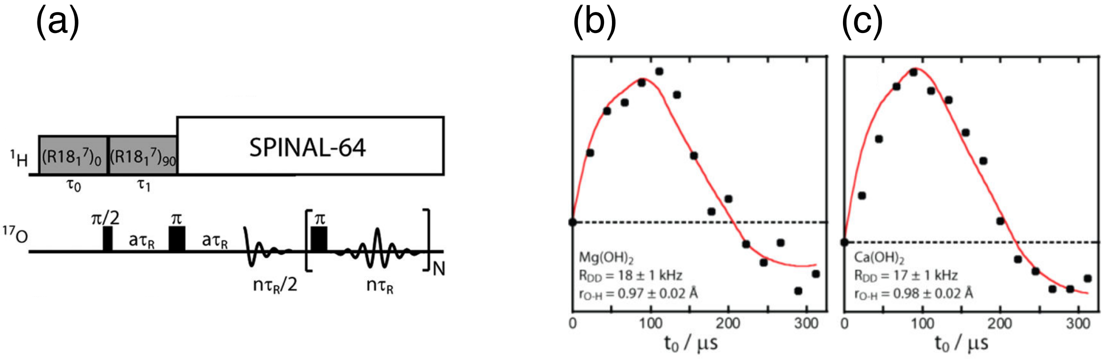

Figure 2.27: **(a)** PRESTO-QCPMG pulse scheme. O-H distance measurements using PRESTO-QCPMG on $Mg(OH)_2$ **(b)** and $Ca(OH)_2$ **(c)** at natural ^{17}O isotopic abundance. Reprinted (adapted) with permission from [131]. Copyright 2015 ACS.

Other examples of MAS DNP NMR applied to insensitive nuclei are ^{89}Y, demonstrated on hydrated yttrium-doped barium zirconates,[134] and ^{43}Ca on nanocrystalline apatites.[135]

Radical sensitive materials

All the previous examples demonstrated that MAS DNP is a very promising method for the characterization of a large variety of materials, in particular for the description of surfaces. However, these approaches can only be applied on materials that are compatible with the radicals. MAS DNP fails when the polarizing agent reacts with the surface-active sites. For example, in reference [119], DNP SENS could not be applied successfully due to the reaction between the polarizing agent TOTAPOL and the ruthenium active center.

Currently, two strategies have been proposed to avoid the degradation of both the polarizing agent and the active sites. A first strategy is to study confined active sites in porous materials the pore of which are small enough to avoid the penetration of the radical, as demonstrated in 2017 by Pump *et al.*[136] An alternative strategy, maybe more versatile, consists in designing polarizing agents in which the free radical center is protected from the material by bulky organic groups. For example, in [137], the use of dendrimer-derivatives of frequently used DNP polarizing agents (see the structure of PyPolB-D2[G3] on FIGURE 2.28) was proposed, where the nitroxide is protected by bulky organosilicon moieties. With this approach, the authors recorded ^{13}C CPMAS DNP SENS spectrum with an organo-tungsten complex immobilized onto $SiO_{2-(700)}$ particles with a DNP enhancement of about 10, whereas no enhancement was obtained by impregnation of the material with a TEKPOL solution in TCE.

2.5 Conclusions

To optimize heterogeneous catalysts in an industrial chemical context, one needs to elucidate the link between structure and properties. However, this is never easy in heterogeneous catalysis as there is a lack of appropriate analytical methods to characterize active sites at an atomic level. Single well-defined catalytic centers immobilized on surfaces, from SOMC or SHC, is a *chemical* answer to this problematic. The idea is that one can benefit from the help of the – well-established – principles of organometallic chemistry to design heterogeneous catalysts. Among all the supports that can be used to immobilize the catalytic center, silica has been presented in more detail as it is one of the most widespread supports. The introduction of single well-defined supported catalysts

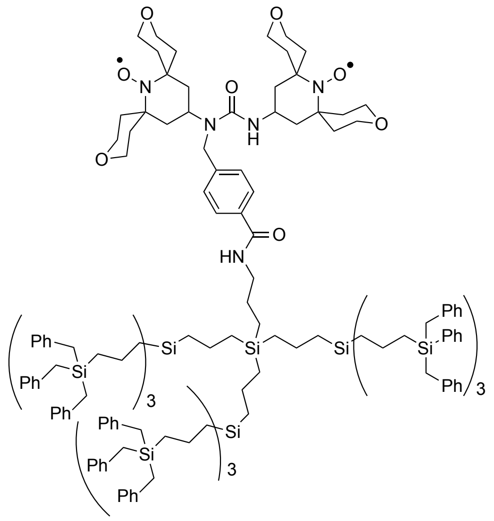

Figure 2.28: Structure of PyPolB-D2[G3]. Adapted from [137]

is not enough to address the problem of structure-properties relationship of the active center. Thus there is still a need for analytical methods to assess the structure of supported species. SSNMR is an excellent candidate to characterize such materials. Some examples where SSNMR has been successfully used to describe single well-defined surface sites have been reviewed. However, the use of isotopic labeling is almost inevitable due to the poor sensitivity of SSNMR. DNP SENS is a hyperpolarization approach that can circumvent this obstacle. The latest development in the DNP MAS field and recent examples where this approach has been used to characterize supported surface sites have been described. All in all, well-defined immobilized catalysts obtained from chemical approaches such as SOMC or SHC combined with DNP SENS can address the need of obtaining optimized heterogeneous catalysts.

Part I

Expanding the experimental range of Dynamic Nuclear Polarization for surfaces

Chapter 3

Experimental aspects of impregnation in DNP SENS of porous silica materials

3.1 Introduction

The first example of Dynamic Nuclear Polarization Surface Enhanced NMR Spectroscopy (DNP SENS) has been carried out in 2010 by Lesage *et al.* [71]. Since then the development of the approach has been focused on improving the sensitivity gain provided by DNP on NMR studies of materials, exploring more and more challenging systems, for example, applying the approach to water-sensitive materials,[92] to radical-sensitive material,[136, 137] or to increasing low surface area materials[125] as it has been reported in the chapter 2 of this manuscript.

During my Ph.D. work, I focus on the characterization of well-defined organometallic catalysts supported on the mesoporous silica SBA-15 by DNP SENS. The latter is a class of silica material consisting of amorphous silica with a dense hexagonal network of cylindrical pores whose diameter usually ranges from 5 to 30 nm [18] as represented in FIGURE 3.1. Different kinds of functionalities can be introduced by covalent binding molecules on the silica surface. Surface functionalization is enabled for example via post-modification of the SBA-15 surface or via a sol-gel approach as described in chapter 2. Nowadays advanced synthetic methods allow to introduce increasingly complex active centers, but also allow to ensure a homogenous distribution of the functionalities, to control the surface concentration of these functionalities, and to tune the hydrophobicity of the surface.

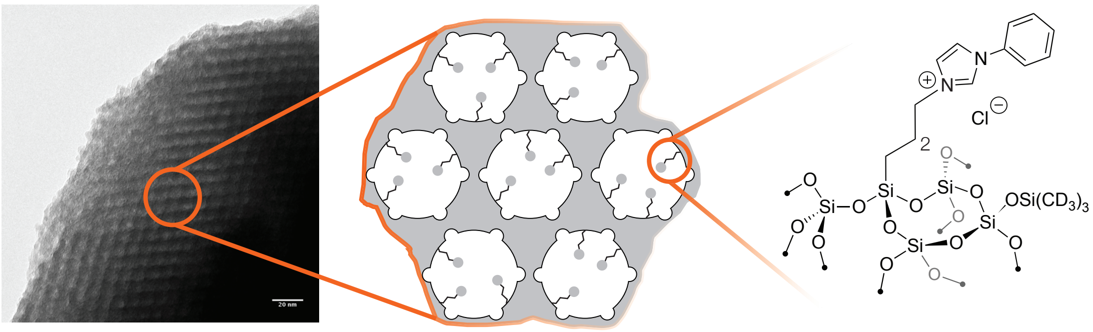

FIGURE 3.1: Functionalized mesoporous silica SBA-15.

As many of materials studied in this thesis are supported on silica, some fundamental experimental aspect of DNP SENS on mesoporous silica are investigated in a first step. Sample preparation in NMR enhanced with DNP is one of the most important factors to guarantee the success of the experience. Without being exhaustive, some important experimental aspects are described here. Experiments reported here are carried out on functionalized SBA-15 silica type material. The conclusions obtained here are mainly linked to general properties of the porous silica matrix rather than to the grafted functionality itself.

In a DNP enhanced NMR experiment, the diamagnetic sample must first be doped with a polarizing agent, which is commonly achieved by impregnating the sample with a radical solution leading to trivial questions. The design of the radical used for CE DNP has resulted in bigger and bulkier polarizing agents as described in the section 2.4.2. Thus when impregnating a porous material with a radical solution, there is a possibility that the pore size prevents the penetration of the radical inside the porous network. This is the case for small pores (pore sizes of approx. 1 nm such as for SBA-16 or MOFs)[122, 19]. However, the answer is not straightforward for SBA-15 silica type where the pore diameter usually ranges from 5 to 30 nm [18] and usually around 5 to 7 nm for the SBA-15 samples studied in the present work. I, therefore, investigate the diffusion into the pores of different polarizing agents from the bTbK family (bTbK, bCTbK, TEKPOL, and TEKPOL2)[100, 101]. To do so, a spin diffusion model in porous materials is developed. It reveals that spin diffusion plays a significant role in DNP SENS experiments applied to SBA-15 and that these models can be used to obtain insights on the location of polarizing agents in the material. These aspects have a substantial impact on the DNP SENS experiment. Indeed, the results show that biggest radicals such as TEKPOL or TEKPOL2 are not able to diffuse inside the porous network of SBA-15 silica.

When impregnating material, another fundamental question that can arise is the influence of the solvent volume for a given weight of porous silica. Hence, the dependence of ratio between the volume of radical solution and the weight of the porous SBA-15 materials on the DNP SENS experiment is investigated. The results reveal the pore-filling mechanisms of the solvent inside the porous network. Regarding the impact on the DNP SENS experiment, it shows that the radical solution volume used to impregnate porous materials should be carefully monitored to ensure the highest possible DNP sensitivity gain.

3.2 Diffusion of the polarizing agent into mesoporous materials

In all this section, the impregnation of an SBA-15 silica material functionalized with phenylimadazolium is investigated, the material is represented in FIGURE 3.1. The silica is impregnated with four different solutions containing 16 mM of bTbK, bCTbK, TEKPOL, or TEKPOL2 in 1,1,2,2-tetrachloroethane (FIGURE 3.2 for the radical structures). The surface of the studied silica is passivated with deuterated trimethylsilyl group (TMS-d_9), and consequently, the surface is hydrophobic. One can expect different behaviors of the DNP enhancements as the size of the radical increases and the decoration of the binitroxides is importantly modified. To probe the distribution of the polarizing agent into the porous silica, the measurement of the quenching introduced by the paramagnetic species in the sample is evaluated. We finally show that we can use ^{1}H-^{1}H spin diffusion models to localize the polarizing agent.

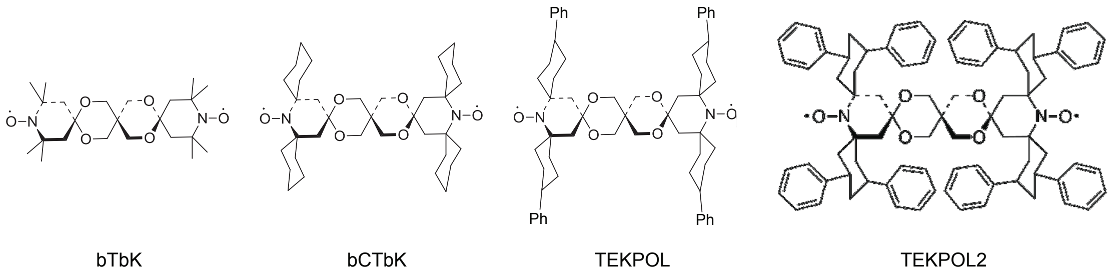

FIGURE 3.2: Radicals from the bTbK series [100, 101]

3.2.1 Signal quenching induced on surface nuclei when introducing nitroxides into porous silica

When a paramagnetic species is introduced into a sample, the NMR signal is partially reduced. This is due to the fact that the nuclear spins undergo strong paramagnetic interactions because of the hyperfine coupling between nuclear and electron spins. This usually results in large anisotropic shifts, or in enhanced relaxation, and partial quenching of the nuclear polarization. In addition, binitroxide radicals, optimized to perform cross-effect DNP, induce important depolarization effect due to the rotation of the sam-

Polarizing agent	**Contribution factor θ**
TEKPOL2	0.83
TEKPOL	0.80
bCTbK	0.18
bTbK	0.23

TABLE 3.1: Contribution factor θ of passivated phenylimadazolium SBA-15 impregnated with different radical solutions in 1,1,2,2-tetrachloroethane.

ple around the magic angle. [111, 110] In this section, the mechanism responsible for the loss of NMR signal upon introduction of paramagnetic species is not essential, however it is important to note that these effects are local and thus the loss of signal only occurs in the direct environnement of the radical.

We measure the *contribution factor θ* as defined in reference [60]. The contribution factor indicates the fraction of the sample, impregnated with the radical solution, that contributes to the NMR signal compared to a sample where materials are impregnated with a pure solvent. It accounts for all the effects described previously, *i.e.* signal quenching and nuclear depolarization. To quantify the fraction of the surface that contributes, ^{29}Si $Q_{4,4'}$ signals can be used as a probe for surface contribution. θ is obtained by dividing the ^{29}Si $Q_{4,4'}$ signal area per unit of mass of the impregnated material with a radical solution by the area of the same peak with a material impregnated with pure solvent. The contribution factor for different radical solutions are reported in TABLE 3.1.

We observe that the contribution factor is significantly lower for small polarizing radicals, bCTbK, and bTbK whereas it reaches 83 % for TEKPOL2 and 80 % for TEKPOL. These observations suggest that bigger radicals cannot enter into the silica pores and consequently less signal from the surface is quenched as radicals remain outside. With smaller radicals such as bCTbK, bTbK, on the contrary, a smaller contribution factor reveals higher concentration of radicals in the pore resulting in more quenching of the surface signals. Note that the quenching factor itself is not sufficient to get a formal proof that TEKPOL and TEKPOL2 do not enter in the SBA-15 pores whereas bTbK and bCTbK do enter. Indeed, as stated before, the aromatic rings decorating the radicals may change significantly the interactions between the surface and the radicals. Thus, in the following section, localization of the polarizing agent in porous materials is confirmed by investigating the spin diffusion of the enhanced magnetization inside the pores.

3.2.2 Spin diffusion simulations

In DNP experiments in the solid-state, ^{1}H-^{1}H spin diffusion is a very important aspect. This is a flip-flop process that efficiently diffuses the ^{1}H hyperpolarization locally created by DNP around each radical through the sample. Thus spin diffusion allows obtaining enhanced NMR signals from sample regions which are not directly polarized. Actually, ^{1}H-^{1}H spin diffusion is essential in DNP experiments as the signals in the direct neighborhood of the radical are quenched and then not observed[60, 99].

In 2007, Van Der Wel *et al.* have shown that it is possible to polarize amyloidogenic peptide nanocrystals in a TOTAPOL solution from the outside of the core of the crystal. [68] In addition, they have observed that the DNP enhancement is not constant with the recycling time of the experiment and that the enhancement as a function of time can be modeled by using the Fick's law, which can be applied for processes of nuclear polarization and spin diffusion. In 2013, Rossini *et al.* have polarized 1-100 μm glucose crystals and have applied a numerical spin diffusion model to obtain an estimation of the size of the glucose crystal in the powder by fitting the DNP enhancement as a function of time. [60] FIGURE 3.3 is a reproduction of the enhancement as function of the polarization time observed on glucose in [60]. They have observed that the enhancement starts at its maximum and slowly decreases to reach a steady-state value. The latter decreases with increasing size of particles.

Here, I show how spin diffusion models allows to get insights into the location of the polarizing agent location in SBA-15 and also enables the measurement of pore lengths with DNP SENS. I first adapt the spin diffusion model developed by Rossini *et al.* to interpret the behavior of DNP enhancement in SBA-15. [1]

To probe the heterogeneity of the radical distribution in mesoporous silica, the ^{1}H en-

---

[1] A unified spin diffusion model for different set of data with different geometries (including porous silica) has been developed and submitted: Pinon, A ; Schlagnitweit, J ; Berruyer, P ; Rossini, A ; Lelli, M ; Socie, E ; Tang, M ; Pham, T ; Lesage, A ; Schantz, S ; Emsley, L. Measuring Nano to Micro Structures From Relayed DNP NMR.

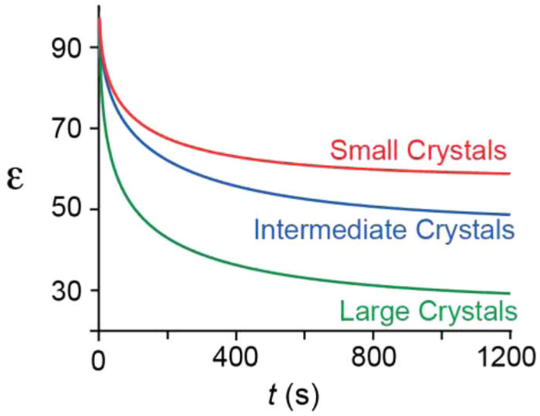

FIGURE 3.3: ^{1}H enhancement as a function of time simulated for a microcrystalline system. Reproduced with permission from [60]. Copyright 2012 American Chemical Society.

hancements as a function of time are recorded on the functionalized SBA-15 material impregnated with four different solutions containing 16 mM of bTbK, bCTbK, TEKPOL, or TEKPOL2 in 1,1,2,2-tetrachloroethane. The enhancement curves obtained are reported on FIGURE 3.4. As observed for the contribution factor discussed above, the enhancements as a function of time obtained with SBA-15 impregnated with TEKPOL and TEKPOL2 show a clearly different behavior compared to bTbK and bCTbK. We observe for the two bulkier radicals, that the ^{1}H enhancement starts to increase at short polarization times, reaches a maximum and finally decreases to its steady-state value. However, for bTbK and bCTbK, the enhancement quickly decreases and reaches its final value within approximately 10 seconds.

Spin diffusion model for relayed DNP in porous materials

To rationalize these behaviors, the spin diffusion model used in 2012 by Rossini *et al.* [60] needs to be modified as the enhancements measured on mesoporous silica impregnated with TEKPOL or TEKPOL2 solutions in TCE have never been observed or predicted with this model.

At the mesoscopic scale, spin diffusion can be described using the Fick's second law:

$$\frac{\partial P}{\partial t} = \nabla(D\nabla P) + \sigma(\vec{r}, t) \tag{3.1}$$

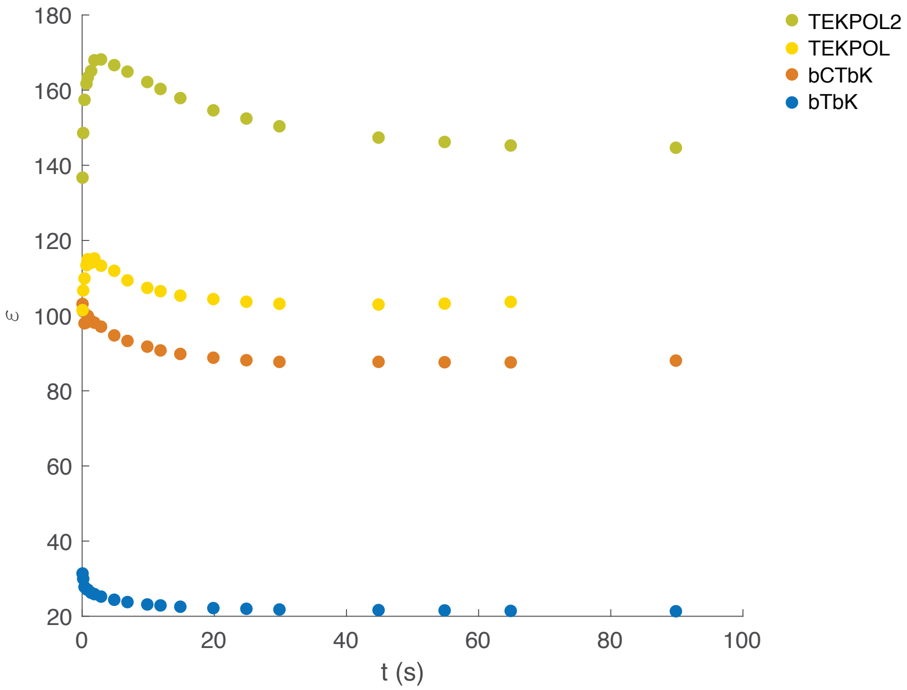

FIGURE 3.4: ^{1}H enhancement as a function of time recorded on a functionnalized SBA-15 material impregnated with four different solutions containing 16 mM of bTbK, bCTbK, TEKPOL, or TEKPOL2 in 1,1,2,2-tetrachloroethane.

where

- $P(\vec{r},t) = \frac{n_\alpha(\vec{r},t)-n_\beta(\vec{r},t)}{n^0_\alpha(\vec{r},t)-n^0_\beta(\vec{r},t)}$ is the local nuclear polarisation. At thermal equilibrium, $P = P^0 = 1$; at nuclear saturation, $P = 0$.

- $\sigma(\vec{r},t)$ is the local *creation* term of Fick's law. In the spin diffusion process, polarization is created, after saturation, following spin-lattice relaxation process. Thus, this term can be written $\sigma(\vec{r},t) = \frac{P(\vec{r},t)-P^0(\vec{r})}{T_1(\vec{r})}$. Note that if we assume no diffusion ($D = 0$) and homogenous spin-lattice relaxation time ($T_1(\vec{r}) = T_1$), we are back to a simple exponential build-up of polarization after saturation.

SBA-15 is a porous silica exhibiting a dense hexagonal network of pores. It is modeled with a single cylindrical tube aligned on the x axis, filled with the polarizing agent solution. As the system is invariant by all rotations around the x-axis and assuming that the polarization is independent of the distance r to the center of the pore (constant polarization in slices at $x = constant$), it can be reduced to a one dimensional problem: $P(\vec{r}, t) = P(x, t)$. Finally, assuming the diffusion coefficient D can only depend on x, the diffusion equation can be written:

$$\frac{\partial P}{\partial t} = D\frac{\partial^2 P}{\partial x^2} + \frac{P(x,t) - P^0(x)}{T_1(x)} \tag{3.2}$$

We first need to set initial and boundary conditions for the partial differential equation.

- **Initial conditions.** The enhancement as a function of time is recorded with a saturation-recovery experiment. At time $t = 0$ the nuclear polarization is equal to zero in the whole sample:

$$\forall x \;\; P(x, t = 0) = 0 \tag{3.3}$$

- **Boundary conditions.** The system we considered is closed from the outside, *i.e.* no polarization can enter, nor leave the system through the border. Thus the polarization flow $\vec{j_P}(x,t)$ at $x = 0$ and $x = L$ can be set to zero at all times:

$$\begin{aligned} & \forall t \;\; \vec{j_P}(x = 0, t) = \vec{j_P}(x = L, t) = 0 \\ \Leftrightarrow \;\; & \forall t \;\; -D\vec{\nabla}P(x = 0, t) = -D\vec{\nabla}P(x = L, t) = 0 \\ \Leftrightarrow \;\; & \forall t \;\; \tfrac{\partial P}{\partial x}(x = 0, t) = \tfrac{\partial P}{\partial x}(x = L, t) = 0 \end{aligned} \tag{3.4}$$

In the porous system, we now need to take into account the distribution of the polarizing agent into the system by properly defining the functions $x \to T_1(x)$ and $x \to P^0(x)$. The functions are represented in FIGURE 3.5. The cylindrical tube of total length L is divided in two: the source, where the DNP hyperpolarization is created and, the target where the DNP hyperpolarization is transported by spin diffusion. The source is located at both edge of the silica pore on a width P_L, simulating partial diffusion of the polarizing agent into the pore. Due to direct paramagnetic relaxation enhancement (PRE) effect, [138] we consider a shorter T_1^{source} in the region where the radical is located and a longer one T_1^{target} in the region where there is only pure TCE. A continuous T_1 function is created using the hyperbolic tangent (tanh):

$$T_1(x) = T_1^{source} + \frac{T_1^{target} - T_1^{source}}{2}\left(\tanh p(x - P_L) + \tanh p(L - x - P_L)\right) \tag{3.5}$$

where p defines the *slope* of the hyperbolic tangent and consequently the thickness of the interface between solvent containing polarizing agent and pure TCE.

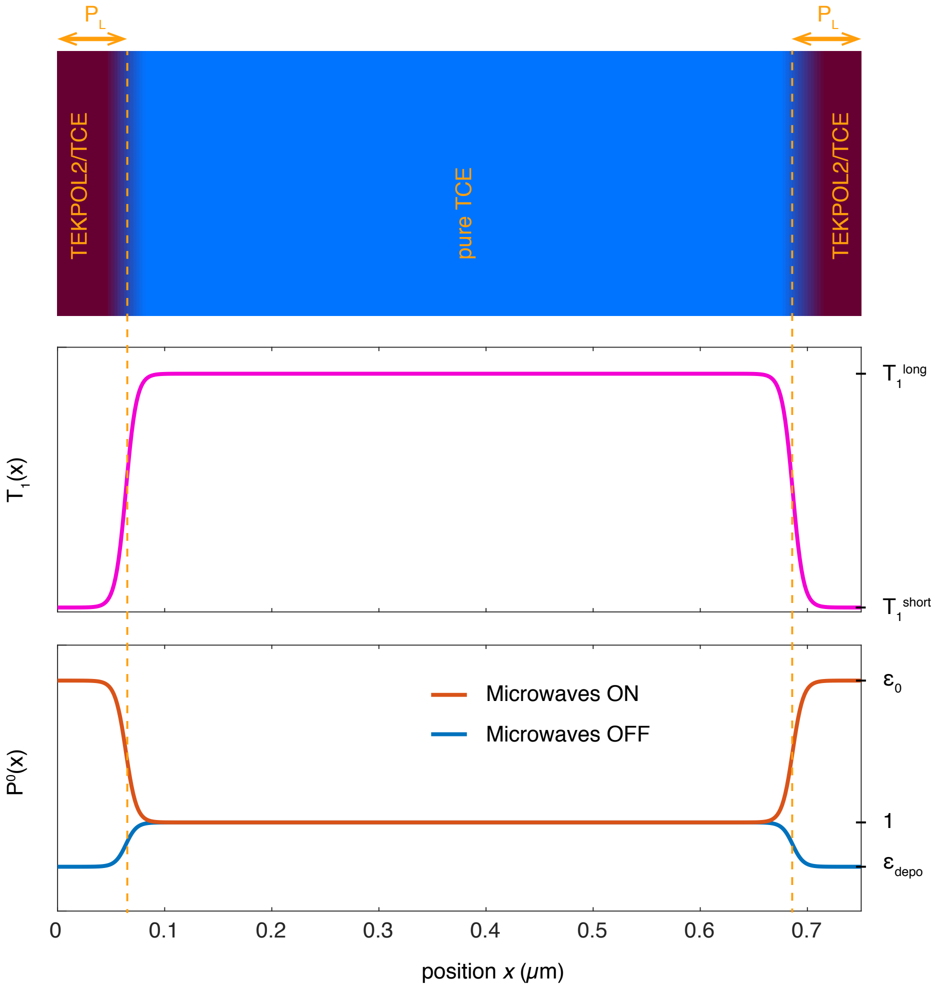
P_L
P_L
TEKPOL2/TCE
pure TCE
TEKPOL2/TCE
T_1(x)
T_1^long
T_1^short
P^0(x)
Microwaves ON
Microwaves OFF
ε_0
1
ε_depo
0
0.1
0.2
0.3
0.4
0.5
0.6
0.7
position x (μm)

FIGURE 3.5: Schematic representation of the system used for simulations with the T_1 and P_0 functions as defined in the main text. Radicals are located at the edges of the system (purple regions), the center of the pore only contains pure TCE (blue region) and the different regions are *continuously connected.*

The local equilibrium polarization function P^0 has two definitions depending on if there is microwaves irradiation of the sample or not. If microwaves are on, the region where the radicals are located $[0, P_L] \cup [L - P_L, L]$, P^0 is set to ε_0 translating that this region is directly hyperpolarized by DNP. In the region containing pure TCE $[P_L, L-P_L]$, P^0 is given by the Boltzmann distribution and set to 1 when microwaves on or off. In the absence of microwaves in the source region, the effect of depolarization induced by binitroxides is taken into account. P^0 is set to $\varepsilon_{depo} = 0.5$ where the value of ε_{depo} is chosen to be in line with litterature. [109, 110, 111] The continuous function P^0 is created again with the use of the hyperbolic tangent:

$$P^0(x) = \begin{cases} \varepsilon_0 + \frac{1-\varepsilon_0}{2} \left(\tanh p(x - P_L) + \tanh p(L - x - P_L)\right) \\ \hfill \text{if microwaves are on} \\ \varepsilon_{depo} + \frac{1-\varepsilon_{depo}}{2} \left(\tanh p(x - P_L) + \tanh p(L - x - P_L)\right) \\ \hfill \text{if microwaves are off} \end{cases} \tag{3.6}$$

The partial differential equation is solved numerically in MatLab to get the polarization in the system as function of space and time $(x, t) \to P(x, t)$. Finally, the NMR signals intensity is obtained by integrating the polarization all over the sample and the enhancement by dividing simulated polarization build-up with and without microwaves:

$$\mathcal{S}(t) = \int_0^L P(x, t)\theta(x)\mathrm{d}x \qquad \text{and} \qquad \varepsilon(t) = \frac{\mathcal{S}_{on}(t)}{\mathcal{S}_{off}(t)} \tag{3.7}$$

where θ is a function that accounts for partial quenching of NMR signals due to presence of radicals. As in the systems considered in this section the distribution of radical is expected to be heteregenous, θ is not supposed to be constant along the pore and can varies between 0 (total quenching) and 1 (total contribution). To be consistent with the previous definition the contribution function θ is also defined with the hyperbolic tangent function:

$$\theta(x) = \theta_{min} + \frac{\theta_{max} - \theta_{min}}{2} \left(\tanh p(x - P_Q) + \tanh p(L - x - P_Q)\right) \tag{3.8}$$

Note that here defining such a contribution function assumes that there are regions in the sample where we can observe ^{1}H spin diffusion but the signal is not directly observed in such regions. This is possible if paramagnetic interactions between nitroxide radicals and ^{1}H have a strong effect on nuclear coherence lifetimes, but little effect on the spread of the signals (^{1}H signals still overlaps, allowing conservative flip-flop processes).

Spin diffusion in mesoporous silica impregnated with TEKPOL2 in TCE

In the case of mesoporous silica impregnated with a 16 mM TEKPOL2 solution in TCE, in section 3.2.1 a very high contribution factor of 83 % (measured on the silicon surface signals) have been reported. High contribution factor suggests that the radicals

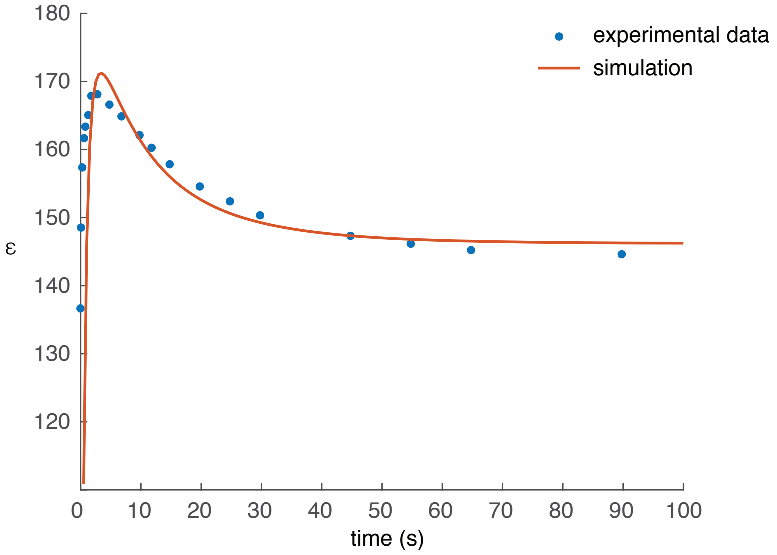

Figure 3.6: ^{1}H enhancement as a function of time recorded on functionnalized SBA-15 material impregnated with 16 mM TEKPOL2 in TCE: comparison between the experimental data and the curve obtained with spin diffusion model.

cannot diffuse through the entire pore of the mesoporous silica, TEKPOL2 molecules may, however, diffuse into the entrance of the pore up to a certain length and then block the entrance for other TEKPOL2 molecules. This results in a pore filled with pure TCE at the center and TEKPOL2/TCE at the outside and the pore entrance, as illustrated on Figure 3.5. This segregation should result in a rather high concentration of TEKPOL2 at the pore entrance. Thus, we hypothesize that the ^{1}H signals in the regions where the radicals are highly concentrated are fully quenched. In addition, we assume that the length in which TEKPOL2 has diffused can be estimated using the contribution factor θ measured on the surface signal (through CP on ^{29}Si).

We simulate spin diffusion in a pore of length L with $P_L = P_Q = (1-0.83)\times L$ defining the size of the regions at the edge of the system where nuclei are directly polarized and the signals quenched. As we assume total quenching in the TEKPOL2/TCE regions and no quenching in the pure TCE region, we have $\theta_{min} = 0$ and $\theta_{max} = 1$. Finally we take $T_1^{source} = 0.5$ s and $T_1^{target} = 27$ s. The pore length L is adjusted during the numerical simulations to get the best fit of the experimental data. We obtain a pore length of $L = 750$ nm, which is in good agreement with the expected length of silica pores in SBA-15 materials, demonstrating the suitability of the model. The experimental data and the simulated data for the enhancement as a function of time are compared in FIGURE 3.6.

Spin diffusion in mesoporous silica impregnated with bCTbK in TCE

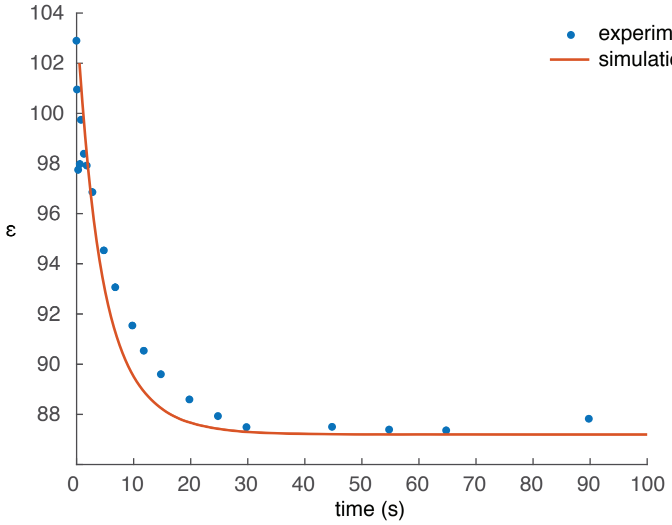

FIGURE 3.7: ^{1}H enhancement as a function of time recorded on functionnalized SBA-15 material impregnated with 16 mM bCTbK in TCE: comparison between the experimental data and the curve obtained with the spin diffusion model.

When mesoporous silica is impregnated with a solution containing 16 mM bCTbK in TCE, the enhancement as a function of time behaves quite differently and the spin diffusion model can be used to simulate this different aspect. The contribution factor measured on the silicon surface signal of only 18 % suggests that the radical can diffuse inside the pores of silica on a longer range, thus resulting in quench of a larger part of the NMR surface signals. Though bCTbK may enter further into the pores, we still observe an enhancement that evolves with time[2] that can only be explained by a heterogenous distribution of the radical. Thus we hypothesize the radical diffuses slowly into the pore resulting in a gradient of concentration along the pore. As the radical is dispersed in a bigger volume, we do not expect a quenching effect on ^{1}H signals as strong as for TEKPOL2 as we interpreted this effect to a high local concentration of TEKPOL2. In reference [99], the quenching measured as a function of the radical concentration has shown that increasing the radicals concentration has resulted in a decrease of the contribution factor. Using a 25 mM bCTbK solution, the authors have observed almost 80 % of the surface signals are quenched. Thus we simulate the enhancement as function of time, with the known pore length of $L = 750$ nm, a contribution function set to $\theta : x \to 1$ and $P_L = P_Q = (1 - 0.18) \times L$, for the ^{1}H enhancement curve measured with the material impregnated with bCTbK dissolved in TCE. Figure 3.7 shows the simulated curve is in reasonable agreement with the experimental data.

---

[2] In a frozen solution of binitroxide in TCE, we observe the enhancement is constant as a function of time. However, we believe spin diffusion also allow polarizing the entire frozen solution, but it happens almost *instantaneously* as the average distance between two polarizing agents is quite small (≈ 2.9 nm in a 16 mM binitroxide solution in TCE).

The enhancements as a function of time for mesoporous silica impregnated with a solution of TEKPOL or bTbK in TCE exhibit similar behaviors as TEKPOL2 and bCTbK respectively. In principle, spin diffusion simulations can be easily adapted to these cases using similar parameters for the simulations.

All in all, the results and simulations report here show that bulkier polarizing agents, TEKPOL and TEKPOL2, are not able to diffuse in the entire length of the pores of SBA-15. On the contrary, smaller radicals investigate in this section, bTbK and bCTbK can enter and diffuse into the SBA-15 porous network. Preventing the diffusion of the radical in the pores allows to obtain high contribution factor from the silica surface and thus, combined with high surface contribution factor θ, the sensitivity of the DNP SENS experiment for functionalized SBA-15 silica type material is significantly high with TEKPOL or TEKPOL2. Using bTbK or bCTbK an important part of the NMR signal is loss due to paramagnetic quenching effects.

3.3 Partial Impregnation Dynamic Nuclear Polarization

Another, basic but important, experimental aspects of DNP SENS on mesoporous materials is the volume of solution used to impregnate the sample. In this section, we analyze the DNP enhancement obtained on passivated mesoporous silica SBA-15 impregnated with different volumes of a 16 mM bCTbK solution in TCE. We choose to work with bCTbK as, according to section 3.2, it diffuses more easily into the porous material, thus simplifying the analysis of the effect of partial impregnation on DNP SENS.

3.3.1 Effect of partial pore filling on DNP SENS experiments

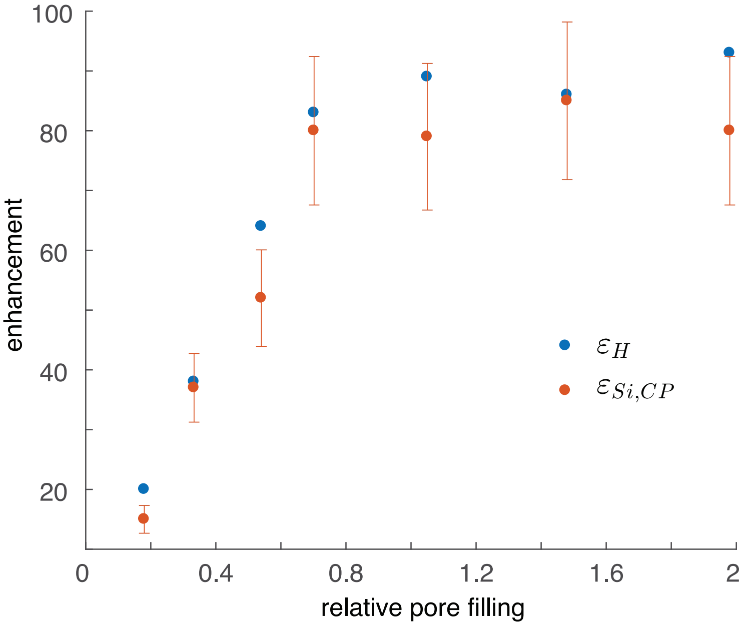

FIGURE 3.8: ^{1}H and ^{29}Si (measured via CP from ^{1}H) enhancements as a function of the pore filling of the passivated functionalized SBA-15 material with a 16 mM bCTbK solution in TCE. Error bars on ^{29}Si were estimated on the basis of the signal over noise ratio in microwaves on and off spectra. Error bars on ^{1}H enhancement are not represented as they were found to be lower than the size of the data points themselves.

FIGURE 3.8 reports the DNP enhancement measured on ^{1}H and on ^{29}Si (through CP) as a function of the solution volume. The latter is measured relative to the pore volume obtained by nitrogen physisorption measurement: 2.05 cm^3.g^{-1} using the Barrett-Joyner-Halenda (BJH) approach [139] and 1.99 cm^3.g^{-1} using the Brunauer-Emmett-Teller (BET) approach.[140] We first observe an increase of both ε_{H} and $\varepsilon_{^{29}\mathrm{Si,\ CP}}$ enhancements up to approximately the complete pore filling of the mesoporous material (relative pore filling of 1). After the complete filling of the pore, when adding more solution to impregnate the material, both ε_{H} and $\varepsilon_{^{29}\mathrm{Si,\ CP}}$ enhancements reach a plateau at their maximum value.

In practice, the visual aspect of the sample clearly indicates if the impregnation volume exceeds or not the porous volume of the sample. While a dry powder is obtained when the impregnation volume is smaller than the porous volume, a wet paste-like sample is obtained when it is larger.

These curves clearly show that partial impregnation of mesoporous material results in lower DNP performance whereas over-impregnation of the sample does not affect the DNP efficiency. However, we note that the absolute sensitivity of the DNP SENS experiments will decrease when overloading the sample, as adding too much solution will decrease the amount of material that can be packed in an NMR rotor.

It is particularly interesting to observe that the shape of the DNP curve evolution clearly change when the volume of the polarizing solution matches the porous volume measured using nitrogen physisorption. Indeed, if nitrogen can adsorb on nearly the entire available silica surface and fills all the pores (including micro-pores) of mesoporous silica SBA-15, this is not necessary the case for TCE. Indeed, the wettability of the silica surface may not be the same, and the ability to access the whole available porous volume may be different from nitrogen. Here the results suggest that the porous volume of the material revealed by DNP using TCE as solvent matches extremely well with the volume measured with nitrogen physisorption. Adsorption measurements with TCE or organic solvents, in general, are possible but not straightforward as this requires a special BET instrument.

Though the porous volume of the material measured with TCE matches with the volume measured by nitrogen adsorption, it does not explain why we observe an increase of the enhancement when the pore filling is incomplete. In 2014, Kubicki *et al.* reported that the introduction of finely ground KBr particles in a 16 mM TEKPOL solution in TCE resulted in almost two times higher DNP enhancements measured in bulk solution.[102] They hypothesized that the high dielectric properties of KBr particles allowed for a better distribution of the microwaves field inside the sample thus increasing the average field experienced by the sample and thus resulting in higher DNP enhancement. This effect is related to the relative dielectric constant of the particles compared to TCE ($\epsilon_r(\text{TCE}) = 2.5$ and $\epsilon_r(\text{KBr}) = 4.9$). Here we believe that we observe a *reverse dielectric effect*. Porous materials are currently attracting attention in microelectronics for their properties of reaching low relative dielectric constants by increasing porosity. The relative dielectric constant decreases when the porosity of the material is increased.[141, 142, 143] In our case, we progressively reduce the *apparent* porosity of the material by filling it with TCE and thus the relative dielectric constant increases. Similarly to what was observed with the addition of high relative dielectric constant particles, filling the pores with TCE increases the apparent dielectric constant and thus yield to higher DNP enhancement.

So far I only discussed the general trend observed for these enhancements as a function of the filling volume. In the following section I show that the results shown in FIGURE 3.8 also give insights into the pore filling mechanisms of TCE in the passivated SBA-15.

3.3.2 Pore filling mechanisms

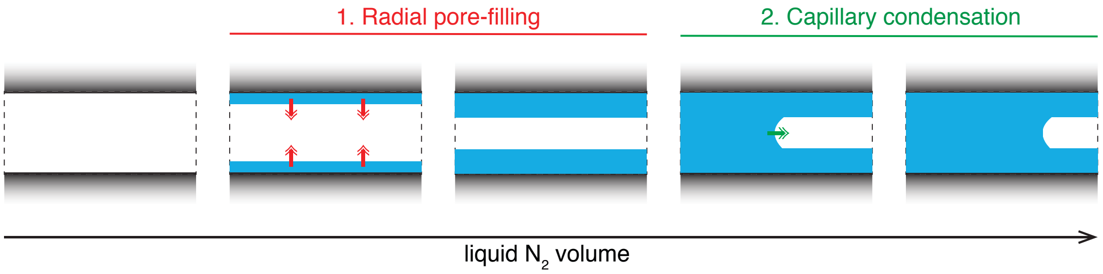

FIGURE 3.9: Pore filling of liquid N_2 in MCM-41 porous material. A pore is schematically represented with different liquid N_2 volume. First, radial pore-filling occurs, then capillary condensation occurs in a second time.

In 2004, Cao *et al.* compared, using a combination of Density Functional Theory (DFT), Grant Canonical Monte Carlo (GCMC) simulations, and experimental adsorption data, the pore-filling mode of N_2 and tetrachloromethane CCl_4 in MCM-41 porous material.[144] They found, in the case of N_2, that the latter started to fill the pores progressively from the wall to the center (radial multi-layer filling), then at some point capillary condensation of N_2 occurred in the remaining space as represented in FIGURE 3.9. Unlike N_2, for CCl_4 they observed that capillary condensation directly occurred in MCM-41 without the completion of a single contact layer of CCl_4. These experiments thus show us that the pore filling with TCE cannot be *a priori* postulated from the knowledge of gas adsorption. Grünberg *et al.* studied in 2004 water confinement in mesoporous silica MCM-41 and SBA-15 using ^{1}H MAS NMR spectroscopy. They found that water filling in SBA-15 occurs in two steps, first with a radial-pore-filling mode and secondly pore condensation at a high level of water content. [145] Later, in 2010, water filling of silica nanopores were analyzed in [146] along with dynamics of confined water.

FIGURE 3.10 shows different simple models that we can imagine for the filling of pores in SBA-15 with the bCTbK solution in TCE. Hypothesis (1) is an axial pore filling model and implies that the filling of pores occurs linearly: for a relative pore filling degree of 0.5, half of each pores is filled with the polarizing agent solution. The second hypothesis (2) is that pores can be only entirely filled or completely empty: for a 0.5 pore filling one out of two pores is filled with solution one out of two pores is entirely empty. Hypothesis (3) is the radial pore filling model where the filling with the solution occurs progressively from the wall of the pores to the center.

Considering the amount of TCE solvent used to impregnate samples and ^{1}H spectra usually obtained in DNP SENS, it seems reasonable to assume ^{1}H spectra (recorded without any solvent suppression techniques [96, 97]) will be dominated by the solvent resonances. If we analyze ^{1}H-^{29}Si HETCOR usually obtained for mesoporous silica under DNP SENS conditions, see FIGURE **??** and also references [72, 99] for example, ^{29}Si nuclei are never directly polarized from the protons of the solvent. However, these ^{29}Si nuclei are always polarized from the covalently attached organic moieties used to functionalize the surface. This is interpreted in terms of ^{1}H spin diffusion, which relays the hyperpolarized magnetization through the solvent where it reaches the ^{1}H of the organic moieties and is transferred to neighboring ^{29}Si nuclei by CP. When the microwaves are off, the $\{^1H\}$-^{29}Si CP spectrum is that of the entire functionalized silica surface is observed. For an indirect DNP (hyperpolarized ^{1}H and CP to ^{29}Si), considering that there is no ^{1}H spin diffusion in the bulk silica when microwaves are on, only surface ^{29}Si in contact with the bCTbK solution can be hyperpolarized. Thus only these ^{29}Si nuclei are participating to the ^{1}H-^{29}Si CP spectrum (we can neglect the contribution of

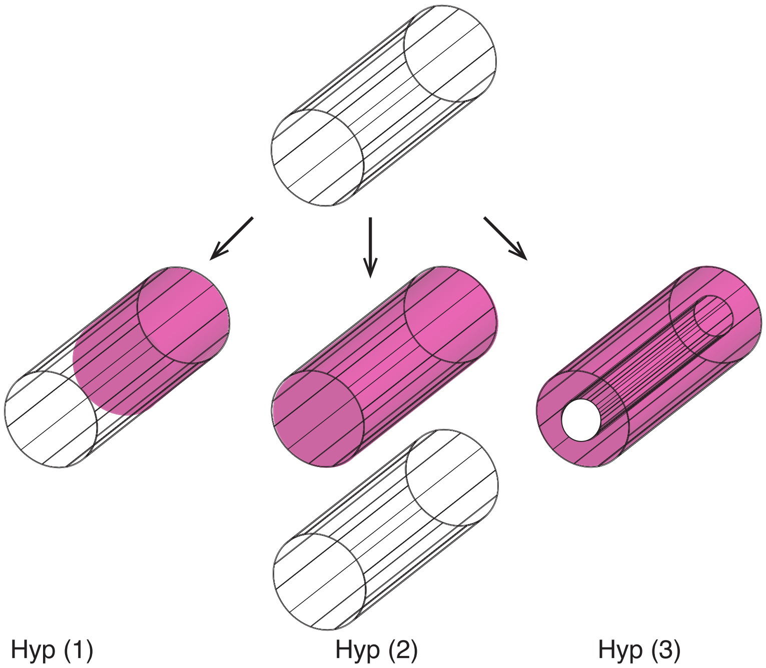

FIGURE 3.10: Pore filling with TCE of passivated SBA-15 hypotheses. (1) is an axial pore filling model ; (2) supposes pores can be only entirely filled or entirely emptied ; (3) is a radial pore filling model.

non-enhanced regions in microwaves on spectra). Consequently, if the entire ^{1}H DNP enhancement is transferred to the ^{29}Si during CP, we expect $\varepsilon_{^{29}\mathrm{Si,\ CP}}$ to match with $\varepsilon_{^1\mathrm{H}}$ for regions where the solution wets the surface. Regions, where the surface is not wetted, will not be enhanced during microwaves on experiments and thus ^{29}Si will be dominated by enhanced regions; but they will still contribute as equally as wetted regions when microwaves are off.

For hypothesis (3), the whole surface is always entirely wetted with the polarizing solution whatever the volume of impregnation is. Thus the entire surface is enhanced and we expect $\varepsilon_{^1\mathrm{H}} = \varepsilon_{^{29}\mathrm{Si,\ CP}}$. On the contrary, for hypothesis (1) and (2), if the volume used to impregnate samples is lower than the porous volume, it will result in partial coverage of the surface. Let's write α the ratio between the wetted surface and the total surface of the sample (in FIGURE 3.10 $\alpha = 0.5$ is represented). As $\{^1\mathrm{H}\}$-^{29}Si CP spectra with microwaves ON are dominated by ^{29}Si signals from the wetted surface, and the whole surface contributes to when microwaves are OFF, we expect a mismatch between $\varepsilon_{^1\mathrm{H}}$ and $\varepsilon_{^{29}\mathrm{Si,\ CP}}$: n_{tot} spins contributed to μw OFF and αn_{tot} to μw ON:

$$\varepsilon_{^{29}\mathrm{Si,\ CP}} = \frac{I_{\mu w\ on}}{I_{\mu w\ off}} = \frac{\alpha\, n_{tot}\, \varepsilon_{^1\mathrm{H}}}{n_{tot}} = \alpha\, \varepsilon_{^1\mathrm{H}} \tag{3.9}$$

FIGURE 3.10 shows that $\varepsilon_{^{29}\mathrm{Si,\ CP}}$ match with $\varepsilon_{^1\mathrm{H}}$ for all relative pore fillings, confirming hypothesis (3) for the pore-filling mechanism of TCE in passivated mesoporous silica. Note that, contrary to the study of Grünberg *et al.* [145] of water filling in SBA-15 where they have observed water condensation of water after radial filling, our enhancement data do not allow us to reveal such precise description of the filling process of TCE inside SBA-15: radial pore filling model or a two-step pore-filling (radial pore filling followed by condensation like in MCM-41, FIGURE 3.9) will both give matching between $\varepsilon_{^1\mathrm{H}}$ and $\varepsilon_{^{29}\mathrm{Si,\ CP}}$.

3.4 Conclusions

In this section, we analyze two different experimental aspects of impregnation in DNP SENS. The conclusions that we have obtained give us a more detailed picture of the impregnation process in porous materials and new insights for sample preparation which is maybe one of the most crucial factors to guarantee the success of a DNP SENS experiment.

The analysis of spin diffusion in functionalized mesoporous silica impregnated with different polarizing agent solutions from the bTbK series allows us to demonstrate that the impregnation leads to a heterogeneous distribution of the polarizing source inside the material. In particular, bulkier radicals (TEKPOL and TEKPOL2) diffuse a short way into the pores whereas smaller ones (bTbK and bCTbK) can diffuse on longer range. The analysis of enhancement behaviors with spin diffusion model require to modify the model previously published for amyloid fibrils [68] and microcrystals [60]. In particular, the role of the quenching appears to be key to reproduce the enhancement curves.

The analysis of the influence of the volume of solvent used to impregnate the porous sample in DNS SENS shows that insufficient impregnation will lead to a significant loss of the DNP efficiency in mesoporous silica. We hypothesize the existence of a reverse dielectric effect that can explain the poor DNP enhancement obtained from partially loaded silica. However, the TCE volume needed to correctly impregnate samples can be simply estimated from the porous volume calculated with BET nitrogen adsorption measurements. We have also seen that impregnation of passivated mesoporous silica with TCE occurs with a radial-pore-filling mode: a TCE layer forms on the silica wall and progressively grows from the surface to the center of the pore.

Using both optimal volume of the polarizing solution and a bulky highly efficient radical like TEKPOL2 that partially diffuse inside the pores as demonstrated in this section, and thus lead to high contribution factors, extremely high overall enhancement can be obtained for mesoporous silica materials. This, in addition, yields long coherence lifetime for the surface nuclei, allowing for the application of efficient solvent suppression techniques as well as, more importantly, of echo-based experiments like INADEQUATE or REDOR-type experiments (as will be detailed in Chapter 6).

Chapter 4

40 kHz Magic Angle Spinning Dynamic Nuclear Polarization

This chapter is an augmented version of the article:
Chaudhari, S. R.; Berruyer, P.; Gajan, D.; Reiter, C.; Engelke, F.; Silverio, D. L.; Copéret, C.; Lelli, M.; Lesage, A.; Emsley, L. *Phys. Chem. Chem. Phys.* **2016**, *18*, 10616-10622.

Chapter 5

Frozen acrylamide gels as DNP matrix

This chapter is an augmented version of the article:
Viger-Gravel, J.†; Berruyer, P.†; Gajan, D; Basset, J.M.; Lesage, A; Tordo, P; Ouari, O; Emsley, L. *Angew. Chem. Int. Ed.*, Accepted article, DOI: 10.1002/anie.201703758
† authors contributed equally

Part II

Three-dimensional surface structure determination

Chapter 6

Direct observation of three-dimensional surface molecular structure

This chapter is an augmented version of the article:
Berruyer, P.; Lelli, M.; Conley, M. P.; Silverio, D. L.; Widdifield, C. M.; Siddiqi, G.; Gajan, D.; Lesage, A.; Copéret, C.; Emsley, L. *J. Am. Chem. Soc.* **2017**, *139*, 849-855.

Chapter 7

Perspectives: exploring low coordinated Ir-NHC surface sites

In the previous section, we have demonstrated, using the combination of DNP SENS and EXAFS, that the carbene platinum complex immobilized onto an SBA-15 silica surface exhibits a well-defined structure and we have been able to determine the three-dimensional structure of this complex. While it was interesting as a proof-of-concept, it does not truly enable a structure-property relationship, as the Pt complex studied does not exhibit a particularly interesting catalytic activity! In this last chapter, we propose to investigate the structure of a low-coordinated Ir(I) complex immobilized onto SBA-15 silica, which is represented on FIGURE 7.1**(a)**. In 2015, Romanenko *et al.* have demonstrated that this Ir(I) complex exhibits exceptional catalytic performance in the hydrogenation of trans-stillbene whereas its molecular analog version is far less active.[120] On FIGURE 7.1**(b)** the difference in terms of catalytic performance of the two catalysts is striking. It is known that immobilization of the catalyst onto a surface prevent bimolecular deactivation process of the Ir(I) center. Additionally, the ^{1}H-^{13}C DNP SENS HETCOR spectrum has allowed the authors to qualitatively evidence the existence of additional stabilizing interactions between the surface and the iridium in the supported catalyst version.[120]

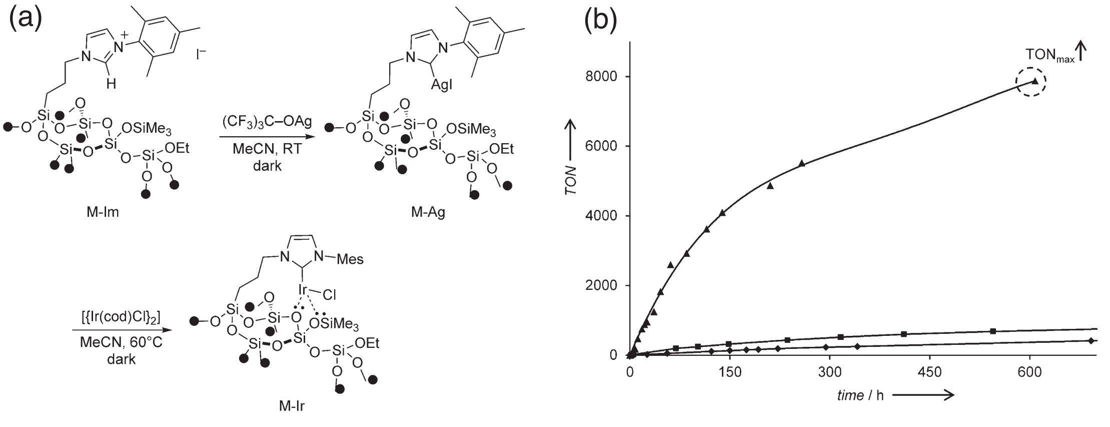

FIGURE 7.1: **(a)** Synthesis route and structure of the low coordinated Ir(I) material reported by Romanenko *et al.*. **(b)** TON as function of lifetime for the supported Ir(I) material and its molecular analogue. Reprinted (adapted) with permission from [120]. Copyright 2015 Wiley-VCH.

Here we propose to quantitatively investigate this Ir(I) catalyst by implementing a similar 3D surface structure determination approach that the method designed for the platinum complex. Thus the materials, represented on FIGURE 7.2, have been formulated with ^{15}N isotopic labelling to enable constraint measurements with ^{29}Si-{^{15}N} and ^{13}C-{^{15}N} DNP SENS REDOR experiments. Additionally, the complexes are ^{13}C labeled at the carbene (C_6) position. This additional isotopic labeling will open new experimental possibilities regarding distance measurements and will allow one to orient the imidazole ring with respect to the silica support, which could not have been done by NMR in the previous study. In addition, we will be able to measure ^{13}C-^{13}C DQ build-up curves under DNP conditions to determine the C_6-C_2 distances and hence constrains the orientation of the imidazolium ring. In the previous study, this orientation has been set based on DFT structure optimization.

FIGURE 7.2 shows the $^{13}C\{^{1}H\}$ and $^{15}N\{^{1}H\}$ DNP SENS CPMAS spectra on the three labelled materials (FIGURE 7.2). The $^{13}C\{^{1}H\}$ CPMAS spectra clearly demonstrates the metallation from the NHC precatalyst to the silver materials has a partial yield. In contrast the transmetallation is complete as evidence by the $^{15}N\{^{1}H\}$ CPMAS spectra recorded on N_1-labelled materials. Thus both the silver- and iridium-based materials still contains a non-negligible amount of the starting ligand, which will have to be considered in the structure determination.

This issue can be solved by implementing selective recoupling NMR experiments that will exploit the fact that the carbene resonances in the organic and organometallic ligands have very distinct ^{13}C chemical shifts. Selective REDOR pulse sequences have been developed for distance measurement in fully labeled solid proteins. [187] This will lead to the determination of three unambiguous distance restraints between the (labeled) carbene and the surface silicon atoms in the Ir-materials. The ^{15}N chemical shifts of the N_1 atom in the organic and organometallic NHC ligands are too close to enable a selective recoupling of the ^{29}Si-{^{15}N} dipolar interactions.

These approaches are currently under investigations. We envision these methods can (*i*) demonstrate that 3D surface structure determination allows structure-property relationship on catalytically relevant materials and (*ii*) address surface characterization of a large number of immobilized catalyst where the conversion of surface sites is incomplete during the synthesis.

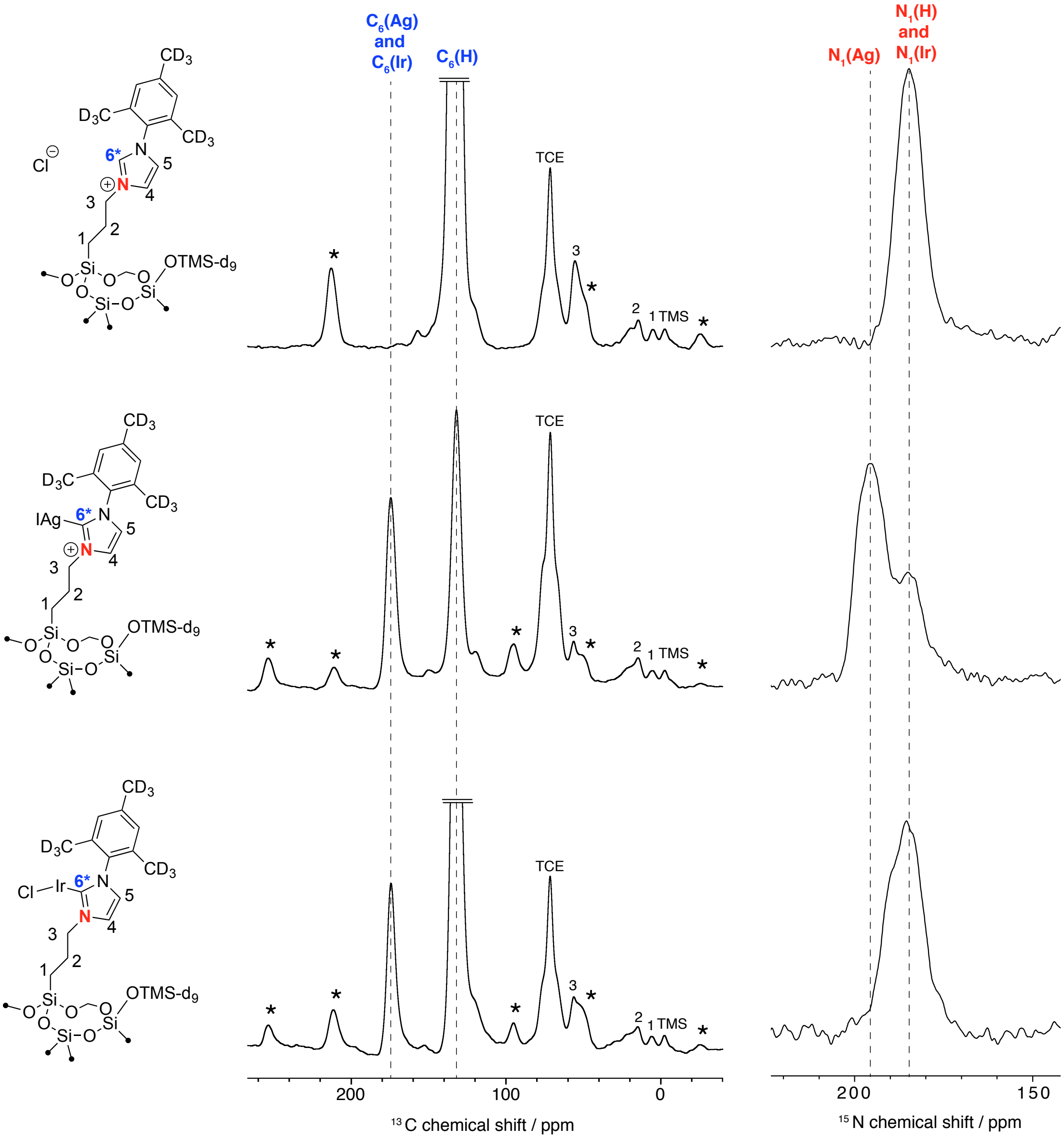

Figure 7.2: Materials structure along with their $^{13}C\{^{1}H\}$ and $^{15}N\{^{1}H\}$ DNP SENS CPMAS. N_1 and C_6 are isotopically enriched.

Chapter 8

Conclusions

The present manuscript comes to its end. It has been mainly focused on introducing three-dimensional structure determination of single surface sites using the DNP SENS approach. In the beginning of this work, the 3D structure of organometallic ligands anchored at a surface was never observed. It was not even known if such surface sites exhibited a well-defined structure or were completely disordered structures. Combining DNP SENS, with EXAFS, we have been able to demonstrate that a Pt organometallic complex immobilized onto SBA-15 silica has a well-defined structure and the organic moiety adopts a conformation so that surface-metal interactions are permitted. We note that we determined the structure in the presence of an organic solvent, which mimics the conditions of the catalyzed reaction (with the exception of the temperature). We believe that the ability to obtain 3D surface sites structure will facilitate the implementation of structure-activity relationships in many modern materials in particular for those relevant in heterogeneous catalysis. Thus, current investigations focus on the structure of a low-coordinated Ir(I) immobilized catalyst that is showing high catalytic activity in its immobilized version whereas its molecular analog is far less active.

In parallel, more fundamental aspects of DNP MAS have been investigated in order to expand the application range of Dynamic Nuclear Polarization NMR. First, by implementing fast Magic Angle Spinning conditions, we have observed that the MAS rate is not preventing high DNP enhancements with the gold standard AMUPOL in water/glycerol. However, we have reported that fast spinning has a dramatic effect on signal quenching. New polarizing agents should be able to circumvent this limitation. For example, there is no depolarization for radicals performing OE DNP and thus the BDPA radical is a promising system to perform DNP MAS at fast spinning. Alternatively, CE DNP at fast MAS would lead to higher sensitivity using biradicals made of two narrow line radical anchored. In this case, lower depolarization effect can be expected. However, this type of radical is still complicated to obtained and the hybrid approach where a narrow line radical and a broad line radical are combined (*e.g.* for TEMTri-POL [104]) is a promising alternative.

Second, a new DNP matrix based on polyacrylamide gels has been introduced. It allows to characterize of CdTe COOH quantum dots and prevents the aggregation of the particles when cooling the sample.

Third, so as to have a better understanding of the DNP SENS experiment and in particular of incipient wetness impregnation, which is a key step to perform the experiment, we have analyzed some primary aspects of the approach on mesoporous materials. In particular, we found that spin diffusion is playing an important role and a numerical spin diffusion model adapted to mesoporous materials have allowed measuring pore lengths.

DNP MAS is currently a vibrant approach in SSNMR as it allows to implement experiments that were not possible before and to get unprecedented information at the atomic scale. However, during this thesis, going more deeply in fundamental aspects of DNP SENS, it is clear that the application of DNP MAS is strongly dependent on the nature of the sample of interest. There are still many samples where DNP MAS is not meeting up to the expectations, in particular in the field of structural biology where very poor NMR resolution are obtained due to important heterogeneous line broadenings. In material, investigation of radical-sensitive material is still challenging. Recent introduction of dendritic binitroxides, or [137] silica wall-embedded radical [172, 173] are promising versatile strategies to study radical-sensitive material with DNP MAS.

List of publications

- Publications corresponding to a chapter in this thesis:

  J. Viger-Gravel †, P. Berruyer †, D. Gajan, J.M. Basset, A. Lesage, P. Tordo, O. Ouari, L. Emsley. Frozen acrylamide gels as DNP matrix. *Angew. Chem. Int. Ed.*, Accepted article, DOI: 10.1002/anie.201703758 († authors contributed equally)

  P. Berruyer, M. Lelli, M.P. Conley, D.L. Silverio, C.M. Widdifield, G. Siddiqi, D. Gajan, A. Lesage, C. Copéret, L. Emsley. Three-Dimensional Structure Determination of Surface Sites. *J. Am. Chem. Soc.* **2017**, *139*, 849-855.

  S.R. Chaudhari, P. Berruyer, D. Gajan, C. Reiter, F. Engelke, D.L. Silverio, C. Copéret, M. Lelli, A. Lesage, L. Emsley. Dynamic nuclear polarization at 40 kHz magic angle spinning. *Phys. Chem. Chem. Phys.* **2016**, *18*, 10616-10622.

- Other contributions:

  F.M. Wisser, P. Berruyer, L. Cardenas, E.A. Quadrelli, A. Lesage, J. Canivet, D. Farrusseng. Tailoring the local electronic structure of heterogenized rhodium photocatalysts within microporous supports. *Submitted.*

  A.C. Pinon, J. Schlagnitweit, P. Berruyer, A.J. Rossini, M. Lelli, E. Socie, M.X. Tang, T. Pham, A. Lesage, S. Schantz, L. Emsley. Measuring Nano to Micro Structures From Relayed DNP NMR. *Submitted*

  S.R. Chaudhari, D. Wisser, A.C. Pinon, P. Berruyer, P. Tordo, O. Ouari, C. Reiter, F. Engelke, C. Copéret, M. Lelli, A. Lesage, L. Emsley. Dynamic Nuclear

Polarization Efficiency Increased by Very Fast Magic Angle Spinning. *Submitted.*

D.L. Silverio, D. L., H.A van Kalkeren, T.C. Ong, M. Baudin, M. Yulikov, L. Veyre, P. Berruyer, S. Chaudhari, D. Gajan, D. Baudouin, M. Cavaillès, B. Vuichoud, A. Bornet, G. Jeschke, G. Bodenhausen, A. Lesage, L. Emsley, S. Jannin, C. Thieuleux, C. Copéret. Tailored Polarizing Hybrid Solids with Nitroxide Radicals Localized in Mesostructured Silica Walls. *Helv. Chim. Acta* **2017**, *38*, e1700101.

T.K. Todorova, X. Rozanska, C. Gervais, A. Legrand, L.N. Ho, P. Berruyer, A. Lesage, L. Emsley, D. Farrusseng, J. Canivet, C. Mellot-Draznieks. Molecular Level Characterization of the Structure and Interactions in Peptide-Functionalized Metal-Organic Frameworks. *Chem. - A Eur. J.* **2016**, *22*, 16531-16538.

Lexique

BET	Brunauer, Emmett, and Teller
BJH	Barrett-Joyner-Halenda
CE	Cross Effect
CP	Cross Polarization
CPMG	Carr-Purcell-Meiboom-Gill
CW	Continuous Waves
DCP	Double Cross Polarization
DNP	Dynamic Nuclear Polarization
EPR	Electron Paramagnetic Resonance
HETCOR	Heteronuclear Correlation
INADEQUATE	Incredible Natural-Abundance DoublE-QuAntum Transfer Experiment
INEPT	Insensitive Nuclei Enhanced by Polarization Transfer
LT	Low Temperature
MAS	Magic Angle Spinning
MSN	Mesoporous Silica Nanoparticles
NMR	Nuclear Magnetic Resonance
OE	Overhauser Effect
PFP	(Pentafluorophenyl)propyl
POSS	Polyhedral Oligomeric Silsesquioxanes
SE	Solid Effect
SENS	Surface Enhanced NMR Spectroscopy
SHC	Supported Homogenous Catalysis
SOMC	Surface Organometallic Catalysis
SSNMR	Solid-State NMR
TCE	Tetrachloroethane

Bibliography

[1] D. G. de Oteyza, P. Gorman, Y.-C. Chen, S. Wickenburg, A. Riss, D. J. Mowbray, G. Etkin, Z. Pedramrazi, H.-Z. Tsai, A. Rubio, M. F. Crommie, F. R. Fischer. Direct Imaging of Covalent Bond Structure in Single-Molecule Chemical Reactions. *Science* **2013**, *340*, 1434–1437.

[2] F. Blanc, C. Copéret, A. Lesage, L. Emsley. High resolution solid state NMR spectroscopy in surface organometallic chemistry: access to molecular understanding of active sites of well-defined heterogeneous catalysts. *Chem. Soc. Rev.* **2008**, *37*, 518–26.

[3] A. Marchetti, J. Chen, Z. Pang, S. Li, D. Ling, F. Deng, X. Kong. Understanding Surface and Interfacial Chemistry in Functional Nanomaterials via Solid-State NMR. *Adv. Mater.* **2017**, *29*, 1605895.

[4] T. Tsubogo, H. Oyamada, S. Kobayashi. Multistep continuous-flow synthesis of (R)- and (S)-rolipram using heterogeneous catalysts. *Nature* **2015**, *520*, 329–332.

[5] C. Copéret, M. Chabanas, R. Petroff Saint-Arroman, J.-M. Basset. Homogeneous and Heterogeneous Catalysis: Bridging the Gap through Surface Organometallic Chemistry. *Angew. Chemie Int. Ed.* **2003**, *42*, 156–181.

[6] D. Astruc, *Organometallic Chemistry and Catalysis*, Springer Berlin Heidelberg, Berlin, Heidelberg, **2007**.

[7] C. Copéret, J.-M. Basset. Strategies to Immobilize Well-Defined Olefin Metathesis Catalysts: Supported Homogeneous Catalysisvs. Surface Organometallic Chemistry. *Adv. Synth. Catal.* **2007**, *349*, 78–92.

[8] C. Copéret, A. Comas-Vives, M. P. Conley, D. P. Estes, A. Fedorov, V. Mougel, H. Nagae, F. Núñez-Zarur, P. A. Zhizhko. Surface Organometallic and Coordination Chemistry toward Single-Site Heterogeneous Catalysts: Strategies, Methods, Structures, and Activities. *Chem. Rev.* **2016**, *116*, 323–421.

[9] M. Trueba, S. P. Trasatti. γ-Alumina as a Support for Catalysts: A Review of Fundamental Aspects. *Eur. J. Inorg. Chem.* **2005**, *2005*, 3393–3403.

[10] G. S. Machado, K. A. D. d. F. Castro, O. J. de Lima, E. J. Nassar, K. J. Ciuffi, S. Nakagaki. Aluminosilicate obtained by sol-gel process as support for an anionic iron porphyrin: Development of a selective and reusable catalyst for oxidation reactions. *Colloids Surfaces A Physicochem. Eng. Asp.* **2009**, *349*, 162–169.

[11] H. E. Bergna (Ed.), *The Colloid Chemistry of Silica*, Vol. 234 of *Advances in Chemistry*, American Chemical Society, Washington DC, **1994**.

[12] A. Rimola, D. Costa, M. Sodupe, J.-F. Lambert, P. Ugliengo. Silica surface features and their role in the adsorption of biomolecules: computational modeling and experiments. *Chem. Rev.* **2013**, *113*, 4216–313.

[13] J. M. Basset, R. Ugo, *On the Origins and Development of Surface Organometallic Chemistry* in *Mod. Surf. Organomet. Chem.*, J.-M. Basset, R. Psaro, D. Roberto, R. Ugo (Eds.), Wiley-VCH Verlag GmbH and Co. KGaA, Weinheim, Germany, **2009**, pp. 1–21.

[14] F. Quignard, C. Lecuyer, C. Bougault, F. Lefebvre, A. Choplin, D. Olivier, J. M. Basset. Surface organometallic chemistry: synthesis and characterization of a tris(neopentyl)zirconium(IV) complex grafted to the surface of a partially dehydroxylated silica. *Inorg. Chem.* **1992**, *31*, 928–930.

[15] C. Thieuleux, E. A. Quadrelli, J.-m. Basset, J. Döbler, J. Sauer. Methane activation by silica-supported Zr(IV) hydrides: the dihydride [(SiO)2ZrH2] is much faster than the monohydride [(SiO)3ZrH]. *Chem. Commun.* **2004**, 1729–1731.

[16] J. S. Beck, J. C. Vartuli, W. J. Roth, M. E. Leonowicz, C. T. Kresge, K. D. Schmitt, C. T. W. Chu, D. H. Olson, E. W. Sheppard, S. B. McCullen, J. B. Higgins, J. L. Schlenker. A new family of mesoporous molecular sieves prepared with liquid crystal templates. *J. Am. Chem. Soc.* **1992**, *114*, 10834–10843.

[17] C. T. Kresge, M. E. Leonowicz, W. J. Roth, J. C. Vartuli, J. S. Beck. Ordered mesoporous molecular sieves synthesized by a liquid-crystal template mechanism. *Nature* **1992**, *359*, 710–712.

[18] D. Zhao, J. Feng, Q. Huo, N. Melosh, G. H. Fredrickson, B. F. Chmelka, G. D. Stucky. Triblock Copolymer Syntheses of Mesoporous Silica with Periodic 50 to 300 Angstrom Pores. *Science* **1998**, *279*, 548–552.

[19] D. Zhao, Q. Huo, J. Feng, B. F. Chmelka, G. D. Stucky. Nonionic Triblock and Star Diblock Copolymer and Oligomeric Surfactant Syntheses of Highly Ordered, Hydrothermally Stable, Mesoporous Silica Structures. *J. Am. Chem. Soc.* **1998**, *120*, 6024–6036.

[20] F. Hoffmann, M. Cornelius, J. Morell, M. Fröba. Silica-Based Mesoporous Organic-Inorganic Hybrid Materials. *Angew. Chemie Int. Ed.* **2006**, *45*, 3216–3251.

[21] L. Zhuravlev. The surface chemistry of amorphous silica. Zhuravlev model. *Colloids Surfaces A Physicochem. Eng. Asp.* **2000**, *173*, 1–38.

[22] J.-M. Basset, J.-P. Candy, C. Copéret, *Surface Organometallic Chemistry* in *Compr. Organomet. Chem. III*, Elsevier, **2007**, pp. 499–553.

[23] J.-M. Basset, R. Psaro, D. Roberto, R. Ugo (Eds.), *Modern Surface Organometallic Chemistry*, Wiley-VCH Verlag GmbH & Co. KGaA, Weinheim, Germany, **2009**.

[24] M. P. Conley, C. Copéret, C. Thieuleux. Mesostructured Hybrid Organic-Silica Materials: Ideal Supports for Well-Defined Heterogeneous Organometallic Catalysts. *ACS Catal.* **2014**, *4*, 1458–1469.

[25] A. J. Ward, A. F. Masters, T. Maschmeyer, *Transition Metal Single Site Catalysts From Homogeneous to Immobilized Systems* in *Mod. Surf. Organomet. Chem.*,

Wiley-VCH Verlag GmbH and Co. KGaA, Weinheim, Germany, **2009**, pp. 167–237.

[26] Q. Fu, W.-X. Li, Y. Yao, H. Liu, H.-Y. Su, D. Ma, X.-K. Gu, L. Chen, Z. Wang, H. Zhang, B. Wang, X.-h. Bao. Interface-Confined Ferrous Centers for Catalytic Oxidation. *Science* **2010**, *328*, 1141–1144.

[27] G. E. Maciel, W. Sindorf. Silicon-29 Nuclear Magnetic Resonance Study of the Surface of Silica Gel By Cross Polarization and Mangic-Angle Spinning. *J. Am. Chem. Soc.* **1980**, *102*, 7606–7607.

[28] E. L. Hahn, S. R. Hartmann. Nuclear Double Resonance in the Rotating Frame. *Phys. Rev.* **1962**, *128*, 2042–2053.

[29] F. M. Lurie, C. P. Slichter. Spin Temperature in Nuclear Double Resonance. *Phys. Rev.* **1964**, *133*, A1108–A1122.

[30] A. Pines, M. G. Gibby, J. S. Waugh. Proton-Enhanced Nuclear Induction Spectroscopy. A Method for High Resolution NMR of Dilute Spins in Solids. *J. Chem. Phys.* **1972**, *56*, 1776.

[31] A. Pines, M. G. Gibby, J. S. Waugh. Proton-enhanced NMR of dilute spins in solids. *J. Chem. Phys.* **1973**, *59*, 569.

[32] V. J. Bartuska, G. E. Maciel, W. Sindorf. Characterization of silica-attached systems by 29Si and 13C cross-polarization and magic-angle spinning nuclear magnetic resonance. *J. Chromatogr.* **1981**, *205*, 438–443.

[33] W. Sindorf, G. E. Maciel. 29Si CPMAS NMR Studies of Methylchlorosilane Reactions on Silica Gel. *J. Am. Chem. Soc.* **1981**, *103*, 4263–4265.

[34] R. P. Saint-Arroman, M. Chabanas, A. Baudouin, C. Copéret, J.-M. Basset, A. Lesage, L. Emsley. Characterization of Surface Organometallic Complexes Using High Resolution 2D Solid-State NMR Spectroscopy. Application to the Full Characterization of a Silica Supported Metal Carbyne:SiO-Mo(C-Bu-t)(CH2-Bu-t)2. *J. Am. Chem. Soc.* **2001**, *123*, 3820–3821.

[35] A. Lesage, L. Emsley, M. Chabanas, C. Copéret, J. M. Basset. Observation of a H-agostic bond in a highly active rhenium-alkylidene olefin metathesis heterogeneous catalyst by two-dimensional solid-state NMR spectroscopy. *Angew. Chemie - Int. Ed.* **2002**, *41*, 4535–4538.

[36] K. C. Szeto, W. Sahyoun, N. Merle, J. L. Castelbou, N. Popoff, F. Lefebvre, J. Raynaud, C. Godard, C. Claver, L. Delevoye, R. M. Gauvin, M. Taoufik. Development of silica-supported frustrated Lewis pairs: highly active transition metal-free catalysts for the Z-selective reduction of alkynes. *Catal. Sci. Technol.* **2016**, *6*, 882–889.

[37] N. Merle, G. Girard, N. Popoff, A. De Mallmann, Y. Bouhoute, J. Tr?bosc, E. Berrier, J.-F. Paul, C. P. Nicholas, I. Del Rosal, L. Maron, R. M. Gauvin, L. Delevoye, M. Taoufik. On the Track to Silica-Supported Tungsten Oxo Metathesis Catalysts: Input from 17 O Solid-State NMR. *Inorg. Chem.* **2013**, *52*, 10119–10130.

[38] N. Merle, F. Le Qu?m?ner, Y. Bouhoute, K. C. Szeto, A. De Mallmann, S. Barman, M. K. Samantaray, L. Delevoye, R. M. Gauvin, M. Taoufik, J.-M. Basset. Well-Defined Molybdenum Oxo Alkyl Complex Supported on Silica by Surface Organometallic Chemistry: A Highly Active Olefin Metathesis Precatalyst. *J. Am. Chem. Soc.* **2017**, *139*, 2144–2147.

[39] S. Soignier, G. Saggio, M. Taoufik, J.-M. Basset, J. Thivolle-Cazat. Dynamic behaviour of tantalum hydride supported on silica or MCM-41 in the metathesis of alkanes. *Catal. Sci. Technol.* **2014**, *4*, 233–244.

[40] F. Rataboul, A. Baudouin, C. Thieuleux, L. Veyre, C. Copéret, J. Thivolle-Cazat, J.-M. Basset, A. Lesage, L. Emsley. Molecular Understanding of the Formation of Surface Zirconium Hydrides upon Thermal Treatment under Hydrogen of [(SiO)Zr(CH2tBu) 3] by Using Advanced Solid-State NMR Techniques. *J. Am. Chem. Soc.* **2004**, *126*, 12541–12550.

[41] P. Avenier, A. Lesage, M. Taoufik, A. Baudouin, A. De Mallmann, S. Fiddy, M. Vautier, L. Veyre, J.-M. Basset, L. Emsley, E. A. Quadrelli. Well-Defined Surface Imido Amido Tantalum(V) Species from Ammonia and Silica-Supported Tantalum Hydrides. *J. Am. Chem. Soc.* **2007**, *129*, 176–186.

[42] P. Avenier, M. Taoufik, A. Lesage, X. Solans-Monfort, A. Baudouin, A. de Mallmann, L. Veyre, J.-M. Basset, O. Eisenstein, L. Emsley, E. A. Quadrelli. Dinitrogen Dissociation on an Isolated Surface Tantalum Atom. *Science* **2007**, *317*, 1056–1060.

[43] J. Trébosc, J. W. Wiench, S. Huh, V. S.-Y. Lin, M. Pruski. Solid-state NMR study of MCM-41-type mesoporous silica nanoparticles. *J. Am. Chem. Soc.* **2005**, *127*, 3057–3068.

[44] J. Trebosc, J. W. Wiench, S. Huh, V. S.-Y. Lin, M. Pruski. Studies of Organically Functionalized Mesoporous Silicas Using Heteronuclear Solid-State Correlation NMR Spectroscopy under Fast Magic Angle Spinning. *J. Am. Chem. Soc.* **2005**, *127*, 7587–7593.

[45] Y. Ishii, R. Tycko. Sensitivity Enhancement in Solid State 15N NMR by Indirect Detection with High-Speed Magic Angle Spinning. *J. Magn. Reson.* **2000**, *142*, 199–204.

[46] J. W. Wiench, C. E. Bronnimann, V. S. Lin, M. Pruski. Chemical shift correlation NMR spectroscopy with indirect detection in fast rotating solids: studies of organically functionalized mesoporous silicas. *J. Am. Chem. Soc.* **2007**, *129*, 12076–7.

[47] J. L. Rapp, Y. Huang, M. Natella, Y. Cai, V. S. Lin, M. Pruski. A solid-state NMR investigation of the structure of mesoporous silica nanoparticle supported rhodium catalysts. *Solid State Nucl. Magn. Reson.* **2009**, *35*, 82–86.

[48] K. Mao, J. W. Wiench, V. S. Lin, M. Pruski. Indirectly detected through-bond chemical shift correlation NMR spectroscopy in solids under fast MAS: Studies of organic-inorganic hybrid materials. *J. Magn. Reson.* **2009**, *196*, 92–95.

[49] K. Mao, T. Kobayashi, J. W. Wiench, H.-T. Chen, C.-H. Tsai, V. S.-Y. Lin, M. Pruski. Conformations of Silica-Bound (Pentafluorophenyl)propyl Groups Determined by Solid-State NMR Spectroscopy and Theoretical Calculations. *J. Am. Chem. Soc.* **2010**, *132*, 12452–12457.

[50] C.-H. Tsai, H.-T. Chen, S. M. Althaus, K. Mao, T. Kobayashi, M. Pruski, V. S.-Y. Lin. Rational Catalyst Design: A Multifunctional Mesoporous Silica Catalyst for Shifting the Reaction Equilibrium by Removal of Byproduct. *ACS Catal.* **2011**, *1*, 729–732.

[51] F. Blanc, J.-M. Basset, C. Copéret, A. Sinha, Z. J. Tonzetich, R. R. Schrock, X. Solans-Monfort, E. Clot, O. Eisenstein, A. Lesage, L. Emsley. Dynamics of Silica-Supported Catalysts Determined by Combining Solid-State NMR Spectroscopy and DFT Calculations. *J. Am. Chem. Soc.* **2008**, *130*, 5886–5900.

[52] J. Gath, G. L. Hoaston, R. L. Vold, R. Berthoud, C. Copéret, M. Grellier, S. Sabo-Etienne, A. Lesage, L. Emsley. Motional heterogeneity in single-site silica-supported species revealed by deuteron NMR. *Phys. Chem. Chem. Phys.* **2009**, *11*, 6962.

[53] E. A. Quadrelli, *Molecular Insight for Silica-Supported Organometallic Chemistry through Transition Metal Silsesquioxanes* in *Mod. Surf. Organomet. Chem.*, Wiley-VCH Verlag GmbH & Co. KGaA, Weinheim, Germany, **2009**, pp. 557–598.

[54] M. Chabanas, A. Baudouin, C. Copéret, J.-M. Basset, W. Lukens, A. Lesage, S. Hediger, L. Emsley. Perhydrocarbyl Re VII Complexes: Comparison of Molecular and Surface Complexes. *J. Am. Chem. Soc.* **2003**, *125*, 492–504.

[55] F. Blanc, C. Copéret, J. Thivolle-Cazat, J.-M. Basset, A. Lesage, L. Emsley, A. Sinha, R. R. Schrock. Surface versus Molecular Siloxy Ligands in Well-Defined Olefin Metathesis Catalysts: [(RO)3SiOMo(NAr)(CHtBu)(CH2tBu)]. *Angew. Chemie Int. Ed.* **2006**, *45*, 1216–1220.

[56] A. W. Overhauser. Polarization of Nuclei in Metals. *Phys. Rev.* **1953**, *92*, 411–415.

[57] T. R. Carver, C. P. Slichter. Polarization of Nuclear Spins in Metals. *Phys. Rev.* **1953**, *92*, 212–213.

[58] A. Abragam, W. Proctor. Une nouvelle méthode de polarisation dynamique des noyaux atomiques dans les solides. *C. R. Hebd. Seances Acad. Sci.* **1958**, *246*, 2253–2256.

[59] A. Kessenikh, V. Lushchikov, A. Manenkov, Y. Taran. Proton Polarization in irradiated polyethylenes. *Sov. Phys. Solid State* **1963**, *5*, 321–329.

[60] A. J. Rossini, A. Zagdoun, M. Lelli, D. Gajan, F. Rascón, M. Rosay, W. E. Maas, C. Copéret, A. Lesage, L. Emsley. One hundred fold overall sensitivity enhancements for Silicon-29 NMR spectroscopy of surfaces by dynamic nuclear polarization with CPMG acquisition. *Chem. Sci.* **2012**, *3*, 108–115.

[61] L. Becerra, G. Gerfen, B. Bellew, J. Bryant, D. Hall, S. Inati, R. Weber, S. Un, T. Prisner, A. McDermoot, K. Fishbein, K. Kreischer, R. Temkin, D. Singel, R. Griffin. A Spectrometer for Dynamic Nuclear Polarization and Electron Paramagnetic Resonance at High Frequencies. *J. Magn. Reson. Ser. A* **1995**, *117*, 28–40.

[62] G. J. Gerfen, L. R. Becerra, D. A. Hall, R. G. Griffin, R. J. Temkin, D. J. Singel. High frequency (140 GHz) dynamic nuclear polarization: Polarization transfer to a solute in frozen aqueous solution. *J. Chem. Phys.* **1995**, *102*, 9494–9497.

[63] R. G. Griffin. Clear signals from surfaces. *Nature* **2010**, *468*, 3–4.

[64] L. B. Andreas, A. B. Barnes, B. Corzilius, J. J. Chou, E. A. Miller, M. Caporini, M. Rosay, R. G. Griffin. Dynamic Nuclear Polarization Study of Inhibitor Binding to the M2 18-60 Proton Transporter from Influenza A. *Biochemistry* **2013**, *52*, 2774–2782.

[65] Ü. Akbey, A. H. Linden, H. Oschkinat. High-Temperature Dynamic Nuclear Polarization Enhanced Magic-Angle-Spinning NMR. *Appl. Magn. Reson.* **2012**, *43*, 81–90.

[66] Ü. Akbey, H. Oschkinat. Structural biology applications of solid state MAS DNP NMR. *J. Magn. Reson.* **2016**, *269*, 213–224.

[67] Q. Z. Ni, E. Markhasin, T. V. Can, B. Corzilius, K. O. Tan, A. B. Barnes, E. Daviso, Y. Su, J. Herzfeld, R. G. Griffin. Peptide and Protein Dynamics and Low-Temperature/DNP Magic Angle Spinning NMR. *J. Phys. Chem. B* **2017**, acs.jpcb.7b02066.

[68] P. C. A. van der Wel, K.-N. Hu, J. Lewandowski, R. G. Griffin. Dynamic Nuclear Polarization of Amyloidogenic Peptide Nanocrystals: GNNQQNY, a Core Segment of the Yeast Prion Protein Sup35p. *J. Am. Chem. Soc.* **2006**, *128*, 10840–10846.

[69] A. J. Rossini, A. Zagdoun, F. Hegner, M. Schwarzwälder, D. Gajan, C. Copéret, A. Lesage, L. Emsley. Dynamic Nuclear Polarization NMR Spectroscopy of Microcrystalline Solids. *J. Am. Chem. Soc.* **2012**, *134*, 16899–16908.

[70] G. Mollica, M. Dekhil, F. Ziarelli, P. Thureau, S. Viel. Quantitative structural constraints for organic powders at natural isotopic abundance using dynamic nuclear polarization solid-state NMR spectroscopy. *Angew. Chem. Int. Ed. Engl.* **2015**, *54*, 6028–6031.

[71] A. Lesage, M. Lelli, D. Gajan, M. a. Caporini, V. Vitzthum, P. Miéville, J. Alauzun, A. Roussey, C. Thieuleux, A. Mehdi, G. Bodenhausen, C. Coperet, L. Emsley. Surface Enhanced NMR Spectroscopy by Dynamic Nuclear Polarization. *J. Am. Chem. Soc.* **2010**, *132*, 15459–15461.

[72] M. Lelli, D. Gajan, A. Lesage, M. A. Caporini, V. Vitzthum, P. Miéville, F. Héroguel, F. Rascón, A. Roussey, C. Thieuleux, M. Boualleg, L. Veyre, G. Bodenhausen, C. Coperet, L. Emsley. Fast Characterization of Functionalized Silica Materials by Silicon-29 Surface-Enhanced NMR Spectroscopy Using Dynamic Nuclear Polarization. *J. Am. Chem. Soc.* **2011**, *133*, 2104–2107.

[73] M. A. Hope, D. M. Halat, P. C. M. M. Magusin, S. Paul, L. Peng, C. P. Grey. Surface-selective direct 17 O DNP NMR of CeO 2 nanoparticles. *Chem. Commun.* **2017**, *53*, 2142–2145.

[74] F. Blanc, S. Y. Chong, T. O. McDonald, D. J. Adams, S. Pawsey, M. A. Caporini, A. I. Cooper. Dynamic Nuclear Polarization NMR Spectroscopy Allows High-Throughput Characterization of Microporous Organic Polymers. *J. Am. Chem. Soc.* **2013**, *135*, 15290–15293.

[75] A. J. Rossini, A. Zagdoun, M. Lelli, A. Lesage, C. Copéret, L. Emsley. Dynamic Nuclear Polarization Surface Enhanced NMR Spectroscopy. *Acc. Chem. Res.* **2013**, *46*, 1942–1951.

[76] M. Rosay, L. Tometich, S. Pawsey, R. Bader, R. Schauwecker, M. Blank, P. M. Borchard, S. R. Cauffman, K. L. Felch, R. T. Weber, R. J. Temkin, R. G. Griffin, W. E. Maas. Solid-state dynamic nuclear polarization at 263 GHz: spectrometer design and experimental results. *Phys. Chem. Chem. Phys.* **2010**, *12*, 5850.

[77] M. Rosay, M. Blank, F. Engelke. Instrumentation for solid-state dynamic nuclear polarization with magic angle spinning NMR. *J. Magn. Reson.* **2016**, *264*, 88–98.

[78] T. Maly, G. T. Debelouchina, V. S. Bajaj, K.-N. Hu, C.-G. Joo, M. L. Mak-Jurkauskas, J. R. Sirigiri, P. C. a. van der Wel, J. Herzfeld, R. J. Temkin, R. G. Griffin. Dynamic nuclear polarization at high magnetic fields. *J. Chem. Phys.* **2008**, *128*, 052211.

[79] T. Can, Q. Ni, R. Griffin. Mechanisms of dynamic nuclear polarization in insulating solids. *J. Magn. Reson.* **2015**, *253*, 23–35.

[80] C. Griesinger, M. Bennati, H. Vieth, C. Luchinat, G. Parigi, P. Höfer, F. Engelke, S. Glaser, V. Denysenkov, T. Prisner. Dynamic nuclear polarization at high magnetic fields in liquids. *Prog. Nucl. Magn. Reson. Spectrosc.* **2012**, *64*, 4–28.

[81] T. V. Can, M. A. Caporini, F. Mentink-Vigier, B. Corzilius, J. J. Walish, M. Rosay, W. E. Maas, M. Baldus, S. Vega, T. M. Swager, R. G. Griffin. Overhauser effects in insulating solids. *J. Chem. Phys.* **2014**, *141*, 064202.

[82] S. Pylaeva, K. L. Ivanov, M. Baldus, D. Sebastiani, H. Elgabarty. Molecular Mechanism of Overhauser Dynamic Nuclear Polarization in Insulating Solids. *J. Phys. Chem. Lett.* **2017**, 2137–2142.

[83] B. Corzilius, A. A. Smith, R. G. Griffin. Solid effect in magic angle spinning dynamic nuclear polarization. *J. Chem. Phys.* **2012**, *137*, 054201.

[84] K.-N. Hu, V. S. Bajaj, M. Rosay, R. G. Griffin. High-frequency dynamic nuclear polarization using mixtures of TEMPO and trityl radicals. *J. Chem. Phys.* **2007**, *126*, 044512.

[85] K. R. Thurber, R. Tycko. Theory for cross effect dynamic nuclear polarization under magic-angle spinning in solid state nuclear magnetic resonance: The importance of level crossings. *J. Chem. Phys.* **2012**, *137*, 084508.

[86] F. Mentink-Vigier, Ü. Akbey, Y. Hovav, S. Vega, H. Oschkinat, A. Feintuch. Fast passage dynamic nuclear polarization on rotating solids. *J. Magn. Reson.* **2012**, *224*, 13–21.

[87] B. Corzilius. Theory of solid effect and cross effect dynamic nuclear polarization with half-integer high-spin metal polarizing agents in rotating solids. *Phys. Chem. Chem. Phys.* **2016**, *18*, 27190–27204.

[88] D. Mance, P. Gast, M. Huber, M. Baldus, K. L. Ivanov. The magnetic field dependence of cross-effect dynamic nuclear polarization under magic angle spinning. *J. Chem. Phys.* **2015**, *142*, 234201.

[89] D. Gajan, A. Bornet, B. Vuichoud, J. Milani, R. Melzi, H. A. van Kalkeren, L. Veyre, C. Thieuleux, M. P. Conley, W. R. Gruning, M. Schwarzwalder, A. Lesage, C. Coperet, G. Bodenhausen, L. Emsley, S. Jannin. Hybrid polarizing solids for pure hyperpolarized liquids through dissolution dynamic nuclear polarization. *Proc. Natl. Acad. Sci.* **2014**, *111*, 14693–14697.

[90] K.-N. Hu, H.-h. Yu, T. M. Swager, R. G. Griffin. Dynamic Nuclear Polarization with Biradicals. *J. Am. Chem. Soc.* **2004**, *126*, 10844–10845.

[91] C. Sauvée, M. Rosay, G. Casano, F. Aussenac, R. T. Weber, O. Ouari, P. Tordo. Highly efficient, water-soluble polarizing agents for dynamic nuclear polarization at high frequency. *Angew. Chem. Int. Ed. Engl.* **2013**, *52*, 10858–10861.

[92] A. Zagdoun, A. J. Rossini, D. Gajan, A. Bourdolle, O. Ouari, M. Rosay, W. E. Maas, P. Tordo, M. Lelli, L. Emsley, A. Lesage, C. Copéret. Non-aqueous solvents for DNP surface enhanced NMR spectroscopy. *Chem. Commun.* **2012**, *48*, 654–656.

[93] H. Takahashi, D. Lee, L. Dubois, M. Bardet, S. Hediger, G. De Paëpe. Rapid Natural-Abundance 2D 13 C- 13 C Correlation Spectroscopy Using Dynamic Nu-

clear Polarization Enhanced Solid-State NMR and Matrix-Free Sample Preparation. *Angew. Chemie Int. Ed.* **2012**, *51*, 11766–11769.

[94] H. Takahashi, S. Hediger, G. De Paëpe. Matrix-free dynamic nuclear polarization enables solid-state NMR 13C-13C correlation spectroscopy of proteins at natural isotopic abundance. *Chem. Commun.* **2013**, *49*, 9479.

[95] C. Fernández-de Alba, H. Takahashi, A. Richard, Y. Chenavier, L. Dubois, V. Maurel, D. Lee, S. Hediger, G. De Paëpe. Matrix-Free DNP-Enhanced NMR Spectroscopy of Liposomes Using a Lipid-Anchored Biradical. *Chem. - A Eur. J.* **2015**, *21*, 4512–4517.

[96] J. R. Yarava, S. R. Chaudhari, A. J. Rossini, A. Lesage, L. Emsley. Solvent suppression in DNP enhanced solid state NMR. *J. Magn. Reson.* **2017**, *277*, 149–153.

[97] D. Lee, S. R. Chaudhari, G. De Paëpe. Solvent signal suppression for high-resolution MAS-DNP. *J. Magn. Reson.* **2017**, *278*, 60–66.

[98] Y. Matsuki, T. Maly, O. Ouari, H. Karoui, F. Le Moigne, E. Rizzato, S. Lyubenova, J. Herzfeld, T. Prisner, P. Tordo, R. G. Griffin. Dynamic nuclear polarization with a rigid biradical. *Angew. Chem. Int. Ed. Engl.* **2009**, *48*, 4996–5000.

[99] A. Zagdoun, G. Casano, O. Ouari, G. Lapadula, A. J. Rossini, M. Lelli, M. Baffert, D. Gajan, L. Veyre, W. E. Maas, M. Rosay, R. T. Weber, C. Thieuleux, C. Coperet, A. Lesage, P. Tordo, L. Emsley. A Slowly Relaxing Rigid Biradical for Efficient Dynamic Nuclear Polarization Surface-Enhanced NMR Spectroscopy: Expeditious Characterization of Functional Group Manipulation in Hybrid Materials. *J. Am. Chem. Soc.* **2012**, *134*, 2284–2291.

[100] A. Zagdoun, G. Casano, O. Ouari, M. Schwarzwälder, A. J. Rossini, F. Aussenac, M. Yulikov, G. Jeschke, C. Copéret, A. Lesage, P. Tordo, L. Emsley. Large Molecular Weight Nitroxide Biradicals Providing Efficient Dynamic Nuclear Polarization at Temperatures up to 200 K. *J. Am. Chem. Soc.* **2013**, *135*, 12790–12797.

[101] D. J. Kubicki, G. Casano, M. Schwarzwälder, S. Abel, C. Sauvée, K. Ganesan, M. Yulikov, A. J. Rossini, G. Jeschke, C. Copéret, A. Lesage, P. Tordo, O. Ouari,

L. Emsley. Rational design of dinitroxide biradicals for efficient cross-effect dynamic nuclear polarization. *Chem. Sci.* **2016**, *7*, 550–558.

[102] D. J. Kubicki, A. J. Rossini, A. Purea, A. Zagdoun, O. Ouari, P. Tordo, F. Engelke, A. Lesage, L. Emsley. Amplifying Dynamic Nuclear Polarization of Frozen Solutions by Incorporating Dielectric Particles. *J. Am. Chem. Soc.* **2014**, *136*, 15711–15718.

[103] V. K. Michaelis, A. A. Smith, B. Corzilius, O. Haze, T. M. Swager, R. G. Griffin. High-field 13C dynamic nuclear polarization with a radical mixture. *J. Am. Chem. Soc.* **2013**, *135*, 2935–2938.

[104] G. Mathies, M. A. Caporini, V. K. Michaelis, Y. Liu, K.-N. Hu, D. Mance, J. L. Zweier, M. Rosay, M. Baldus, R. G. Griffin. Efficient Dynamic Nuclear Polarization at 800 MHz/527 GHz with Trityl-Nitroxide Biradicals. *Angew. Chemie Int. Ed.* **2015**, *54*, 11770–11774.

[105] M. Kaushik, M. Qi, A. Godt, B. Corzilius. Bis-Gadolinium Complexes for Solid Effect and Cross Effect Dynamic Nuclear Polarization. *Angew. Chemie Int. Ed.* **2017**, *56*, 4295–4299.

[106] T.-C. Ong, M. L. Mak-Jurkauskas, J. J. Walish, V. K. Michaelis, B. Corzilius, A. A. Smith, A. M. Clausen, J. C. Cheetham, T. M. Swager, R. G. Griffin. Solvent-Free Dynamic Nuclear Polarization of Amorphous and Crystalline ortho -Terphenyl. *J. Phys. Chem. B* **2013**, *117*, 3040–3046.

[107] M. Lelli, S. R. Chaudhari, D. Gajan, G. Casano, A. J. Rossini, O. Ouari, P. Tordo, A. Lesage, L. Emsley. Solid-State Dynamic Nuclear Polarization at 9.4 and 18.8 T from 100 K to Room Temperature. *J. Am. Chem. Soc.* **2015**, *137*, 14558–14561.

[108] T. Kobayashi, O. Lafon, A. S. Lilly Thankamony, I. I. Slowing, K. Kandel, D. Carnevale, V. Vitzthum, H. Vezin, J.-P. Amoureux, G. Bodenhausen, M. Pruski. Analysis of sensitivity enhancement by dynamic nuclear polarization in solid-state NMR: a case study of functionalized mesoporous materials. *Phys. Chem. Chem. Phys.* **2013**, *15*, 5553.

[109] F. Mentink-Vigier, S. Paul, D. Lee, A. Feintuch, S. Hediger, S. Vega, G. De Paëpe. Nuclear depolarization and absolute sensitivity in magic-angle spinning cross effect dynamic nuclear polarization. *Phys. Chem. Chem. Phys.* **2015**, *17*, 21824–21836.

[110] B. Corzilius, L. B. Andreas, A. A. Smith, Q. Z. Ni, R. G. Griffin. Paramagnet induced signal quenching in MAS-DNP experiments in frozen homogeneous solutions. *J. Magn. Reson.* **2014**, *240*, 113–123.

[111] K. R. Thurber, R. Tycko. Perturbation of nuclear spin polarizations in solid state NMR of nitroxide-doped samples by magic-angle spinning without microwaves. *J. Chem. Phys.* **2014**, *140*, 184201.

[112] A. Henstra, P. Dirksen, J. Schmidt, W. Wenckebach. Nuclear spin orientation via electron spin locking (NOVEL). *J. Magn. Reson.* **1988**, *77*, 389–393.

[113] A. Henstra, W. Wenckebach. The theory of nuclear orientation via electron spin locking (NOVEL). *Mol. Phys.* **2008**, *106*, 859–871.

[114] T. V. Can, J. J. Walish, T. M. Swager, R. G. Griffin. Time domain DNP with the NOVEL sequence. *J. Chem. Phys.* **2015**, *143*, 054201.

[115] G. Mathies, S. Jain, M. Reese, R. G. Griffin. Pulsed Dynamic Nuclear Polarization with Trityl Radicals. *J. Phys. Chem. Lett.* **2016**, *7*, 111–116.

[116] T. V. Can, R. T. Weber, J. J. Walish, T. M. Swager, R. G. Griffin. Ramped-amplitude NOVEL. *J. Chem. Phys.* **2017**, *146*, 154204.

[117] a. Henstra, P. Dirksen, W. Wenckebach. Enhanced dynamic nuclear polarization by the integrated solid effect. *Phys. Lett. A* **1988**, *134*, 134–136.

[118] A. Zagdoun, A. J. Rossini, M. P. Conley, W. R. Grüning, M. Schwarzwälder, M. Lelli, W. T. Franks, H. Oschkinat, C. Copéret, L. Emsley, A. Lesage. Improved Dynamic Nuclear Polarization Surface-Enhanced NMR Spectroscopy through Controlled Incorporation of Deuterated Functional Groups. *Angew. Chemie Int. Ed.* **2013**, *52*, 1222–1225.

[119] M. K. Samantaray, J. Alauzun, D. Gajan, S. Kavitake, A. Mehdi, L. Veyre, M. Lelli, A. Lesage, L. Emsley, C. Copéret, C. Thieuleux. Evidence for Metal-Surface Interactions and Their Role in Stabilizing Well-Defined Immobilized Ru-NHC Alkene Metathesis Catalysts. *J. Am. Chem. Soc.* **2013**, *135*, 3193–3199.

[120] I. Romanenko, D. Gajan, R. Sayah, D. Crozet, E. Jeanneau, C. Lucas, L. Leroux, L. Veyre, A. Lesage, L. Emsley, E. Lacôte, C. Thieuleux. Iridium(I)/N-Heterocyclic Carbene Hybrid Materials: Surface Stabilization of Low-Valent Iridium Species for High Catalytic Hydrogenation Performance. *Angew. Chemie Int. Ed.* **2015**, *54*, 12937–12941.

[121] D. M. D'Alessandro, B. Smit, J. R. Long. Carbon Dioxide Capture: Prospects for New Materials. *Angew. Chemie Int. Ed.* **2010**, *49*, 6058–6082.

[122] A. J. Rossini, A. Zagdoun, M. Lelli, J. Canivet, S. Aguado, O. Ouari, P. Tordo, M. Rosay, W. E. Maas, C. Copéret, D. Farrusseng, L. Emsley, A. Lesage. Dynamic nuclear polarization enhanced solid-state NMR spectroscopy of functionalized metal-organic frameworks. *Angew. Chem. Int. Ed. Engl.* **2012**, *51*, 123–127.

[123] T. Kobayashi, F. A. Perras, T. W. Goh, T. L. Metz, W. Huang, M. Pruski. DNP-Enhanced Ultrawideline Solid-State NMR Spectroscopy: Studies of Platinum in Metal-Organic Frameworks. *J. Phys. Chem. Lett.* **2016**, 2322–2327.

[124] P. Wolf, M. Valla, A. J. Rossini, A. Comas-Vives, F. Núñez-Zarur, B. Malaman, A. Lesage, L. Emsley, C. Copéret, I. Hermans. NMR Signatures of the Active Sites in Sn-β Zeolite. *Angew. Chemie Int. Ed.* **2014**, *53*, 10179–10183.

[125] R. P. Sangodkar, B. J. Smith, D. Gajan, A. J. Rossini, L. R. Roberts, G. P. Funkhouser, A. Lesage, L. Emsley, B. F. Chmelka. Influences of Dilute Organic Adsorbates on the Hydration of Low-Surface-Area Silicates. *J. Am. Chem. Soc.* **2015**, *137*, 8096–8112.

[126] L. Piveteau, T.-C. Ong, A. J. Rossini, L. Emsley, C. Copéret, M. V. Kovalenko. Structure of Colloidal Quantum Dots from Dynamic Nuclear Polarization Surface Enhanced NMR Spectroscopy. *J. Am. Chem. Soc.* **2015**, *137*, 13964–13971.

[127] R. L. Johnson, F. A. Perras, T. Kobayashi, T. J. Schwartz, J. A. Dumesic, B. H. Shanks, M. Pruski. Identifying low-coverage surface species on supported noble metal nanoparticle catalysts by DNP-NMR. *Chem. Commun.* **2016**, *52*, 1859–1862.

[128] T.-C. Ong, W.-C. Liao, V. Mougel, D. Gajan, A. Lesage, L. Emsley, C. Copéret. Atomistic Description of Reaction Intermediates for Supported Metathesis Catalysts Enabled by DNP SENS. *Angew. Chemie Int. Ed.* **2016**, *55*, 4743–4747.

[129] V. K. Michaelis, E. Markhasin, E. Daviso, J. Herzfeld, R. G. Griffin. Dynamic Nuclear Polarization of Oxygen-17. *J. Phys. Chem. Lett.* **2012**, *3*, 2030–2034.

[130] F. Blanc, L. Sperrin, D. A. Jefferson, S. Pawsey, M. Rosay, C. P. Grey. Dynamic Nuclear Polarization Enhanced Natural Abundance O-17 Spectroscopy. *J. Am. Chem. Soc.* **2013**, *135*, 2975–2978.

[131] F. A. Perras, T. Kobayashi, M. Pruski. Natural Abundance (17)O DNP Two-Dimensional and Surface-Enhanced NMR Spectroscopy. *J. Am. Chem. Soc.* **2015**, *137*, 8336–9.

[132] F. A. Perras, U. Chaudhary, I. I. Slowing, M. Pruski. Probing Surface Hydrogen Bonding and Dynamics by Natural Abundance, Multidimensional, <sup>17</sup> O DNP-NMR Spectroscopy. *J. Phys. Chem. C* **2016**, acs.jpcc.6b02579.

[133] F. A. Perras, Z. Wang, P. Naik, I. I. Slowing, M. Pruski. Natural Abundance 17O DNP NMR Provides Precise O-H Distances and Insights into the Brønsted Acidity of Heterogeneous Catalysts. *Angew. Chemie Int. Ed.* **2017**.

[134] F. Blanc, L. Sperrin, D. Lee, R. Dervisoglu, Y. Yamazaki, S. M. Haile, G. De Paëpe, C. P. Grey. Dynamic Nuclear Polarization NMR of Low-γ Nuclei: Structural Insights into Hydrated Yttrium-Doped BaZrO 3. *J. Phys. Chem. Lett.* **2014**, *5*, 2431–2436.

[135] D. Lee, C. Leroy, C. Crevant, L. Bonhomme-Coury, F. Babonneau, D. Laurencin, C. Bonhomme, G. De Paëpe. Interfacial Ca2+ environments in nanocrystalline ap-

atites revealed by dynamic nuclear polarization enhanced 43Ca NMR spectroscopy. *Nat. Commun.* **2017**, *8*, 14104.

[136] E. Pump, J. Viger-Gravel, E. Abou-Hamad, M. K. Samantaray, B. Hamzaoui, A. Gurinov, D. H. Anjum, D. Gajan, A. Lesage, A. Bendjeriou-Sedjerari, L. Emsley, J.-M. Basset. Reactive surface organometallic complexes observed using dynamic nuclear polarization surface enhanced NMR spectroscopy. *Chem. Sci.* **2017**, *8*, 284–290.

[137] W.-C. Liao, T.-C. Ong, D. Gajan, F. Bernada, C. Sauvée, M. Yulikov, M. Pucino, R. Schowner, M. Schwarzwälder, M. R. Buchmeiser, G. Jeschke, P. Tordo, O. Ouari, A. Lesage, L. Emsley, C. Copéret. Dendritic polarizing agents for DNP SENS. *Chem. Sci.* **2017**, *8*, 416–422.

[138] J. Schlagnitweit, M. Tang, M. Baias, S. Richardson, S. Schantz, L. Emsley. Nanostructure of Materials Determined by Relayed Paramagnetic Relaxation Enhancement. *J. Am. Chem. Soc.* **2015**, *137*, 12482–12485.

[139] E. P. Barrett, L. G. Joyner, P. P. Halenda. The Determination of Pore Volume and Area Distributions in Porous Substances. I. Computations from Nitrogen Isotherms. *J. Am. Chem. Soc.* **1951**, *73*, 373–380.

[140] S. Brunauer, P. H. Emmett, E. Teller. Adsorption of Gases in Multimolecular Layers. *J. Am. Chem. Soc.* **1938**, *60*, 309–319.

[141] B. Lee, Y.-H. Park, Y.-T. Hwang, W. Oh, J. Yoon, M. Ree. Ultralow-k nanoporous organosilicate dielectric films imprinted with dendritic spheres. *Nat. Mater.* **2005**, *4*, 147–150.

[142] M. R. Vengatesan, S. Devaraju, K. Dinakaran, M. Alagar. SBA-15 filled polybenzoxazine nanocomposites for low-k dielectric applications. *J. Mater. Chem.* **2012**, *22*, 7559.

[143] X.-D. Liu, Z.-L. Hou, B.-X. Zhang, K.-T. Zhan, P. He, K.-L. Zhang, W.-L. Song. A general model of dielectric constant for porous materials. *Appl. Phys. Lett.* **2016**, *108*, 102902.

[144] D. Cao, Z. Shen, J. Chen, X. Zhang. Experiment, molecular simulation and density functional theory for investigation of fluid confined in MCM-41. *Microporous Mesoporous Mater.* **2004**, *67*, 159–166.

[145] B. Grünberg, T. Emmler, E. Gedat, I. Shenderovich, G. H. Findenegg, H.-H. Limbach, G. Buntkowsky. Hydrogen Bonding of Water Confined in Mesoporous Silica MCM-41 and SBA-15 Studied by 1 H Solid-State NMR. *Chem. - A Eur. J.* **2004**, *10*, 5689–5696.

[146] E. de la Llave, V. Molinero, D. A. Scherlis. Water filling of hydrophilic nanopores. *J. Chem. Phys.* **2010**, *133*, 034513.

[147] E. Bouleau, P. Saint-Bonnet, F. Mentink-Vigier, H. Takahashi, J.-F. Jacquot, M. Bardet, F. Aussenac, A. Purea, F. Engelke, S. Hediger, D. Lee, G. De Paëpe. Pushing NMR sensitivity limits using dynamic nuclear polarization with closed-loop cryogenic helium sample spinning. *Chem. Sci.* **2015**, *6*, 6806–6812.

[148] S. Penzel, A. A. Smith, V. Agarwal, A. Hunkeler, M.-L. Org, A. Samoson, A. Böckmann, M. Ernst, B. H. Meier. Protein resonance assignment at MAS frequencies approaching 100 kHz: a quantitative comparison of J-coupling and dipolar-coupling-based transfer methods. *J. Biomol. NMR* **2015**, *63*, 165–186.

[149] Y. Nishiyama, T. Kobayashi, M. Malon, D. Singappuli-Arachchige, I. Slowing, M. Pruski. Studies of minute quantities of natural abundance molecules using 2D heteronuclear correlation spectroscopy under 100kHz MAS. *Solid State Nucl. Magn. Reson.* **2015**, *66-67*, 56–61.

[150] L. B. Andreas, K. Jaudzems, J. Stanek, D. Lalli, A. Bertarello, T. Le Marchand, D. Cala-De Paepe, S. Kotelovica, I. Akopjana, B. Knott, S. Wegner, F. Engelke, A. Lesage, L. Emsley, K. Tars, T. Herrmann, G. Pintacuda. Structure of fully protonated proteins by proton-detected magic-angle spinning NMR. *Proc. Natl. Acad. Sci.* **2016**, *113*, 9187–9192.

[151] S. Lange, A. H. Linden, Ü. Akbey, W. Trent Franks, N. M. Loening, B.-J. van Rossum, H. Oschkinat. The effect of biradical concentration on the performance of DNP-MAS-NMR. *J. Magn. Reson.* **2012**, *216*, 209–212.

[152] H. Takahashi, C. Fernández-de Alba, D. Lee, V. Maurel, S. Gambarelli, M. Bardet, S. Hediger, A.-L. Barra, G. De Paëpe. Optimization of an absolute sensitivity in a glassy matrix during DNP-enhanced multidimensional solid-state NMR experiments. *J. Magn. Reson.* **2014**, *239*, 91–99.

[153] K. R. Thurber, R. Tycko. Measurement of sample temperatures under magic-angle spinning from the chemical shift and spin-lattice relaxation rate of 79Br in KBr powder. *J. Magn. Reson.* **2009**, *196*, 84–87.

[154] B. M. Fung, A. K. Khitrin, K. Ermolaev. An improved broadband decoupling sequence for liquid crystals and solids. *J. Magn. Reson.* **2000**, *142*, 97–101.

[155] B. Elena, G. de Paëpe, L. Emsley. Direct spectral optimisation of proton-proton homonuclear dipolar decoupling in solid-state NMR. *Chem. Phys. Lett.* **2004**, *398*, 532–538.

[156] H. Y. Carr, E. M. Purcell. Effects of Diffusion on Free Precession in Nuclear Magnetic Resonance Experiments. *Phys. Rev.* **1954**, *94*, 630–638.

[157] S. Meiboom, D. Gill. Modified Spin-Echo Method for Measuring Nuclear Relaxation Times. *Rev. Sci. Instrum.* **1958**, *29*, 688–691.

[158] C. Song, K.-N. Hu, C.-G. Joo, T. M. Swager, R. G. Griffin. TOTAPOL: A Biradical Polarizing Agent for Dynamic Nuclear Polarization Experiments in Aqueous Media. *J. Am. Chem. Soc.* **2006**, *128*, 11385–11390.

[159] D. Gajan, M. Schwarzwälder, M. P. Conley, W. R. Grüning, A. J. Rossini, A. Zagdoun, M. Lelli, M. Yulikov, G. Jeschke, C. Sauvée, O. Ouari, P. Tordo, L. Veyre, A. Lesage, C. Thieuleux, L. Emsley, C. Copéret. Solid-Phase Polarization Matrixes for Dynamic Nuclear Polarization from Homogeneously Distributed Radicals in Mesostructured Hybrid Silica Materials. *J. Am. Chem. Soc.* **2013**, *135*, 15459–15466.

[160] B. D. Hames (Ed.), *Gel Electrophoresis of Proteins: A Practical Approach (Second Edition)*, Oxford University Press, New York, **1998**.

[161] Y. Osada, J.-P. Gong. Soft and Wet Materials: Polymer Gels. *Adv. Mater.* **1998**, *10*, 827–837.

[162] P. Thoniyot, M. J. Tan, A. A. Karim, D. J. Young, X. J. Loh. Nanoparticle-Hydrogel Composites: Concept, Design, and Applications of These Promising, Multi-Functional Materials. *Adv. Sci.* **2015**, *2*, 1400010.

[163] V. Pardo-Yissar, R. Gabai, A. N. Shipway, T. Bourenko, I. Willner. Gold Nanoparticle/Hydrogel Composites with Solvent-Switchable Electronic Properties. *Adv. Mater.* **2001**, *13*, 1320.

[164] S. A. Asher, J. H. Holtz. Polymerized colloidal crystal hydrogel films as intelligent chemical sensing materials. *Nature* **1997**, *389*, 829–832.

[165] C. Wang, N. T. Flynn, R. Langer. Controlled Structure and Properties of Thermoresponsive Nanoparticle-Hydrogel Composites. *Adv. Mater.* **2004**, *16*, 1074–1079.

[166] D. L. Holmes, N. C. Stellwagen. Estimation of polyacrylamide gel pore size from Ferguson plots of linear DNA fragments. II. Comparison of gels with different crosslinker concentrations, added agarose and added linear polyacrylamide. *Electrophoresis* **1991**, *12*, 612–619.

[167] D. Baudouin, H. A. van Kalkeren, A. Bornet, B. Vuichoud, L. Veyre, M. Cavaillès, M. Schwarzwälder, W.-C. Liao, D. Gajan, G. Bodenhausen, L. Emsley, A. Lesage, S. Jannin, C. Copéret, C. Thieuleux. Cubic three-dimensional hybrid silica solids for nuclear hyperpolarization. *Chem. Sci.* **2016**, *7*, 6846–6850.

[168] E. Boisselier, D. Astruc. Gold nanoparticles in nanomedicine: preparations, imaging, diagnostics, therapies and toxicity. *Chem. Soc. Rev.* **2009**, *38*, 1759.

[169] J. R. Reimers, M. J. Ford, A. Halder, J. Ulstrup, N. S. Hush. Gold surfaces and nanoparticles are protected by Au(0)-thiyl species and are destroyed when Au(I)-thiolates form. *Proc. Natl. Acad. Sci.* **2016**, *113*, E1424–E1433.

[170] H. Al-Johani, E. Abou-Hamad, A. Jedidi, C. M. Widdifield, J. Viger-Gravel, S. S. Sangaru, D. Gajan, D. H. Anjum, S. Ould-Chikh, M. N. Hedhili, A. Gurinov, M. J.

Kelly, M. El Eter, L. Cavallo, L. Emsley, J.-M. Basset. The structure and binding mode of citrate in the stabilization of gold nanoparticles. *Nat. Chem.* **2017**.

[171] Z. Zhang, A. Berg, H. Levanon, R. W. Fessenden, D. Meisel. On the Interactions of Free Radicals with Gold Nanoparticles. *J. Am. Chem. Soc.* **2003**, *125*, 7959–7963.

[172] E. Besson, F. Ziarelli, E. Bloch, G. Gerbaud, S. Queyroy, S. Viel, S. Gastaldi. Silica materials with wall-embedded nitroxides provide efficient polarization matrices for dynamic nuclear polarization NMR. *Chem. Commun.* **2016**, *52*, 5531–5533.

[173] D. L. Silverio, H. A. van Kalkeren, T.-C. Ong, M. Baudin, M. Yulikov, L. Veyre, P. Berruyer, S. Chaudhari, D. Gajan, D. Baudouin, M. Cavaillès, B. Vuichoud, A. Bornet, G. Jeschke, G. Bodenhausen, A. Lesage, L. Emsley, S. Jannin, C. Thieuleux, C. Copéret. Tailored Polarizing Hybrid Solids with Nitroxide Radicals Localized in Mesostructured Silica Walls. *Helv. Chim. Acta* **2017**, *38*, e1700101.

[174] C. I. Ratcliffe, K. Yu, J. A. Ripmeester, M. Badruz Zaman, C. Badarau, S. Singh. Solid state NMR studies of photoluminescent cadmium chalcogenide nanoparticles. *Phys. Chem. Chem. Phys.* **2006**, *8*, 3510.

[175] V. Ladizhansky, G. Hodes, S. Vega. Surface Properties of Precipitated CdS Nanoparticles Studied by NMR. *J. Phys. Chem. B* **1998**, *102*, 8505–8509.

[176] O. Antzutkin, S. Shekar, M. Levitt. Two-Dimensional Sideband Separation in Magic-Angle-Spinning NMR. *J. Magn. Reson. Ser. A* **1995**, *115*, 7–19.

[177] M. M. Stalzer, M. Delferro, T. J. Marks. Supported Single-Site Organometallic Catalysts for the Synthesis of High-Performance Polyolefins. *Catal. Letters* **2015**, *145*, 3–14.

[178] B. Van Berlo, K. Houthoofd, B. F. Sels, P. A. Jacobs. Silica Immobilized Second Generation Hoveyda-Grubbs: A Convenient, Recyclable and Storageable Heterogeneous Solid Catalyst. *Adv. Synth. Catal.* **2008**, *350*, 1949–1953.

[179] A. Riisager, R. Fehrmann, S. Flicker, R. van Hal, M. Haumann, P. Wasserscheid. Very Stable and Highly Regioselective Supported Ionic-Liquid-Phase (SILP) Catal-

ysis: Continuous-Flow Fixed-Bed Hydroformylation of Propene. *Angew. Chemie Int. Ed.* **2005**, *44*, 815–819.

[180] Q. Zhang, S. Zhang, Y. Deng. Recent advances in ionic liquid catalysis. *Green Chem.* **2011**, *13*, 2619.

[181] D. Le, F. Ziarelli, T. N. T. Phan, G. Mollica, P. Thureau, F. Aussenac, O. Ouari, D. Gigmes, P. Tordo, S. Viel. Up to 100% Improvement in Dynamic Nuclear Polarization Solid-State NMR Sensitivity Enhancement of Polymers by Removing Oxygen. *Macromol. Rapid Commun.* **2015**, *36*, 1416–1421.

[182] A. Lesage, M. Bardet, L. Emsley. Through-Bond Carbon-Carbon Connectivities in Disordered Solids by NMR. *J. Am. Chem. Soc.* **1999**, *121*, 10987–10993.

[183] T. Gullion, J. Schaefer. Rotational-echo double-resonance NMR. *J. Magn. Reson.* **1989**, 196–200.

[184] T. Gullion. Introduction to rotational-echo, double-resonance NMR. *Concepts Magn. Reson.* **1998**, *10*, 277–289.

[185] J. M. Griffiths, R. G. Griffin. Nuclear magnetic resonance methods for measuring dipolar couplings in rotating solids. *Anal. Chim. Acta* **1993**, *283*, 1081–1101.

[186] K. Mueller. Analytic Solutions for the Time Evolution of Dipolar-Dephasing NMR Signals. *J. Magn. Reson. Ser. A* **1995**, *113*, 81–93.

[187] C. P. Jaroniec, B. A. Tounge, J. Herzfeld, R. G. Griffin. Frequency Selective Heteronuclear Dipolar Recoupling in Rotating Solids: Accurate 13 C-15 N Distance Measurements in Uniformly 13 C, 15 N-labeled Peptides. *J. Am. Chem. Soc.* **2001**, *123*, 3507–3519.

[188] P. Ugliengo, M. Sodupe, F. Musso, I. J. Bush, R. Orlando, R. Dovesi. Realistic Models of Hydroxylated Amorphous Silica Surfaces and MCM-41 Mesoporous Material Simulated by Large-scale Periodic B3LYP Calculations. *Adv. Mater.* **2008**, *20*, 4579–4583.

[189] A. Comas-Vives. Amorphous SiO 2 surface models: energetics of the dehydroxylation process, strain, ab initio atomistic thermodynamics and IR spectroscopic signatures. *Phys. Chem. Chem. Phys.* **2016**, *18*, 7475–7482.